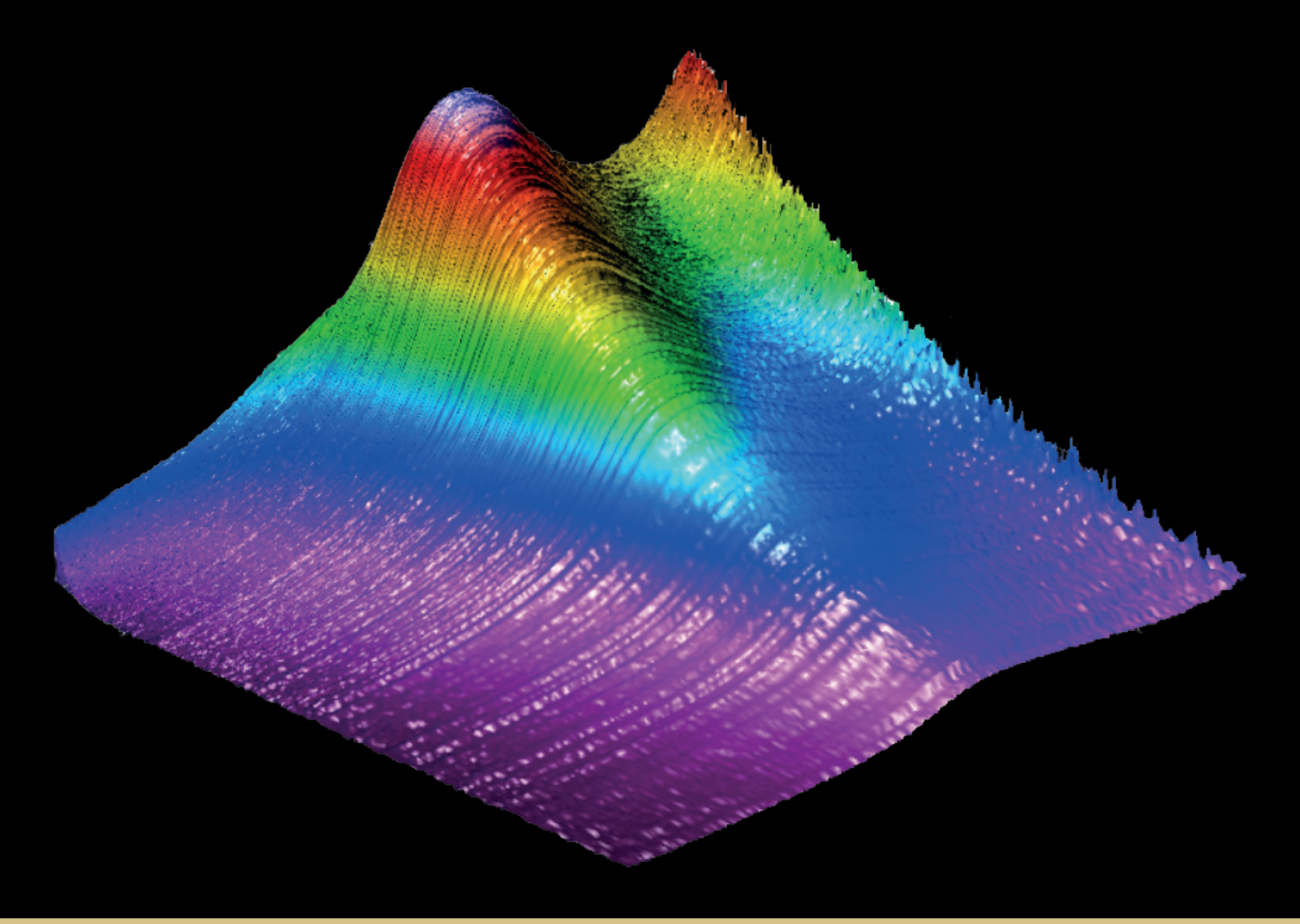

Kamila Krystyna Mentel

NEW FREE-ENERGY RELATIONSHIPS IN ELECTRON TRANSFER REACTIONS

PhD Thesis in Chemistry, specialization in Photochemistry, supervised by Professor Luís Arnaut, submitted to the Department of Chemistry of the Faculty of Sciences and Technology of the University of Coimbra

July 2017

· U C ·

Universidade de Coimbra

Dissertation submitted in order to obtain a Doctoral Degree in Chemistry

New free-energy relationships in electron transfer reactions

Kamila Krystyna Mentel

Coimbra 2017

University of Coimbra

Faculty of Sciences and Technology

Department of Chemistry

This work is dedicated to the memory of

Jerzy Mentel and **Prof. Sebastião Formosinho**

Contents

Acknowledgments

This work would not have been possible without the support and assistance of a large number of people.

First and foremost, I would like to thank my supervisor Professor Luis G. Arnaut, for the opportunity to work in his research group, for his guidance and advice throughout this project.

I would like to thank Professor Arménio Serra for the synthesis of the compounds used in Chapter 4 and 5, and for his collaboration on that work. Professor Paulo Abreu is thanked for the computational calculation supporting the experimental results.

Special thanks to all my group colleagues for their great support and welcoming, particularly to Carlos Serpa and Rui Nunes for their contribution on part of the work presented here.

I am also deeply grateful to João Pina and Fábio Schaberle for their availability to assist me with the laser systems, and theirs valuable discussions and meticulous comments.

I thank the Portuguese Foundation for Science and Technology for the doctoral grant that financially supported this research work (SFRH/BD/91209/2012).

The unwavering support and understanding of my mother Teresa, Luis, family and friends throughout my education is acknowledged, their belief in me has been an huge motivation.

Abstract

This work is a contribution to the understanding of electron transfer (ET) reactions, which are the basis of fundamental physical and chemical processes and are at the core of essential life-sustaining biological processes. In particular, ET reactions in bimolecular and intramolecular systems containing aromatic hydrocarbons and nitrile groups were examined with a view to understand the role of the medium, driving force and temperature in the energies and rates of ET reactions.

Five electron donors (naphthalene, pyrene, 3,4-dimethylanisole, p-xylene and o-xylene), and two electron-acceptors (fumaronitrile and isopropylidenomalononitrile) were used in the photoinduced bimolecular electron transfer. Bimolecular reactions were studied in solvents such as: n-heptane ($\varepsilon = 1.9$), cyclohexane ($\varepsilon = 2.0$), n-butyl ether ($\varepsilon = 3.1$), isopropyl ether ($\varepsilon = 3.9$), chloroform ($\varepsilon = 4.8$), ethyl acetate ($\varepsilon = 6.1$), methyl acetate ($\varepsilon = 6.9$), 1-chlorobutane ($\varepsilon = 7.2$), tetrahydrofuran ($\varepsilon = 7.6$), dichloromethane ($\varepsilon = 9.0$) and 1,2-dichloroethane ($\varepsilon = 10.4$). Quenching of donor fluorescence emission was observed in all bimolecular systems studied. However, a fluorescent radical ion pair was formed when fumaronitrile was used as an electron-acceptor. The data are consistent with the direct formation of contact ion pairs, rather than free ions, by photoinduced electron transfer. The temperature-dependence of charge recombination rates shows an additional decay channel competitive with the thermal equilibration.

Intramolecular electron transfer was studied using two rigidly bridged donor-acceptor molecules: 3-methoxy-1,3,5(10)-estratrien-17-yliden) malononitrile (**1**) and 1,3,5(10)-estratrien-17-yliden) malononitile (**2**). Both molecules have the same edge-to-edge separation distance between the donor and the acceptor. Studies were per-

formed in a series of solvents with different dielectric constants such as: n-butyl ether ($\varepsilon = 3.1$), isopropyl ether ($\varepsilon = 3.9$), chloroform ($\varepsilon = 4.8$), ethyl acetate ($\varepsilon = 6.1$), dichloromethane ($\varepsilon = 9.0$), 2-propanol ($\varepsilon = 20.2$) and acetonitrile ($\varepsilon = 37.0$), covering a wide range of temperatures (288-328 K) and exothermicities (–1 to –103 kcal/mol).

Time-resolved techniques, namely femtosecond pump-probe transient spectroscopy, time-correlated single photon counting and flash photolysis, were employed to probe and characterize the species with the lifetime between 0.5 ps to 30 μs. These comprehensive studies uncovered a new relationship between rates and free energies of very exothermic reactions ($\Delta G^0 < -70$ kcal/mol), which is characterized by an increase of rate constants with the driving force of the reactions, bringing an end to Marcus inverted region, and described as a "double inverted region". Additionally, it was found that reactions with apparent negative activation energies in the inverted region were slower than the analogous reactions with positive activation energy in the double inverted region. With the possible exception of acetonitrile, the rates obtained in the other solvents follow the same free-energy dependence.

Our bimolecular and intramolecular experimental data were very well supported by the theoretical prediction of the Intersecting-State Model, and challenge the interpretation of electron transfer by commonly used electron transfer theories.

Resumo

Este trabalho é uma contribuição para o entendimento das reações de transferência de eletrão (TE), que são a base de processos físicos e químicos fundamentais e estão no cerne de processos biológicos essenciais à vida. Em particular, reações de TE em sistemas bimoleculares e intramoleculares contendo hidrocarbonetos aromáticos e grupos nitrilo foram examinadas com vista a compreender o papel do meio, força motriz e temperatura nas energias e velocidades das reações TE.

Cinco doadores de eletrões (naftaleno, pireno, 3,4-dimetilanisole, p-xileno e o-xileno), e dois aceitadores de eletrões (fumaronitrilo e isopropilidenomalononitrilo) foram usados na transferência de eletrão bimolecular fotoinduzida. As reações bimoleculares foram estudadas nos seguintes solventes: n-heptano (ε=1.9), cyclohexano (ε=2.0), éter n-butílico (ε=3.1), éter isopropílico (ε=3.9), clorofórmio (ε=4.8), acetato de etilo (ε=6.1), acetato de metilo (ε=6.9), 1-clorobutano (ε=7.2), tetraidrofurano (ε=7.6), dicloro- metano (ε=9.0) e 1,2-dicloroetano (ε=10.4). Foi observada supressão da fluorescência do doador em todos os sistemas bimoleculares estudados. No entanto, quando o fumarinitrilo foi usado como um aceitador de eletrões, ocorreu a formação de um par iónico radical fluorescente. Os dados obtidos são consistentes com a formação direta de pares iónicos de contacto, em vez de iões livres, através da tranferência de eletrão fotoinduzida. A dependência da temperatura das velocidades de recombinação de carga mostra um canal de decaimento adicional competitivo com o equilibrio térmico.

A transferência de eletrão intramolecular foi estudada em duas moléculas contendo grupos doador-aceitador de eletrões ligados rigidamente entre si: 3-metoxi-1,3,5(10)-estratrien-17-ilideno) malononitrilo (**1**) and 1,3,5(10)-estratrien-17-ilideno)

malononitilo (**2**). Ambas as moléculas têm a mesma distância de separação de ponta-a-ponta entre o doador e o aceitador. Foram realizados estudos numa série de solventes com diferentes constantes dielétricas, tais como: éter n-butílico (ε=3.1), éter isopropílico (ε=3.9), clorofórmio (ε=4.8), acetato de etilo (ε=6.1), diclorometano (ε=9.0), 2-propanol (ε=20.2) e acetonitrilo (ε=37.0), cobrindo uma ampla gama de temperaturas (288-328 K) e exotermicidades (–1 to –103 kcal/mol).

Técnicas resolvidas no tempo, nomeadamente a espectroscopia de transientes femtossegundo (pump-probe), contagem de monofotão correlacionada temporalmente e fotólise por pulso de laser, foram empregues para investigar e caracterizar as espécies com tempos de vida entre 0.5 ps e 30 μs. Estes estudos abrangentes revelaram uma nova relação entre velocidades e energias livres de reações muito exotérmicas ($\Delta G < -70$ kcal/mol), a qual é caraterizada por um aumento da velocidade de reação com a força motriz das reações, levando ao fim da região-invertida prevista por Marcus, e sendo descrita como dupla região-invertida. Adicionalmente, verificou-se que as reações com energias de ativação negativas na região-invertida foram mais lentas do que as reações análogas com energia de ativação positiva na dupla região-invertida. Com a possível exceção do acetonitilo, as velocidades obtidas em outros solventes, seguem a mesma dependência da energia-livre.

Os dados bimoleculares e intramoleculares experimentais obtidos são bem suportados pela previsão teórica do Modelo de Intersecão de Estados, e desafiam a interpretação da transferênica de eletrão por teorias de transferência eletrónica frequentemente usadas.

"We are all connected! To each other biologically, to the earth chemically, to the rest of the Universe atomically"

Neil deGrasse Tyson

1 Introduction

1.1 Electron Transfer in Science

Science gives beautiful examples of how everything in the world is somehow connected with seemingly dissimilar things. For instance, what is in common in photosynthesis, corrosion and chemiluminescence? All of them share the same fundamental process, which is ubiquitous in chemistry, biology and physics. This process is called **electron transfer (ET)**, and according to the IUPAC definition can be described as:

"a transfer of an electron from one molecular entity to another, or between two localized sites in the same molecular entity."[1]

Life on Earth, in the form which exists nowadays, relies on electron transfer. ET plays a crucial role in photosynthesis, where it takes place in the photosynthetic reaction center, and is the basis for the conversion of sunlight into usable energy (ATP).[2,3] A side product of photosynthesis, is the oxygen molecule, which is used by all aerobic organisms. They use glucose and oxygen to produce ATP, in the process called cellular respiration. A final step of this process, oxidative phosphorylation, also requires transfer of electrons.[4] In addition, electron transfer is responsible for most cellular activities such as steroid metabolism, DNA UV-damage repair,[5,6] the immune response,[7,8] and many others.[9]

In the last decades, important research efforts focused on searching for alternative ways to produce energy from the renewable sources. This is driven by increasing energy demands, limited amount of non-renewable energy sources and heightened

by environmental concerns. Therefore, scientists are trying to create sustainable energy sources inspired in nature. Recently, inorganic and organic solar cells, which use electron transfer to capture and store solar energy by converting it into chemical potential, have been designed.[10–12]

Electron transfer has a huge impact on molecular electronics, where it plays important roles in molecular switches,[13] molecular wires,[14] and molecular information storage.[15] Additionally, corrosion involves the surface electron transfer between metals and oxygen in electrochemical systems. ET is also involved in water splitting, an affordable source of molecular hydrogen.[16–18]

In organic chemistry, photoinduced electron transfer participates in many chemical transformations and is often involved in bond breaking and/or forming steps in the synthesis of molecules. Electron-mediated reactions are applied in the synthesis of macrocyclic compounds[19–21] and in catalysis (e.g. in photoinduced cyclization of quinolone).[22] Moreover, chemiluminescence, where an excited electronic state is populated by chemical reaction, may also result from electron transfer.[23,24]

Electron transfer also found applications in medicine. For example, it is involved in type I mechanism in the photodynamic therapy (PDT).[25] Very promising developments of PDT of cancer are based on bacteriochlorin derivatives that use both electron transfer and energy transfer to produce reactive oxygen species.[26–28]

Electron transfer is a very common phenomenon which occurs in the gas and liquid phase and that was also found in heterogeneous systems such as semiconductors, zeolite, TiO_2 nanoparticels, electrodes, etc.[29–31]

As presented above, it is clear that ET has huge impact in several fields. Even thought electron transfer processes have been one of the most active areas of research in the last decades, and have strong implification in many applications, aspects of ET are still controversial. A proper understanding of the phenomenon will allow for full and unbiased explanation of the experimental observations in biological and artificial systems. Additionally, the new detailed knowledge obtained may guide the design of innovative and efficient ET-based materials and technologies.

1.2 Physical Principles

In this section, some of the fundamental physical principles underlying the electron transfer theory are briefly described.

1.2.1 Born-Oppenheimer Approximation

The Born-Oppenheimer approximation describes the separability of electronic and nuclear motion. This is based on the huge difference between mass of an electron and the mass of a nuclei, with the latter one being approximately a 1000 times heavier. In consequence, the electronic movement is much faster than the nuclear motion and the nuclei can be considered as stationary for a given electronic distribution.

1.2.2 Boltzmann Distribution Law

It describes the population of different energy levels in the thermal equilibrium state. It can be express by equation 1.1:

$$\frac{N_1}{N_0} = exp\left(-\frac{\Delta E}{RT}\right) \tag{1.1}$$

where N_0 and N_1 are the number of molecule is the ground state and higher energy level, respectively, represented by an energetic differences of $\triangle E = E_1 - E_0$. R is the gas constant and T is the temperature (in K).

1.2.3 Franck-Condon Principle

Franck and Condon independently reported that changes in electronic configuration occur much faster than the nuclei movement.[32,33] This is related to smaller mass of an electron in comparison with the mass of the nucleus. Such behavior is known as **Franck-Condon principle**. According to this principle, electronic transitions from ground state to the hot vibrational levels of the electronically-excited state can be represented by vertical arrows (Figure 1.1), and are called **Franck-Condon**

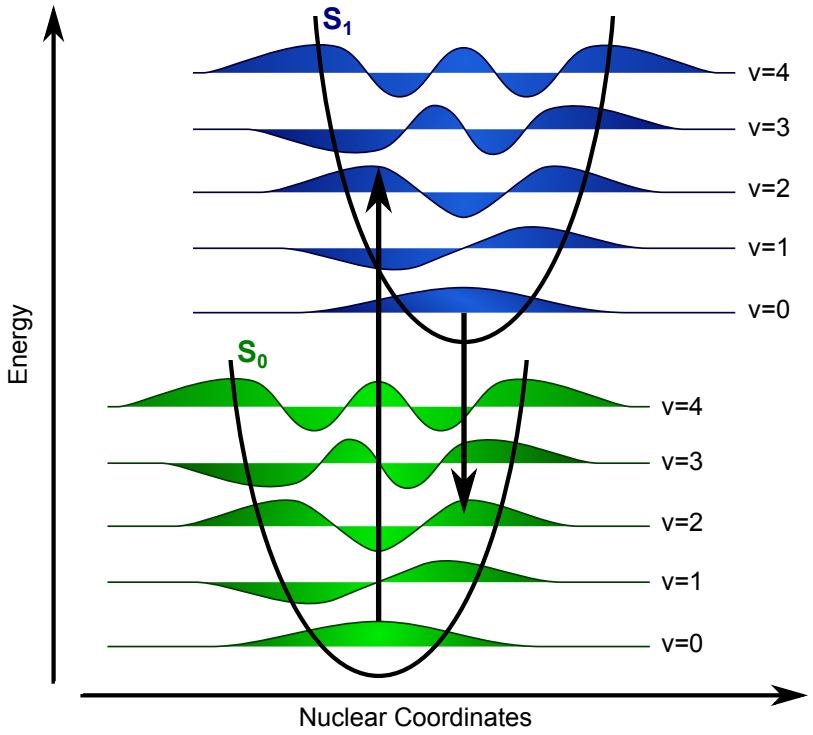

Figure 1.1 Energy diagram of Franck-Condon transitions. The arrows represent the most probable electronic transitions between vibrational states with maximum overlap.

transitions. The state populated immediately after the electronic transition is referred as a **Franck-Condon state**, which has a new electronic distribution, but still possesses the geometry of the ground state. Different vibrational levels of the excited state will not be populated in the same degree. According to Condon, the probability of the electronic transition is equal to the square of the overlap integral of the vibrational wavefunctions between initial and final states.[34]

$$FC_{m\to n} = |\langle \chi_{i,m} \mid \chi_{f,n} \rangle|^2 \tag{1.2}$$

where m and n refers to the respective vibrational states; i and f correspond to the initial and final state.

1.2.4 Electronic Coupling and Electron Tunneling

Electronic coupling describes the orbital overlap between donor and acceptor molecules, and it decreases exponentially when the distance between the donor and acceptor increases. A non-adiabatic reaction is expressed by equation 1.3:

$$V = V_0 exp\left(-\frac{\beta\,(r_c - r_0)}{2}\right) \tag{1.3}$$

where V_0 is the coupling at the donor-acceptor contact distance (which is affected by the orientation effects), β is a damping factor which depends on the electron tunneling barrier (i.e. on the medium connecting D and A), r_c is the center-to-center donor-acceptor distance and r_0 is the contact distance.

In general, tunneling refers to a barrier penetration process described by quantum mechanics. It refers to the movement of a particle from one side of the barrier to the other side, when it possess insufficient potential energy to surmount the barrier.[35–38] Electron tunneling from an electronically-excited donor to a ground state acceptor can be illustrated by the scheme presented in Figure 1.2. The donor and acceptor may be, for example, organic molecules and are represented by square wells. The electron in the donor is localized in the singly occupied molecular orbital (SOMO) where it has an electronic frequency (ν_{el}) close to $10^{15}\,\mathrm{s}^{-1}\cdot$ This is the frequency in which the electron attempts to tunnel the lowest unoccupied molecular orbital (LUMO) of the acceptor.

The probability of tunneling through the square potential barrier can be calculated using the Wenzel-Kramers-Briliouin (WKB) approximation:[39]

$$T = \frac{4\sqrt{E(\triangle V^{\ddagger} - E)}}{\triangle V^{\ddagger}} exp\left\{\frac{4\pi}{h}\int_{x_1}^{x_2}\sqrt{2M(V(x) - E)}dx\right\} \tag{1.4}$$

which E is a particle energy, $\Delta V^{\ddagger}$ is the height of energy barrier, M is the mass of the particle, x_1/x_2 describes the coordinate where the particle enters/leaves the energy barrier, and $V(x)$ is the energy barrier function. It can be seen that the tunneling

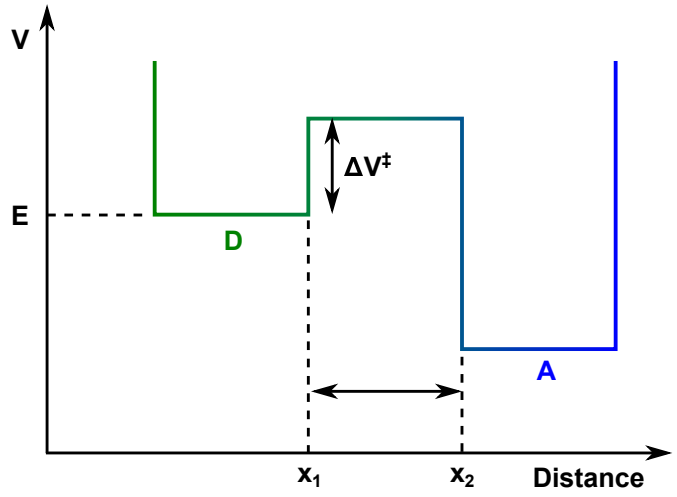

Figure 1.2 A simplified model for the electron tunneling.

probability depends exponentially on the height and length of the potential energy barrier and the mass of the particles.

For a square barrier, the damping factor,β, from eq. 1.3 can be express as:

$$\beta = \frac{2}{\hbar}\sqrt{2m_e\Delta V^{\ddagger}} \tag{1.5}$$

where m_e is the mass of the electron. Values of β reported in the literature are usually between 1 and 2 Å^{-1} for tunneling through the solvent molecules separating the donor and acceptor, and for rigid intramolecular donor-spacer-acceptor systems when the spacer is a non-conjugated system.[40]

When the barrier is a material with an optical dielectric constant ε_{op} ($\varepsilon_{op} = n_D^2$), it stabilizes the energy of the electron with respect to vacuum and the barrier $\triangle V^{\ddagger}$ is replaced by $\Delta V_0^{\ddagger}/n_D^2$, where $\Delta V_0^{\ddagger} = \Delta V_{SCE}^{\ddagger} + E_D^{red}$ ($\Delta V_{SCE}^{\ddagger}$ is the absolute potential of SCE, $\Delta V_{SCE}^{\ddagger}$=4.71 eV, and E_D^{red} is the reduction potential of the donor).[41,42] Therefore eq. 1.5 can be re-written as:

$$\beta = \frac{1.025}{n_D}\sqrt{\Delta V_0^{\ddagger}} \tag{1.6}$$

1.3 Photophysical Processes

Photoexcitation can be described as the absorption of a photon by atom/ molecule/ ion, resulting in the population of an electronically-excited state. This state can release the excess energy through several de-excitation pathways. Aleksander Jabłoński proposed a scheme with possible decay mechanisms of energy dissipation in 1933.[43] In Figure 1.3, Jabłoński diagram showing the relevant pathways to this work is presented.

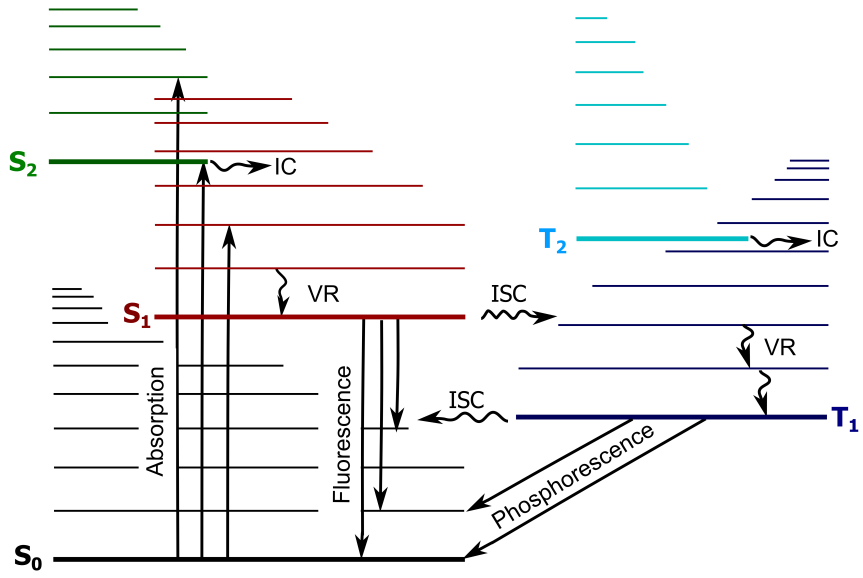

Figure 1.3 Jabłoński diagram. The electronic and vibrational levels are represented by bold and thin lines, respectively. The solid arrows represent vertical transitions (consequence of the Franck-Condon principle) which correspond to radiative pathways. The wavy arrows correspond to the vibrational relaxation (VR) and horizontal radiationless transitions: internal conversion (IC) and intersystem crossing (ISC).

1.3.1 Radiative De-excitation Transitions

All deactivation pathways occurring from the higher to the lower electronic state, accompanied with photon emission are refereed as **radiative de-exciation transitions.**

A transition between states of the same multiplicity is termed **fluorescence** and it takes place from the lowest vibrational level of the electronically-excited state to the ground state. This relaxation pathway is spin-allowed. Most common fluores-

cence occurs between $S_1 \rightarrow S_0$ states. In this case, the lifetime of the excited state is relatively short, around $10^{-9} - 10^{-6}$ s. According to Kasha's rule, fluorescence should occur from the lowest electronically-excited state.[44] This behavior was justified by assumption that in higher-lying excited states the internal conversion is more probable than the radiative decay. Nonetheless, in several compounds fluorescence from the higher electronically-excited state (S_n, where n $\geq$ 2) was observed, which is a violation of the Kasha's rule.[45]

If the transition occurs between states of different multiplicity the process is called **phosphorescence** and is spin-forbidden. Therefore, a transition from T_1 to S_0 takes more time than one from $S_1 \rightarrow S_0$ and may last up to few seconds.

1.3.2 Radiationless Transitions

Radiationless transitions correspond to deactivation processes of the excited state which are not accompanied by light emission.

When a transition occurs between states of the same multiplicity it is called **internal conversion (IC)**. This relaxation takes place from the lowest vibrational level of a higher electronic excited state (S_n) to a lower energy state (S_{n-1}). These transitions occur between vibrionic states with the same energy (horizontal transition) and the hot vibrational level of the lower lying state is populated.

The transition between states of different multiplicity, requires flip of the spin, and is named **intersystem crossing (ISC)**. The rate constant of ISC is usually smaller than the rate of IC because of the spin-forbidden nature of the transition. Nonetheless, it might occur if one of the mechanisms is present:

1. **Spin-orbital coupling (soc)**- It describes how the spin of an electron is affected by the magnetic coupling with its orbital motion. In this case, the spin angular momentum is mixing with the orbital angular momentum, which preserves the total momentum during the spin-flip. Here, the singlet state will have some triplet character while the triplet possesses some singlet character, as a result, the mixing of these states is feasible. The presence of the heavy

nuclei increases the magnitude of the spin-orbital coupling, therefore increase the probability of ISC.[46,47] This is called the **heavy atom effect**, which can be divided for internal or solvent effect depending on where the heavy nuclei were incorporated. Spin-orbital coupling is also enhanced when the spin-flip is associated with the transfer of the electron between orthogonal orbitals. It occurs when π orbitals of the donor are in nearly perpendicular orientation relative to the orbitals of the acceptor.[48]

2. **Hyperfine coupling (hfc)**- It is a contact interaction between a nucleus and an electron, which wavefunction overlap in space. This means that electronic wavefunctions of a nucleus is overlapping with the electronic wavefunction of a spin. Here, electron spin experiences magnetic coupling resulting from nuclear spin.[47]

1.3.3 Vibrational Relaxation (VR)

Upon photon absorption, the molecule is excited to the Franck-Condon state. In the vibrational (or "cooling"), the excess of vibrational energy is lost during collisions with solvent molecules. This corresponds to the thermal equilibration between the hot vibrational state and the solvent. The vibrational relaxation may lead to the lowest vibrational level of the electronically-excited state. This relaxation is fast and occurs with rates of about 10^{12} s^{-1}.

1.3.4 Photochemical Quenching Pathways

The deactivation of the electronically-excited state may occur by interaction with a quencher, in a process called quenching. The quencher decreases the lifetime of excited molecule by offering a decay pathway that is competitive with the natural lifetime of the electronically-excited species. The quenching processes can be divided in two ways:

1. **Intermolecular relaxation**, when excited state species and quencher are different molecules;

2. **Intramolecular relaxation**, when excited state species and quencher are incorporated in the same molecule.

The influence of the quencher on the fluorophore can be measured by following the decrease in fluorescence upon addition of different concentrations of the quencher. The quenching rate constant (k_q) can be calculated from the slope of the Stern-Volmer plot I_0/I versus quencher concentration, $[Q]$, expressed by:

$$\frac{I_0}{I} = 1 + k_q \tau_0 [Q] \tag{1.7}$$

where I and I_0 are the fluorescence intensities of the fluorophore with and without the quencher, respectively, and τ_0 is the lifetime of the fluorophore in the absence of the quencher.

1.3.4.1 Energy Transfer

An electronically-excited molecule (donor) may relax to a lower-lying electronic state by transferring its excess energy to another molecule (acceptor), which is simultaneously promote to a higher electronic state (eq. 1.8). The efficiency of energy transfer increases with overlapping of the emission spectrum of the excited donor and the absorption spectrum of the acceptor.

$$D^* + A \rightarrow D + A^* \tag{1.8}$$

Energy transfer can occur by one of the two possible mechanisms presented in Figure 1.4. Dexter energy transfer, also called electron-exchange transfer, occurs typically at short distances (up to ca. 10 Å), because it requires orbital overlap between donor and acceptor.[49] Förster energy transfer use a Coulombic interaction mechanism and can occurs at longer distances (up to ca. 100 Å).[50] It is also refereed as the dipole-dipole interaction.

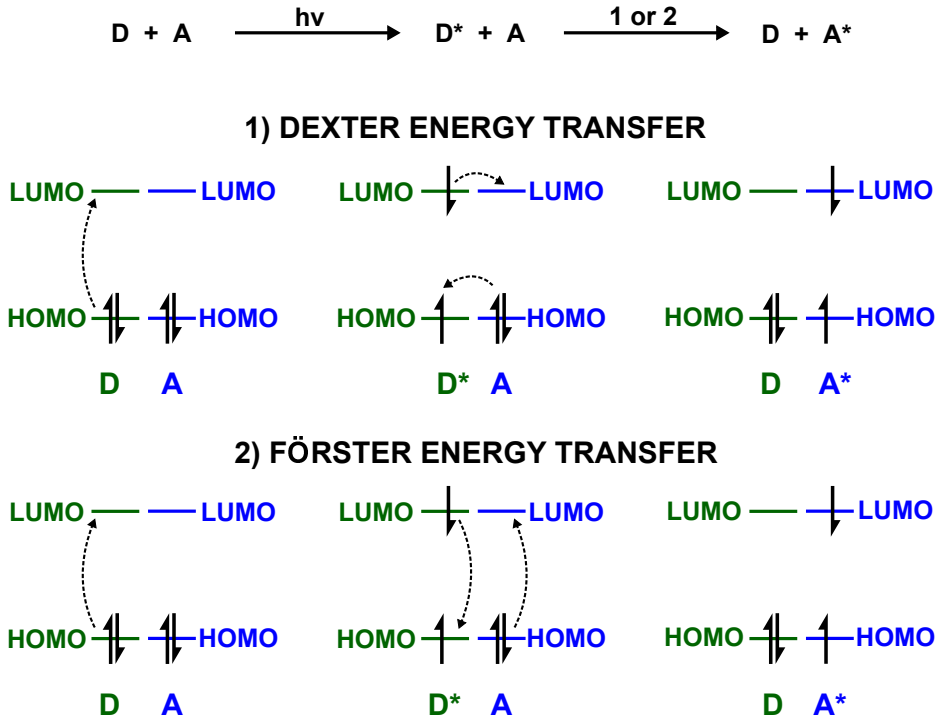

Figure 1.4 Electronic occupation before and after photoexcitation, and after energy transfer.

1.3.4.2 Electron Transfer

This process can be described as a quenching of the photoexcited state by transfer of an electron to the quencher in the ground state. Electron transfer can be divided as an oxidative (1.9) or a reductive (1.10) process, depending on which molecule was excited:

$$D^* + A \rightarrow D^{\cdot +} + A^{\cdot -} \qquad Oxidative\ Electron\ Transfer \tag{1.9}$$

$$A^* + D \rightarrow D^{\cdot +} + A^{\cdot -} \qquad Reductive\ Electron\ Transfer \tag{1.10}$$

Oxidative and reductive bimolecular electron transfer are presented in Figure 1.5, together with electronic occupation. The detailed description of electron transfer is presented in Section 1.4.

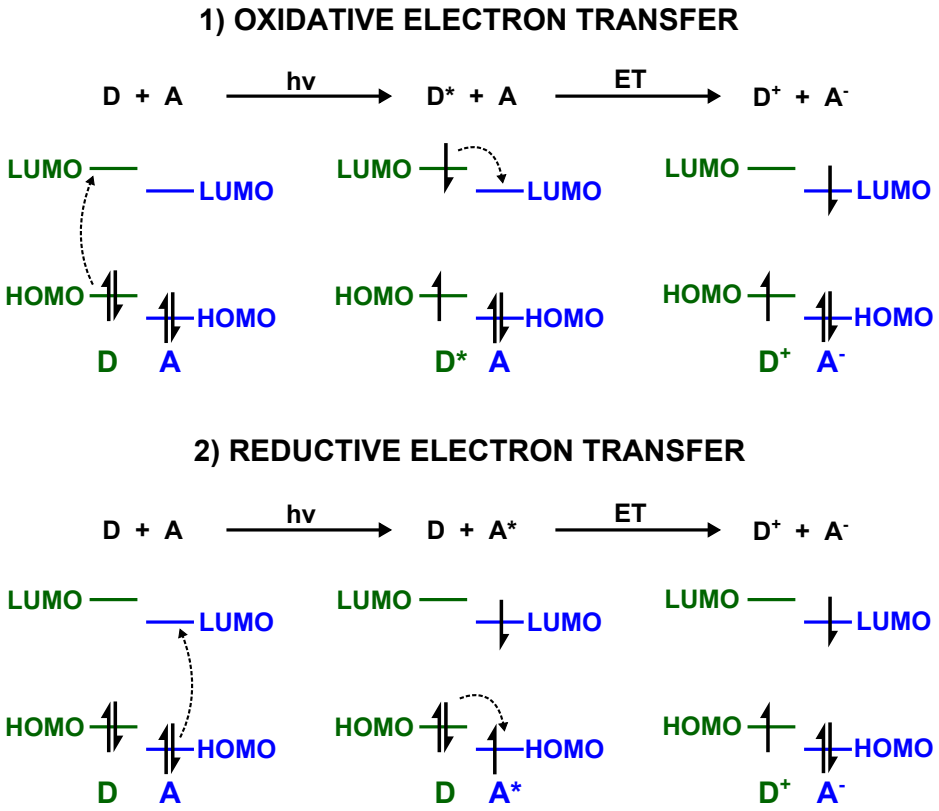

Figure 1.5 Electronic occupation before and after photoexcitation, and after electron transfer.

1.3.5 Lifetime of Excited State

The lifetime of the excited state (τ) depends on the all possible deactivation pathways and it is described as the sum of the rates of all decay processes, $\sum k_{decay}$:

$$\tau = \frac{1}{\sum k_{decay}} = \frac{1}{k_r + k_{nr}} \tag{1.11}$$

where k_r corresponds to the all radiative processes and k_{nr} includes all processes not involved in the emission of photons (radiationless processes and quenching).

The rate of the radiative processes is assumed to be temperature independent, while k_{nr} may depend on the temperature.

1.4 Photoinduced Electron Transfer

As mentioned in Section 1.3.4.2, the absorption of UV or visible light may initiate electron transfer from the donor to the acceptor molecule. The light can be absorbed by the donor or by the acceptor. It this work, the electron donating group is excited, therefore it becomes a better reducing agent than it was in the ground state. An example of ET, together with the subsequent processes, is given by equations 1.12-1.14:

$$D \xrightarrow{h\nu} D^* \tag{1.12}$$

$$D^* + A \xrightarrow{ET} D^{\cdot+} + A^{\cdot-} \tag{1.13}$$

$$D^{\cdot+} + A^{\cdot-} \xrightarrow{BET} D + A \tag{1.14}$$

First, neutral donor is excited. Then, forward electron transfer (also called **Charge Separation, CS**) occurs and **Charge-Transfer state** (**CT**) is formed (eq. 1.13). This state can return to the ground state via **Charge Recombination** (**CR**), which is also called back electron transfer (eq. 1.14).

1.4.1 Charge Separation

Forward electron transfer occurs in systems where donor and acceptor can approach each other to a relatively close distance. When donor and acceptor are independent molecular entities, the quenching of the excited state via ET depends on the concentration of the quencher and of the diffusion of the molecules. The lifetime of the populated excited state must be sufficiently long to allow for diffusion to take place.

The electron transfer rate can be calculated from:

$$k_{ET} = \frac{1}{\tau_1} - \frac{1}{\tau_0} \tag{1.15}$$

where the τ_1 and τ_0 are the lifetimes of the singlet excited state in the absence and presence of quencher, respectively.

Electron transfer occurs spontaneous when the reaction possesses sufficient driving force, $-\Delta G^0$. The Gibbs free energy for the photoinduced electron transfer (ΔG^0_{CS}) can be calculated using the Weller equation:[51]

$$\Delta G^0_{CS} = E^{ox}_D - E^{red}_A - E^* - \frac{e^2_0}{\varepsilon_s \cdot r_c} - \frac{e^2_0}{2}\left(\frac{1}{r_{d^+}} + \frac{1}{r_{a^-}}\right)\left(\frac{1}{\varepsilon_{ACN}} - \frac{1}{\varepsilon_s}\right) \quad (1.16)$$

where E^{ox}_D and E^{red}_A are the oxidation and reduction potentials of donor and acceptor, E^* is the excited state energy of D^*, r_c is the donor-acceptor center-to-center distance, r_{d^+}/r_{a^-} are the effective radii of donor/acceptor, $\varepsilon_{ACN}/\varepsilon_s$ are the dielectric constants of acetonitrile/solvent and $e^2_0 = e^2 N_A/4\pi\varepsilon_0$. The effective radii can be calculated using the molar volume of the neutral molecule:

$$\frac{4}{3}\pi r^3 = \frac{M}{N_A\,\rho} \quad (1.17)$$

where M is the molecular weight, N_A is the Avogadro's number, and ρ is the density of the crystal.

Looking at the equation 1.16, it is evident that ET strongly depends on the redox properties of donor and acceptor and the excited-state energy. The redox groups are characterized by different ionization potential, which correspond to the energy used for removing an electron from the atom/molecule in the gas phase. Therefore, by proper choice of the donor and acceptor the driving force of the reaction can be smoothly modulated. Additionally, it can be observed that the solvent polarity and the distance between the donor and acceptor will affect the driving force.

Studies on bimolecular electron transfer show that diffusion of the donor and acceptor can mask the free-energy dependence of ET reactions.[52] To eliminate diffusion and make possible transfer of the electron at variety of known donor-acceptor distances, ET should be studied in intramolecular systems. In these systems donor and acceptor can be connected by rigid or flexible bridge. It was found that an increase in k_{ET} can be achieve by increasing the electronic coupling (V). V is a critical feature affecting the ET rate and depends on several factors such as:

I. Distance between donor and acceptor. Increasing the separation distance between the donor and acceptor decreases the V and, consequently, slows down the electron transfer rate constant. The presence of a relatively long bridge, leads to electron transfer at larger separations between redox groups than in the bimolecular ET. This was reported, for example, in the work of Oevering and co-workers, where they studied intramolecular electron transfer in rigidly bridged donor-acceptor pairs.[53] The bridges used in this work kept donor and acceptor at well-defined distances and blocked rotations from occuring. The authors showed that it was possible to observe electron transfer even for molecules with the separation distance between the center of the aromatic ring and the center of the dicyanoethene moiety equal to 14.9 Å.[53] This process could occur because it was sufficiently fast and could compete with other relaxation processes of the excited state.

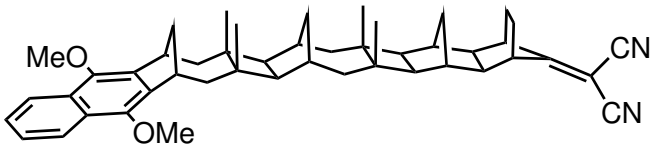

Figure 1.6 Structure of bridged donor-acceptor molecule with large spatial separation distance (R_c=14.9 Å).[53]

Depending on the distance, electron transfer can follow a (i) direct mechanism in case of short bridges or (ii) indirect mechanism, through intermediate states, corresponding to the localization of the electron in part of the bridge.[54] This is clearly seen when another redox group is present in the spacer.

II. Orientation between donor and acceptor. Orientation dependence was observed by Closs et al., and shown to change the electronic coupling between donor and acceptor.[55] Other studies have also shown that the ET rate strongly depends on the orientation and the orbitals involved in the transfer.[56] Miller suggested that some molecules may adopt special orientation which will decrease V to zero, which in consequence would drastically decrease the electron transfer rate.[57]

III. Nature of the bridge. The electronic structure of the bridge may play an important role. Unsaturated C-C bonds will support the delocalization of the electron

in the bridge.[58] Additionally, the presence of π orbitals maximizes the electronic coupling by forcing more planar structure, what should increase the ET rate.[59] A bridge consisting of the saturated C-C bonds does not support electron delocalization, however, it may still assists in the transfer of the electron. Closs et al. studied intramolecular electron transfer in several systems where the donor-acceptor pair was constant but separated by bridges with different lengths. They suggested that the k_{ET} depends on the number of covalent bonds in the bridge connecting donor and acceptor, rather than their direct separation.[55,60] They also showed that even for cases where the bridge itself has a low electron density, it still plays an important role in the electronic coupling between the donor and acceptor.[61]

IV. Flexibility of the bridge. A flexible bridge may allow a closer proximity between the donor and acceptor, which will favor a direct electron transfer and influence its rate. It was observed that in very flexible systems a harpooning phenomena can occur. In addition, in U-shaped D-B-A systems, extensive conformational changes were observed due to strong Coulombic interaction between the charges.[62] On the other hand, a rigid bridge prevents rotation or bending between donor-acceptor moieties. This assures that the distance and orientation between redox moieties will be unchanged before and after ET.[63]

V. Through-bond (TBI) and through-solvent (TSI) interactions. TBI plays a dominant role in extended structures with π-conjugated bridges and even in saturated hydrocarbon bridges.[58] TBI was shown to be the most favorable pathway of mediation of ET in molecules with an all-trans array of σ bonds.[58] Electron transfer rates in these molecules decrease exponentially with an increasing number of separating bonds, which corresponds mainly to the changes in the electronic coupling. Loosing the all-trans configuration decreases the rate constant and leads to higher solvent dependence on the rate. This is connected with the increasing contribution of TSI.[58] Zimmt et al. showed that when the donor and acceptor are connected by a bridge, that allows for a face-to-face orientation, a cleft is created. If this cleft is accessible to the solvent, then solvent-mediated electron transfer will predominate.[64]

1.4.2 Charge-Transfer State

In bimolecular systems the charge-transfer state obtained by ET between neutral species can be described as a geminate radical ion pair, which consist of a radical cation of donor $(D^{\bullet+})$ and a radical anion of acceptor $(A^{\bullet-})$. Depending on the distance between the radical ions and their nature, the properties of the charge-transfer state can change dramatically. Radical ions which are in contact distance $\left(3 < r_c < 4\,\mathring{A}\right)$ can be described as **Contact Ion Pair (CIP)**. On the other hand, when the ions are separated by solvent molecules $\left(6.5 < r_c < 8.8\,\text{Å}\right)$, they are named **Loose** or **Solvent-Separated Ion Pair (LIP or SSIP)**.[51,65] CIP have higher electronic couplings than LIP,[66] and are dominant in non-polar solvents, due to the reduced solvation. The formation of the radical ion pairs in the solution is possible due to the presence of two interactions on the charged species, the Coulombic stabilization and solvation, which are included in eq. 1.16 as the fourth and fifth term, respectively.[67,68] The solvent molecules rapidly stabilize the ion pair after its formation in solution. In polar solvents, the radical ion pair can undergo a further solvation process, which leads to the dissociation of the radical ions and to the formation of **Free Ions** $\left(r_c > 10\,\text{Å}\right)$. A schematic representation of the charge-transfer states and free ions is shown in Figure 1.7.

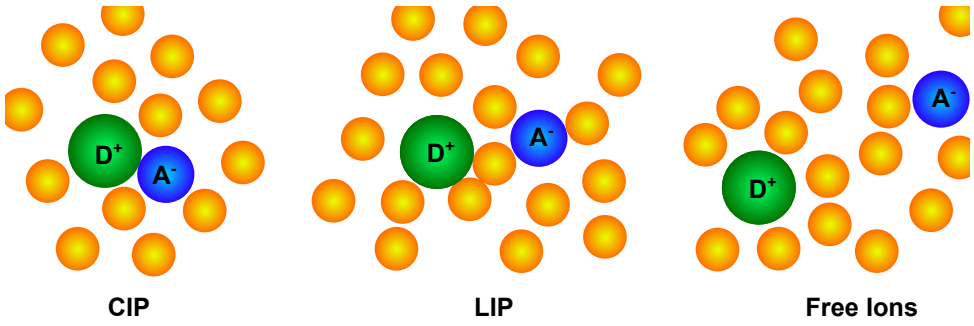

Figure 1.7 A schematic representation of the radical ion pairs and free ions surrounded by solvent molecules.

1.4.3 Exciplex

In some systems it may be difficult to form a charge-transfer state directly from D^* and A. Therefore, an exciplex intermediate needs to be formed, which corresponds to the electronically-excited complex of the photoexcited molecule (D^*) with the quencher (A), which is represented as $[DA]^*$. In photoinduced electron transfer, exciplexes usually have a strong charge-transfer character and a reduced excited state character. The wavefunction of an exciplex (Ψ_{EX}) can be described as a sum of wavefunctions of pure locally excited state, pure charge separated state and pure ground state[47]

$$\Psi_{EX} = c_{LE}\Psi_{LE}\left[D^*A\right] + c_{CS}\Psi_{CS}\left[D^{\bullet+}A^{\bullet-}\right] + c_{CS}\Psi_{CS}\left[DA\right] \tag{1.18}$$

Depending on the contribution of each wavefunction, the exciplex can adapt different properties. When the locally excited state is considerably higher in energy than charge separated state, the mixing of the functions is small, and the exciplex becomes the contact ion pair. Stronger charge-transfer character corresponds to the weaker emission.[65]

The structures of the photoexcited molecule and quencher have impact on the nature of an exciplex. Planar organic molecules will facilitate exciplex formation due to an easier adaptation of the face to face geometry, which brings groups to close distance.[68]

1.4.4 Charge Recombination

The CT state can return to the ground state via emission of a photon or by radiationless processes. The activationless transition to the ground state is referred as charge recombination (CR), as the electron is relocated from the acceptor to donor.

The emission of the CT state is characterized by a broad, structureless band, which occurs at higher wavelengths than the fluorescence of the locally excited state. The position of the band shows the solvatochromic behavior. Lippert and Mataga proposed independently equation 1.19, to account for the solvent dependence of CT emission:[69,70]

$$\bar{\nu}_{CT} = \bar{\nu}_{CT}(0) - \frac{2\mu_{CT}^2}{hc\rho^3}\Delta f \tag{1.19}$$

where μ_{CT} is the dipole moment, c is the speed of the light, ρ is the radius of the spherical Onsanger cavity in which the dipolar molecule was placed, and $\triangle f$ is a solvent parameter defined by:

$$\Delta f = \Delta\varepsilon - 0.5\Delta n_D^2 = \frac{(\varepsilon - 1)}{(2\varepsilon + 1)} - 0.5\frac{(n_D^2 - 1)}{\left(2n_D^2 - 1\right)} \tag{1.20}$$

where ε is the dielectric constant of the solvent and n_D is the refractive index. Equation 1.19 allows the estimation of the dipole moment, which gives information about the separation between the charges.

The free Gibbs energy for the charge recombination ($\triangle G_{CR}^0$) can be obtained from equation 1.21:

$$\Delta G_{CR}^0 = -(\triangle G_{CS}^0 + E^*) \tag{1.21}$$

The charge recombination is not the only pathway for the deactivation of the ^1CT state as discussed below.

1.4.5 Factors Affecting Charge Recombination

Scientists are often inspired by photosynthesis when designing artificial light conversion systems. However, efficient conversion of sunlight into electrical power is hard to achieve. To maximize light conversion, a few requirements should be fulfilled: high quantum yield of charge separation, minimal energy lost, and formation of a long-living charge-transfer state.[71] The highest quantum yield is obtained by optimizing the system to maximize the role of charge separation. In solar energy conversion, the charge recombination is recognized as a "wasting" energy process and various strategies have been developed to minimize it, such as:

Relays - Upon photoinduced electron transfer, a sequence of thermal electron transfers occurs, which produces a larger spatial separation between $D^{\bullet+}$and $A^{\bullet-}$and impede charge recombination to the ground state. This approach was found, for example, in the photosynthesis.

Electron spin - To decrease the charge recombination quantum yield, intersystem crossing to the triplet charge transfer (^3CT) state or to the locally excited triplet (T_1) state is used. Triplet states live longer, because the $T_1 \rightarrow S_0$ transition is forbidden.

The ^1CT state, which has relatively long lifetime, can undergo intersystem crossing to the ^3CT state, if the energy difference between the CT states is small (minor singlet/triplet splitting). The mechanism of ISC will involve the hyperfine coupling (hfc-isc), when electronic coupling is weak. This transition occurs in intramolecular systems (less common in bimolecular ET) when the separation between donor and acceptor is considerably high, e.g. in the photosynthesis reaction center.[72] ISC via hyperfine coupling occurs typical with rate close to $10^8\ s^{-1}$. After slow hfc-isc, fast charge recombination to the locally-excited triplet state will occur, if the charge-transfer state has higher energy than T_1.

In the systems with small spatial separation between $D^{\bullet+}$and $A^{\bullet-}$, direct conversion to locally-excited triplet state (T_1) is possible via soc-isc. The spin-orbital coupling

between ^1CT and T_1 is an electron transfer reaction with the spin flip, which requires a high electronic coupling between these states. The orbital occupation in ^1CT and ^3CT is the same, for that the spin-orbital coupling is equal to zero, thus ^3CT will never be populated via soc-isc.[48]

Electron tunneling - By increasing the distance between the donor and acceptor, the overlap between chromophores gets smaller. In this case, according to the eq. 1.4 the favorable long distance tunneling should slow down the charge recombination.

Solvent effect - Changes in the solvent polarity may affect the lifetime of the charge-transfer state. For instance, polar solvents in bimolecular systems support the formation of the solvent-separated radical ion pairs and free ions and, consequently, the yield of deactivation of the CT state by the charge recombination to the ground state decreases.

Orbital Symmetry - In the intermolecular ET, a coplanar or cofacial orientation of the molecules gives a higher overlap of π orbitals. This results in a very fast charge separation, which is supposed to slow down charge recombination. Changes in the orbital symmetry, may allow the population of the triplet state, and decrease of the charge recombination yield.[48]

Coulomb effect - The product of electron transfer between an ion and neutral molecule will be a pair of a neutral species and an ion. The lack of Coulombic attraction will separate them at a longer distance, and will slow down the charge recombination or even block it completely.

1.5 Main Theories of Electron Transfer

Researchers from different scientific areas proposed numerous solutions to the problem of estimating electron transfer rates from theoretical predictions. In this section, we focus on Marcus classical theory (awarded with the Nobel prize in Chemistry in 1992) and present its critique. This theory is compared with theories based on quantum-mechanical treatments of electron transfer.

1.5.1 Adiabatic versus Non-Adiabatic Reaction

Figure 1.8 represents a general potential energy diagram for an adiabatic and a non-adiabatic electron transfer. The reactants are shown as R and the products as P. The equilibrium configurations of initial and final steps are presented by A and B. The transition between these two states needs to be (i) vertical, to respect Franck-Condon principle, and (ii) horizontal, to respect the conservation of energy. Therefore, electron transfer can only occur in the cross-section of two parabolas (C).

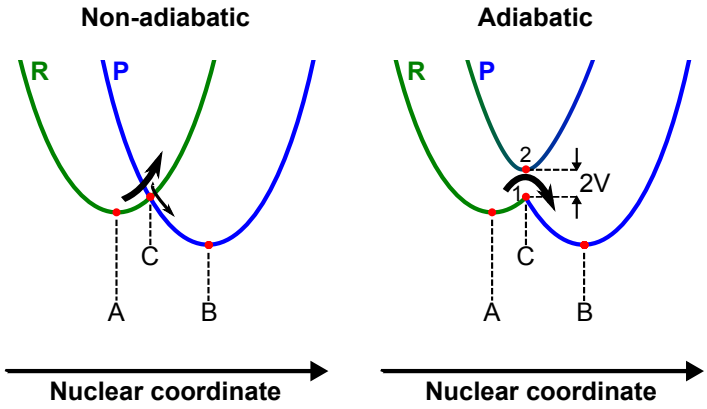

Figure 1.8 Free energy diagram for adiabatic and non-adiabatic electron transfer. The curve representing the reactants (R) actually represent two species: the electron donor and the electron acceptor. The same applies to the curve representing the products (P).

In **non-adiabatic reaction**, electron transfer is a quantum jump process from R to P. The transition between A and C is an activated step. Electron in position C can return to A, or jump to P, followed by relaxation to the equilibrium position B. The probability of transition $A \rightarrow B$ by crossing C, depends on the electronic coupling between R and P. Non-adiabatic electron transfer is treated by Fermi's

Golden Rule, and k_{ET} is equal to:

$$k_{ET} = \frac{2\pi}{\hbar} V^2 FCWD \tag{1.22}$$

where $FCWD$ is the Franck-Condon weighted density of states factor, V is the electronic coupling, which needs to be smaller than the thermal energy ($V < k_B T$) in a non-adiabatic reaction.

At the point where two electronic configurations have the same energy, a splitting of energy levels occurs, known as diabatic states (represented by 1 and 2 in Figure 1.8). In this case, large coupling element gives a higher probability for the electron transfer and the transition $A \rightarrow C \rightarrow B$ is no longer a jump, but instead is a smooth transition called **adiabatic electron transfer.**

1.5.2 Marcus Theory

1.5.2.1 Classical Theory

In 1956, Rudolph Marcus formulated an electron transfer theory which was further developed in the following years.[73,74] The theory describes the distortion from the equilibrium configuration of the reactants, products and solvent. The reactants ($Red_1 + Ox_2$) undergo electron transfer and form the products ($Ox_1 + Red_2$):

$$Red_1 + Ox_2 \rightarrow Ox_1 + Red_2$$

This process is represented by two parabolas. The first parabola corresponds to the reactants (R), whose nuclear potential energy is equal to the total energy of the donor, acceptor and surrounding. The second parabola describes the products (P), with the nuclear potential energy of the system after electron transfer. These parabolas are vertically separated by the free energy, ΔG^0, which is also referred as the energy gap. The transition from R to P usually involves changes in the bond lengths in the donor and acceptor, and also reorganization of the solvent dipoles.

In classical Marcus theory, the rate of ET depends on driving forces of the reaction $(-\Delta G^0)$ and on the reorganization energy (λ), which describes the rearrangement of the nuclear position of the donor and acceptor plus the changes in the solvent. Assuming, that the solvent behaves as a dielectric continuum, the bimolecular rate constant (k_{ET}) for a nearly-adiabatic electron transfer $(\kappa_{el} \approx 1)$ can be estimated from equation 1.23:

$$k_{ET} = \kappa_{el} Z exp\left[\frac{-\left(\Delta G^0 + \lambda\right)^2}{4\lambda k_B T}\right] \tag{1.23}$$

where: Z is the collision frequency factor, κ_{el} is the electronic transmission factor, k_B is the Boltzmann's constant and T is the temperature in K.

Marcus predicted a quadratic dependence of the energy barrier (ΔG_{act}) and Gibbs free energy of the reaction (ΔG^0):

$$\Delta G_{act} = \frac{\left(\lambda + \Delta G^0\right)^2}{4\lambda} \tag{1.24}$$

where the reorganization energy is 4 times the intrinsic barrier (*i.e.* the barrier for $\Delta G^0 = 0$). In Figure 1.9, the parabolic relation between logarithms of rate constant as a function of the standard free energy is presented.

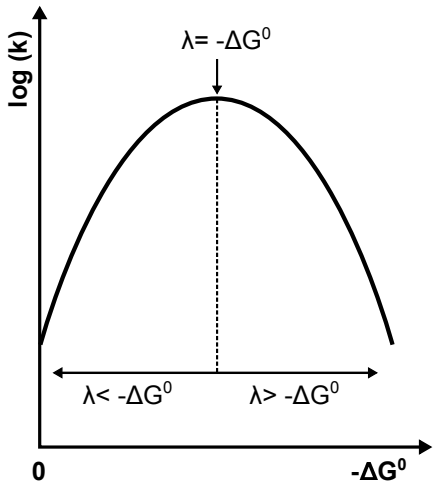

Figure 1.9 Plot of the logarithm of the rate versus the driving force, according to the predictions of Marcus theory.

It can be seen, that the electron transfer rate versus the driving force adopts different dependencies, which can be divided in three regions:

Normal - the rate constant of ET increases with increasing driving force, $\lambda < -\Delta G^0$;

Optimal - when reorganization energy is equal to the driving force, $\lambda = -\Delta G^0$, the activation barrier is zero and the rate constant attains its maximal value;

Inverted - the rate of ET decreases with increasing the exothermicity of the reaction, $\lambda > -\Delta G^0$.

Figure 1.10, presents the energy diagrams illustrating the reactants (R) and the products (P) curves separated by different exothermicities of the system. The graphical representation of the activation energy (ΔG_{act}), free energy of the reaction (ΔG^0) and reorganization energy (λ) is also given in figure.

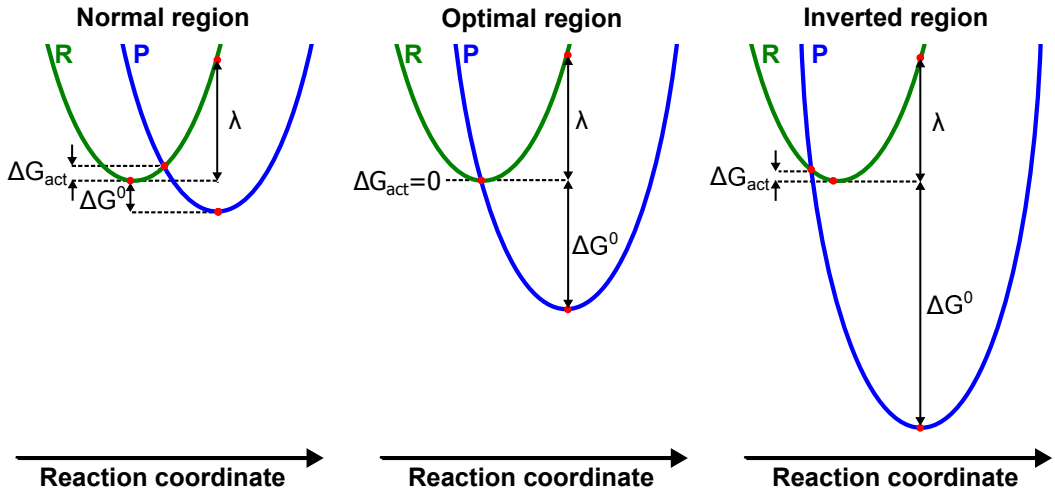

Figure 1.10 Free energy diagram presenting the normal, optimal and inverted regions.

1.5.2.2 Reorganization Energy

The reorganization energy corresponds to the energy which would be necessary to move the configuration of the reactant state to that of the product state, without transferring an electron. It is represented as the sum of the solvent (outer, λ_s) and solute (inner, λ_i) reorganization energies:[74]

$$\lambda = \lambda_s + \lambda_i \tag{1.25}$$

The solvent reorganization energy describes the differences in the configuration of the solvent molecules surrounding the electron donor and acceptor when they exchange an electron. It includes the changes in the orientation and polarization of the solvent molecules upon electron transfer. When the solvent is assumed to behave as a dielectric continuum medium, λ_s can be calculated by knowing the effective radii of the donor and acceptor, treated as charged spheres (r_{D^+} and r_{A^-}) separated by a distance (r_c). According to Marcus, the solvent reorganization energy is given by:[73]

$$\lambda_s = \Delta e^2 \left(\frac{1}{n_D^2} - \frac{1}{\varepsilon}\right)\left(\frac{1}{2r_{D^+}} + \frac{1}{2r_{A^-}} - \frac{1}{r_c}\right) \tag{1.26}$$

where: Δe is the amount of charge transferred, n_D is the refractive index and ε is the dielectric constant.

In nonpolar solvents, continuum model works poor since the electrostatic effect becomes negligible.[75] Additionally, it was later recognized that equation 1.26 overestimates λ_s.[41,76] Newton and co-workers followed a phenomenological approach to the continuum model, with fitted atomic and molecular radii, to conclude that equation 1.26 overestimates λ_s by a factor of 2 in donor-spacer-acceptor systems.[77] More recently, Li used a constrained equilibrium principle to arrive at a correction that lowers the λ_s in polar solvent (by factor of 3) and in middle polarity solvents (by factor of 2 times):[75]

$$\lambda_s(Li) = \left[\frac{\varepsilon - n_D^2}{n_D^2(\varepsilon - 1)}\right]\lambda_s \tag{1.27}$$

The solute reorganization energy corresponds to the structural differences in the reactant and product states. It describes the changes in the bond lengths and bond angles of the donor and acceptor, which occur upon ET. This can be expressed by:[78,79]

$$\lambda_i = \frac{1}{2} \sum f_i \left(\Delta l_i\right)^2 \tag{1.28}$$

where f_i is the stretching force constant associated with the oscillator i and Δl_i is the change in the equilibrium length, and the sum is made over all the oscillators that change their nuclear configuration with the transfer of the electron from the donor to the acceptor.

1.5.2.3 Inverted Region

As presented in Section 1.5.2, the inverted region should be observed when the driving force of the reaction exceeds the reorganization energy. Over the last few decades, many experiments were performed to test this prediction of the Marcus theory.

One of the first systematic attempts to observe this phenomenon was published by Rehm and Weller in 1970.[52] They reported the fluorescence quenching rate constants between more that 60 organic donor-acceptor pairs covering a wide range of driving forces in acetonitrile. The authors did not observe any signs of the existence of the inverted region and concluded that the maximum of bimolecular electron transfer rate is diffusion limited. Their results are shown in Figure 1.11.

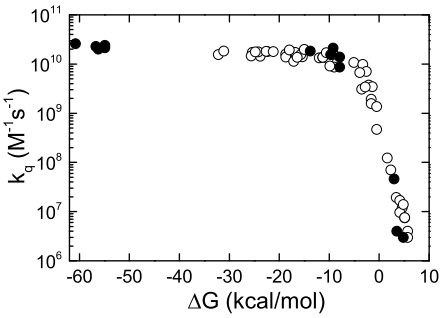

Figure 1.11 Fluorescence quenching rate constants as a function of the free enthalpy. Open circles correspond to the electron transfer between A* and D, and full circles correspond to the ET between D* and A. Adapted from ref.[52]

Miller and co-workers realized that diffusion could bias the observation of the inverted region in bimolecular processes. Therefore, they decided to study ET in a frozen matrix.[80,81] They observed a sharp increase in the charge separation rates with increasing of the driving forces, until the maximum, followed by less steeply decreasing rates, while the reaction exothermicity increased. This could have been the first evidence for Marcus inverted region, but the uncertainty in determining the distance between the donor and acceptor complicated the interpretation of the results. Motivated by results obtained in the frozen samples, Miller et al. expanded their studies to intramolecular long-range electron transfer systems, where the donor and acceptor were rigidly bridged.[60,82] The use of rigid intramolecular system eliminated the problem of the unknown distance between the donor and acceptor, from previous work. They synthesized a series of molecules with the general structure: X-bride-Y, where X is the acceptor, Y is 4-biphenylyl, and the bridge is a rigid saturated hydrocarbon spacer, which keeps X and Y in a constant edge-to-edge distance equal to 10 Å. They observed a relatively fast charge separation ($\sim$ 100 ps) when the reaction conditions were optimized. Most importantly, they showed that with the increase of the driving forces above -1.2 eV, the charge separation rate decreased, and this was the first experimental confirmation of the existence of the so-called inverted region, predicted by Marcus almost 30 years earlier (Figure 1.12). However, the observed dependence did not have a perfect parabolic shape.

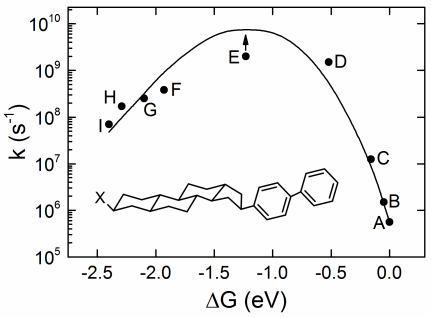

Figure 1.12 Inverted region effect in chemical electron transfer reaction, presented by Miller et al., measured in 2-methyltetrahydrofuran. X represents the electron acceptor: (A) 4-biphenylyl, (B) 2-naphthyl, (C) 9-phenanthryl, (D) 1-pyrenyl, (E) hexahydronaphthoquinon-2-yl, (F) 2-naphthoquinonyl, (G) 2-benzoquinonyl, (H) 5-chlorobenzoquinon-5-yl, (I) 5,6-dichlorobenzoquinon-2-yl. Adapted from ref.[82]

Just one year after this finding, new studies were presented on the Marcus inverted region. Wasielewski and co-workers published studies on a series of porphyrin-quinone donor-acceptor molecules with restricted-distance properties.[83] They showed that in intramolecular systems, an increase of the driving forces of the charge recombination dramatically decreased the rate constant (over two orders of magnitude). Surprisingly, they did not observe the solvent-polarity effect on the CS rate. Gould and co-workers reported an inverted region for a charge recombination rate in the bimolecular electron transfer process.[84,85] They studied systems with driving forces between -2 to -2.9 eV. Recently, a weak inverted region in the dependence of the quenching rate was obtained by Rosspeintner et al.[86] It was found that the intrinsic rate constant of the bimolecular electron transfer is almost 2 orders of magnitude faster that the diffusion rate constant. However, the changes in charge separation vs. driving forces are less pronounced than expected from Marcus theory.

The inverted region was clearly observed for almost all types of electron transfer reactions, with the exceptions for bimolecular charge separation. Successful observation of the inverted regime was performed for systems with exothermicities between -3 eV and -1 eV. In contrast, some studies[87–90] show different behavior of the rate constants vs free energy when the exothermicity of the system is more negative than -3 eV. Kadhum and Salmon observed an increase of the rates attachment of solvated electrons to arenes in very exothermic reaction in tetrahydrofuran.[87] Serpa et al., studied charge recombination rates in CIP, which were formed between nitriles and aromatic hydrocarbons in various solvents and supercritical CO_2.[89,90] They showed that the rates follow Marcus inverted region until the driving forces reach -70 kcal/mol (-3 eV). Upon increasing of the exothermicity, the charge recombination rates increased, what they called as “double inverted region”. They concluded that for sufficiently exothermic reactions, the reorganization energy increases and controls the reactivity, causing the end of inverted region. Their experimental results were well supported by the Intersecting-State Model (for a description of the model see Section 1.5.4). They also reported the lack of the solvent-polarity dependence

on electron transfer rate.[90]

According to the classical theory, the activation barrier should increase in the inverted region while the exothermicity of the system increases. This suggests that a temperature-dependence on the ET rate should be observed. Marcus theory gives a qualitative description of the temperature dependence on the rates in the normal region but it was found that it fails to explain temperature independence in very exothermic reaction in bimolecular[90] and intramolecular systems.[91–93] Kroon and co-workers have found that the charge separation rate is temperature independent in the inverted region, due to the dominant nuclear tunneling effect.[92] Additionally, the temperature independence for the CS rates, and unexpected increase of the CR rates with lowering the temperature was reported by Lemmetyinen and co-workers.[94] In the inverted region the reaction is barrierless. Sukegawa et. al. observed weak inverted temperature-dependence of the charge recombination rate in rigid donor-bridge-acceptor systems, where π-conjugated wires played the role of the bridge.[59] The authors assumed that the increased rates with decreased temperatures, corresponded to the lowering of the activation barrier, by the existence of an additional pathway of transferring electron such as inelastic tunneling. The tunneling mechanism is more probably in a long-distance rigid molecule, than in a flexible system, where competitive thermally activated hopping may occur. All these studies agreed that in the inverted region, the quantum-mechanical treatment of high-frequency modes can not be ignored.

It is of great interest to expand the studies for system with even higher exothermicities (below -85 kcal/mol), and study the behavior of charge recombination rates in the inverted region for a wide range of temperatures. Such studies are expected to give information on the approximations of the Marcus theory used to describe the rates of electron transfer reactions.

1.5.2.4 Problems with Marcus Theory

Marcus theory is widely used as the basic explanation for electron transfer processes. However, a closer comparison of experimental results with theoretical predictions, reveals that Marcus theory has few major problems:

1. The approximation of near adiabaticity for electron transfer processes is difficult to obtain for most reactions.

2. Equation 1.23 may be used just for reaction occurring at high temperatures. According to this equation, electron transfer vanishes at low temperatures and has high barriers in the inverted region.

3. Although the inverted region was observed, the falloff was not as pronounced as predicted from the theory. It does not present a symmetrical parabolic behavior.

4. Recently, it was reported "the end" of inverted region for very exothermic reactions, followed by the existence of new "normal region".

5. It was found that the solvent reorganization energy is overestimated by a factor of two for weakly polar and polar solvents.

6. Absence of the solvent-polarity effect in the electron transfer rate was reported.

7. According to the classical Marcus theory, the barrier can only be overcome by passing over the barrier, but tunneling processes have been reported (see Section 1.5.3).

8. The rates in the inverted region are essentially temperature independent.

1.5.3 Semi-Classical and Nuclear Tunneling Theories

In classical electron transfer theory, the electronic transmission coefficient is assumed to be close to unity. However, many ET reactions are non-adiabatic ($\kappa \leqslant 1$), therefore the role of electronic coupling (V) needs to be specified. Additionally, the theory should include the contribution from quantum high-frequency modes, by a quantum mechanical treatment which is more general than Marcus theory.

The ET rates can be expressed as the product between the electronic coupling strength between donor and acceptor and a Franck-Condon weighted density of states (FCWD) using Fermi Golden Role expressed in equation 1.22. For the case of displaced oscillators with frequencies ω_i and reduced masses μ_i identical in the initial and final states, the Franck-Condon factor is a convolution between line shape integrals corresponding to the contributions of the solvent mode (subscript s) and of one higher frequency molecular vibrational mode (subscript ν), that can be expressed as:[38,95]

$$FCWD = \frac{1}{\hbar\omega_s} exp\left[-S_s(2\bar{n}_s+1) - S_\nu(2\bar{n}_\nu+1)\right] \sum_{m=-\infty}^{+\infty} \left(\frac{\bar{n}_s+1}{\bar{n}_s}\right)^{p(m)/2} \times I_{|p(m)|}\left(2S_s\sqrt{\bar{n}_s(\bar{n}_s+1)}\right)\left(\frac{\bar{n}_\nu+1}{\bar{n}_\nu}\right)^{m/2} I_m\left(2S_\nu\sqrt{\bar{n}_\nu(\bar{n}_\nu+1)}\right) \quad (1.29)$$

where $\Delta E = -\Delta G^0$ because the frequencies were assumed not to change, $p(m) = (\Delta E - m\hbar\omega_v)/\hbar\omega_s$ is taken as an integer closest to the value of $p(m)$, $I_x(z)$ is the modified Bessel function, the average quantum number of an ensemble of identical oscillators in thermal equilibrium is:

$$\bar{n}_s = \left[exp\left(\frac{\hbar\omega_s}{k_B T}\right) - 1\right]^{-1} \qquad \bar{n}_\nu = \left[exp\left(\frac{\hbar\omega_\nu}{k_B T}\right) - 1\right]^{-1} \quad (1.30)$$

or

$$\frac{\bar{n}+1}{\bar{n}} = \left(\frac{\hbar\omega}{k_B T}\right) \quad (1.31)$$

and the electron-phonon couplings (Huang-Rhys parameters) are $S_s = \lambda_s/\hbar\omega_s$ and $S_\nu = \lambda_\nu/\hbar\omega_\nu$. The frequency ω_s corresponds to a solvent mode, or a group of solvent modes with identical frequencies, and may take values close to 10 cm^{-1}. In low temperatures $k_BT \gg \hbar\omega_s$ and the following limits apply[38,95]

$$\sqrt{\bar{n}_s\left(\bar{n}_s+1\right)} \rightarrow \frac{k_BT}{\hbar\omega_s} \tag{1.32}$$

$$2\sqrt{\bar{n}_s\left(\bar{n}_s+1\right)} - \left(2\bar{n}_s+1\right) \rightarrow \frac{\hbar\omega_s}{4k_BT} \tag{1.33}$$

$$I_{|p(m)|}(z) \rightarrow \frac{1}{\sqrt{2\pi z}} exp\left[z - \frac{[p(m)]^2}{2z}\right] \tag{1.34}$$

where an asymptotic expansion of Bessel function for the solvents modes was made because of the large values of its argument. This asymptotic limit corresponds to a Gaussian line shape function, which supports a classical treatment of the medium modes.

When $S_s \rightarrow 0$ (*i.e.*, $\lambda_s \rightarrow 0$) and only $m = 0$ contributes in equation 1.29, a simple relation is derived[95]

$$FCWD = \frac{1}{\hbar\omega_s} exp\left[-S_v\left(2\bar{n}_\nu+1\right)\right]\left(\frac{\bar{n}_\nu+1}{\bar{n}_\nu}\right)^{p/2} I_p\left(2S_\nu\sqrt{\bar{n}_\nu\left(\bar{n}_\nu+1\right)}\right) \tag{1.35}$$

or

$$k = \frac{2\pi}{\hbar}\left|V^2\right|\frac{1}{\hbar\omega_s} exp\left[-S_\nu\left(2\bar{n}_\nu+1\right)\right]\left(\frac{\bar{n}_\nu+1}{\bar{n}_\nu}\right)^{p/2} I_p\left(2S_\nu\sqrt{\bar{n}_\nu\left(\bar{n}_\nu+1\right)}\right) \tag{1.36}$$

where $p = \Delta E/\hbar\omega_s$. This equation exhibits the Poisonian-type function.[95]

At the low temperature limit, when $k_BT \ll \hbar\omega_\nu$, $n_\nu \rightarrow 0$, and the limiting form of the Bessel function for small values of the argument can be used

$$I_p(z) \rightarrow \frac{1}{p!}\left(\frac{z}{2}\right)^p \tag{1.37}$$

Using these approximations, equation 1.35 and 1.36 simplifies to

$$FCWD = \frac{1}{\hbar\omega_s} exp\left[-S_\nu\right] \frac{S_\nu^p}{p!} \tag{1.38}$$

or

$$k = \frac{2\pi}{\hbar} \left|V^2\right| \frac{1}{\hbar\omega_s} exp\left[-S_\nu\right] \frac{S_\nu^p}{p!} \tag{1.39}$$

The frequency ω_ν is often taken as an averaged vibrational mode of donor and acceptor centers,[96] and vibrational frequencies of 1500 cm^{-1} are used to represent aromatic donors and acceptors.[60] Eq. 1.39 shows finite temperature-independent nuclear tunneling rate at low temperatures.

Using the relation between the angular frequency of oscillation and the harmonic force constant of the vibrational mode, $\omega_\nu = \sqrt{f/\mu}$, and the relation of the molecular vibrational reorganization energy (λ_ν) with the horizontal displacement (d) of the vibrational mode between the initial and the final state, $\lambda_\nu = fd^2/2$, it is also useful to write

$$S_\nu = \frac{d\sqrt{\lambda_\nu \mu}}{\hbar\sqrt{2}} \tag{1.40}$$

It is easy to show that when equation 1.39 is used together with 1.22 for a symmetrical reaction ($\Delta E = 0$, $p = 0$, $\Delta E^\ddagger = \lambda_\nu/4$), and equation 1.40 is used for S_ν, the ET rate is given by[97]

$$k = \nu exp\left[-\frac{d\sqrt{2\mu\Delta E^\ddagger}}{\hbar}\right] \tag{1.41}$$

Equation 1.41 was first derived by Formosinho in 1974,[39] that presented it in a more general form, also valid for exothermic reactions. He noticed that previous theories for nuclear tunneling did not allow the correct estimation of the rates because of the incorrect assumptions about the nature of the potential surfaces. Formosinho

also pointed out that the expression $(V(x) - E)^{\frac{1}{2}}$ from equation 1.4 is of a triangular shape for an isoenergetic reaction, and that the nuclear tunneling rate can be expressed by:

$$k = \nu exp\left[-\frac{\Delta x\sqrt{2\mu\Delta E^{\ddagger}}}{\hbar}\right] \tag{1.42}$$

where the barrier width Δx is the horizontal distance between the turning points of vibration of the oscillator in the initial and final states of a radiationless transition. For displaced harmonic oscillators with the same frequency in the initial and final states,

$$\Delta x = d - \sqrt{\frac{2\,|\Delta E|}{f}} \tag{1.43}$$

Equations 1.41 and 1.42 are particular cases of the WKB approximation for nuclear tunneling through a barrier formed by intersecting parabolas with their minima separated by a displacement d. In order to calculate the ET rate constant, it is necessary to evaluate the reduced mass μ. The case of benzene (Figure 1.13) illustrates how to calculate μ.

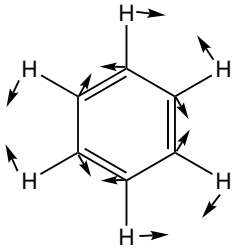

Figure 1.13 Asymmetric CC stretching mode of benzene emphasizing the presence of 3 CC oscillators.

The asymmetric CC stretching mode of benzene is observed at 1309 cm^{-1} and can be reproduced with a harmonic force field using a CC stretching mode with a force constant $f_{CC} \approx 6.6\,aJ/\AA^2 \approx 950$ kcal/(mol $\AA^2$).[98] This vibration of the benzene ring in Figure 1.13 is also described as the Kekulé mode. This representation of the asymmetric CC stretching mode reveals that three CC oscillators are

simultaneously being displaced from their equilibrium positions and involved in the transfer of benzene from the initial to the final state. Hence, in a first approximation, the reduced mass in equation 1.42 must be $\mu_{benzene} = 3\mu_{CC}$. However, eq. 1.42 was derived for radiationless transitions in a given molecule,[39] while in ET two molecules are involved (or two independent moieties is the same molecule). Within the approximations used to derive equation 1.29, the identical and similarly displaced oscillators involved in the transitions in these moieties have the same frequencies and reduced masses. Hence, the barriers $\Delta E^{\ddagger}$ are the same for all the oscillators and the total reduced mass for the hypothetical case of two benzene molecules exchanging an electron is $\mu = \left[(\mu_{benzene})^{1/2} + (\mu_{benzene})^{1/2}\right]^2$. In general the reduced mass of the donor-acceptor system is

$$\mu = \left(\sqrt{\mu_{donor}} + \sqrt{\mu_{acceptor}}\right)^2 \tag{1.44}$$

Another particular case of equation 1.29 was derived without neglecting the effect of the solvent but under the approximation $\hbar\omega_s \ll k_B T \ll \hbar\omega_\nu$, i.e. n_s is a large number and $n_\nu \to 0$. The solvent contribution is treated classically while the donor and acceptor mode (represented by the averaged frequency $\hbar\omega_\nu$) is quantized. Equation 1.29 with $p(m) = (\Delta E - m\hbar\omega_\nu)/\hbar\omega_s$ and with the approximations of equations 1.32-1.34 for the solvent modes and of eq. 1.36 for the donor and acceptor modes, gives[72,96,99,100]

$$k = \frac{2\pi}{\hbar}\left|V^2\right| \frac{1}{\sqrt{2\pi\lambda_s k_B T}} exp\left(-S_\nu\right) \sum_{m=0}^{+\infty} exp\left[-\frac{\left(\Delta G^0 + \lambda_s + m\hbar\omega_\nu\right)^2}{4\lambda_s k_B T}\right] \frac{S_\nu^m}{m!} \tag{1.45}$$

The presence of the nuclear quantum effects changes the free-energy relations in the inverted region. The high-frequency intramolecular vibrational excitations of quantum modes lead to lowering of the E_a and decrease the effective free-energy gap. In consequence, the decrease of the ET rates with increasing ΔG^0 is less pronounced than predicted by Marcus.

In the high-temperature limit, when $\hbar\omega_s \ll \hbar\omega_\nu \ll k_B T$, the semi-classical rate is obtained

$$k = \frac{2\pi}{\hbar}\left|V^2\right| \frac{1}{\sqrt{2\pi\lambda k_B T}} exp\left[-\frac{\left(\Delta G^0 + \lambda\right)^2}{4\lambda k_B T}\right] \tag{1.46}$$

where $\lambda = \lambda_s + \lambda_\nu$ is the sum of the solvent and molecular reorganization energies, respectively. Equation 1.46 leads to an inverted parabola dependence of $log(k)$ on ΔG^0, and is analogues to Marcus theory. The ET rate at high temperature limit is thermally activated.

The calculation of the ET rate using the equations above relies on estimates of the normal mode displacement d, which is related to the change of the equilibrium positions Δq_i of the normal modes (i.e. to the bond-length changes due to electron transfer), and on the corresponding normal mode harmonic frequencies, to calculate the molecular vibrational reorganization energy

$$\lambda_\nu = \frac{1}{2}\sum_i \mu_i \omega_i^2 \left(\Delta q_i\right)^2 \tag{1.47}$$

In the single high-frequency approximation used above, a weighted average over the strongly coupling modes ω_ν is employed rather than a normal mode frequency. The bond length changes are then obtained for the donor or the acceptor from the mean square displacement[39,101,102]

$$d_{D/A} = \left(\sum_i \left(\Delta q_i\right)^2\right)^{1/2} \tag{1.48}$$

and the sum of the displacements of donor and acceptor is $d = d_A + d_D$. The value of d can be obtained from the equation above when the changes in bond lengths are known. Electronic structure calculations are often used to calculate the equilibrium structures of donor and acceptor before and after the transfer of the electron, which provides the basis to calculate each Δq_i relevant for eq. 1.48.

1.5.4 Intersecting-State Model

Formosinho and Varandas proposed a theoretical model which describes the relationship between the energy barrier and transition-state bond extensions in 1986.[103] In this model, called Intersecting-State Model (ISM), the displacement d can be calculated as the sum of the displacements of the reactants and products from their equilibrium positions to their transition state configurations.

The major difference between the ISM and estimates of d by eq. 1.48 is that the ISM accounts for a possible increase of the reorganization energy with the driving force of the reaction, expressed as:[41]

$$d = \frac{a'}{2n^{\ddagger}} ln \left[\frac{1+g}{1-\left(\frac{1}{1+g}\right)} \right] (l_{r,eq} + l_{p,eq}) \tag{1.49}$$

with

$$g = exp\left(\frac{\sqrt{2n^{\ddagger}}\Delta G^0}{\Lambda} \right) \tag{1.50}$$

where a'=0.156 is the scaling factor, $n^{\ddagger}$ is the transition state bond order, Λ is the dynamic parameter and $l_{r,eq}/l_{p,eq}$ are the effective equilibrium bond lengths of the reactants/products, which can be expressed as $l_{eq} = (l_{red} + l_{ox})/2$. For the ET reactions which do not involve bond-breaking or bond-forming, the $n^{\ddagger}$ is just the bond order of the relevant bonds. For example, $n^{\ddagger} = 1.5$ for benzene, $n^{\ddagger} = 2.0$ for dicyanoethene, and $n^{\ddagger} = 1.75$ for a benzene/dicyanoethene pair. The parameter Λ regulates the dissipation of excess ΔG^0 by the accepting modes, that may lead to additional bond extensions not accounted by eq. 1.48. This becomes especially relevant for very exothermic reactions.

When $\Lambda \gg |\Delta G^0|$, the d is independent of the reaction energy,[100] and has constant value which can be expressed as the sum of bond extensions of reactants and products:[41,90,104,105]

$$d = \frac{a' ln\,(2)}{n^{\ddagger}} (l_{r,eq} + l_{p,eq}) \tag{1.51}$$

The rate constant for a thermally-activated ET can be calculated from the intersection of the reactant and product oscillators curves knowing the horizontal displacement (d) and the vertical displacement (ΔG^0), that corresponds to the reactant displacement:

$$\Delta x_{th} = \frac{d}{2} - \frac{\Delta G^0}{df} \tag{1.52}$$

where f is the force constant. The above equation allows the estimation of ΔG_{act}:

$$\Delta G_{act} = \frac{1}{2} f d^2 \tag{1.53}$$

and, subsequently, the tunneling rate can be calculated with eq. 1.42 and the thermally activated rate from:

$$k_{th} = \nu exp\left(-\frac{\Delta G_{act}}{RT}\right) \tag{1.54}$$

Thermally activated or tunneling rates obtained via ISM depend on i) driving forces, ii) force constants of bond-forming and bond-breaking process, iii) and the horizontal displacement, d, of the oscillators. The last factor includes a free energy dependence (eq.1.49-1.50) that is ignored in other theories and may play a dominant role in the free-energy of ET rates as shown by Formosinho.[106] A non-specific solvent reorganization contribution to the ΔG_{act} is neglected by Intersecting-State Model.

Figure 1.14 shows the changes in the reaction coordinate with the increasing exothermicity of the reaction, together with the changes in λ. In the inverted region, the overlap between the nuclear wavefunction of the reactants and the higher vibrational states of the product state is larger, and the tunneling rates are higher than the thermally activated rates.

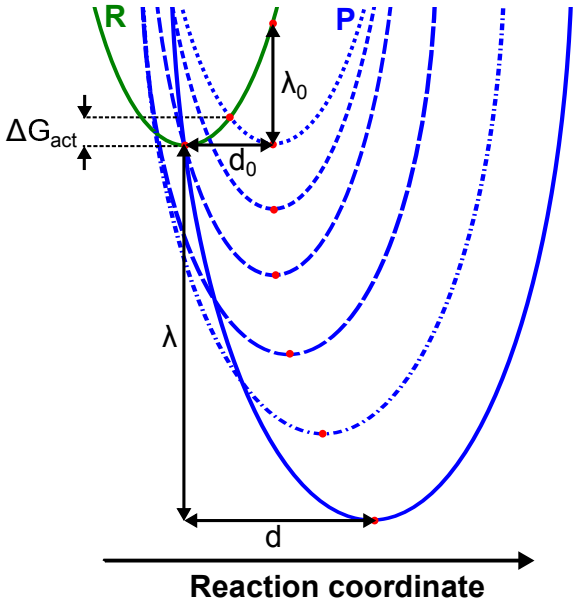

Figure 1.14 Free energy diagram, accounting for the changes in reorganization energy, according to the ISM.

The ISM was first applied in the calculation of the activation energies in the hydrogen atom gas-phase reaction, and later expanded to other types of reaction. It was successfully applied in proton transfer reactions[107,108] and was tested in nucleophilic substitution reactions in enzyme catalysis.[109] Applications of ISM to electron transfer reactions have been extensively published.[41,88–90,110–112] The Intersecting-State Model predicted the existence of a "double inverted region", which shows a new increase in the rates for very exothermic reactions ($> -75\,\mathrm{kcal/mol}$).[113]

1.6 Aim of the Work

As presented in previous sections, electron transfer is a process of great importance in nature and in artificial systems. However, the mechanism behind this seemingly simple process is not fully understood. With the intention to contribute to a better understanding of the electron transfer process, we studied bimolecular and intramolecular system with large driving forces.

The thesis has been divided into five parts (chapter 2-6). In **chapter 2** the materials and methods used are presented.

Chapter 3 examines the photoinduced bimolecular electron transfer between aromatic donors in the presence of fumaronitrile. The generated charge-transfer state is an emissive species in most studied solvents. This enabled the characterization of the systems with steady-state fluorescence and time-correlated techniques. The formation of CIP and LIP is discussed.

Chapter 4 concerns the studies of intramolecular electron transfer in rigidly bridged donor-acceptor systems in weakly polar solvents. Molecules 3-methoxy-1,3,5(10)-estratrien-17-yliden) malononitrile (**1**) and 1,3,5(10)-estratrien-17-yliden) malononitile (**2**) were chosen because of structural properties suitable to the free-energy and temperature dependence studies. Molecules **1** and **2** show a relatively short separation between redox groups (r_{e-e} = 5.9Å) and contain all-trans saturated C-C bonds. The rigid bridge assures a constant separation distance and orientation during the studied processes. Therefore, electron transfer should occur just through-bond interaction. The redox groups were chosen to observe charge separation and charge recombination in a wide range of exothermicities. The objective was to investigate the real effect of tunneling, electron spin and solvent on the charge recombination rate in the inverted region. The influence of the bridge presence on the rate constant in comparison with the bimolecular system was also studied. The bimolecular electron transfer between 3,4-dimethylanisole and o-xylene acting as a donors and isopropylidenomalononitrile as an acceptor was investigated. In this case, the resulting charge-transfer state does not emit light. Therefore, femtosecond

spectroscopy was used to obtain new insight in the investigation of bimolecular PET. The temperature-dependence studies on charge recombination in molecules **1** and **2** were also performed.

In **Chapter 5**, the charge separation and charge recombination rates for molecules **1** and **2** and for the corresponding bimolecular systems in polar solvents are presented. The results obtained are briefly compared with the ones from weakly polar solvents.

Additionally, in the chapters 3-5, the reliability of the theoretical predictions are tested by comparing the experimental results with the electron transfer theories. General conclusions are summarized in the **Chapter 6**.

References

1. IUPAC, *Compendium of Chemical Terminology ("Golden Book")*, Blackwell Scientific Publications, Oxford, 2nd edn, 1997.

2. R. E. Blankenship and W. W. Parson, *Annu. Rev. Biochem.*, 1978, **47**, 635–653.

3. R. K. Clayton, *Photosynthesis: Physical Mechanisms and Chemical Pattern.*, Cambridge Univ. Press, Cambridge, 1980.

4. J. Blumberger, *Chem. Rev.*, 2015, **115**, 11191–11238.

5. D. Zhong, *Annu. Rev. Phys. Chem.*, 2015, **66**, 691–715.

6. O. B. Morozova, N. N. Fishman and A. V. Yurkovskaya, *Zeitschrift für Phys. Chemie*, 2016, **231**, 479–495.

7. M. M. Delmastro-Greenwood and J. D. Piganelli, *Am. J. Clin. Exp. Immunol.*, 2013, **2**, 30–54.

8. B. C. Smith, E. S. Underbakke, D. W. Kulp, W. R. Schief and M. A. Marletta, *Proc. Natl. Acad. Sci. U. S. A.*, 2013, **110**, E3577–E3586.

9. H. B. Gray and W. R. J. Ellis, *Bioinorg. Chem.*, University Science Books, Mill Valley, 1994, vol. 68, ch. 6, pp. 315–363.

10. A. W. Castleman, Q. Zhong and S. M. Hurley, *Proc. Natl. Acad. Sci. U. S. A.*, 1999, **96**, 4219–4220.

11. B. P. Karsten, R. K. M. Bouwer, J. C. Hummelen, R. M. Williams and R. A. J. Janssen, *J. Phys. Chem. B*, 2010, **114**, 14149–14156.

12. M. Mollahosseini, E. Karunaratne, G. N. Gibson, J. A. Gascón and F. Papadimitrakopoulos, *J. Am. Chem. Soc.*, 2016, **138**, 5904–5915.

13. J. Otsuki, T. Akasaka and K. Araki, *Coord. Chem. Rev.*, 2008, **252**, 32–56.

14. C. Schubert, J. . T. Margraf, T. Clark and D. M. Guldi, *Chem. Soc. Rev.*, 2015, **44**, 988–998.

15. M. Mehring, *Int. J. Electron.*, 1992, **73**, 1073–1083.

16. A. Fujishima and K. Honda, *Nature*, 1972, **238**, 37–38.

17. M. Barroso, C. A. Mesa, S. R. Pendlebury, A. J. Cowan, T. Hisatomi, K. Sivula, M. Grätzel, D. R.Klug and J. R. Durrant, *Proc. Natl. Acad. Sci. U. S. A.*, 2012, **109**, 15640–15645.

18. S. Berardi, G. La Ganga, M. Natali, I. Bazzan, F. Puntoriero, A. Sartorel, F. Scandola, S. Campagna and M. Bonchio, *J. Am. Chem. Soc.*, 2012, **134**, 11104–11107.

19. A. G. Griesbeck, M. Oelgemöller and J. Lex, *J. Org. Chem.*, 2000, **65**, 9028–9032.

20. A. G. Griesbeck, T. Heinrich, M. Oelgemöller, J. Lex and A. Molis, *J. Am. Chem. Soc.*, 2002, **124**, 10972–10973.

21. U. C. Yoon, Y. X. Jin, S. W. Oh, C. H. Park, J. H. Park, C. F. Campana, X. Cai, E. N. Duesler and P. S. Mariano, *J. Am. Chem. Soc.*, 2003, **125**, 10664–10671.

22. A. Bauer, F. Westkämper, S. Grimme and T. Bach, *Nature*, 2005, **436**, 1139–1140.

23. R. A. Marcus, *J. Chem. Phys.*, 1965, **43**, 2654–2657.

24. D. M. Hercules, *Acc. Chem. Res.*, 1969, **2**, 301–307.

25. A. P. Castano, T. N. Demidova and M. R. Hamblin, *Photodiagnosis Photodyn. Ther.*, 2004, **1**, 279–293.

26. M. Pineiro, A. L. Carvalho, M. M. Pereira, A. M. d'A. Rocha Gonsalves, L. G. Arnaut and S. J. Formosinho, *Chem. - A Eur. J.*, 1998, **4**, 2299–2307.

27. J. M. Dąbrowski, M. M. Pereira, L. G. Arnaut, C. J. P. Monteiro, A. F. Peixoto, A. Karocki, K. Urbańska and G. Stochel, *Photochem. Photobiol.*, 2007, **83**, 897–903.

28. E. F. F. Silva, C. Serpa, J. M. Dąbrowski, C. J. P. Monteiro, S. J. Formosinho, G. Stochel, K. Urbańska, S. Simões, M. M. Pereira and L. G. Arnaut, *Chem. - A Eur. J.*, 2010, **16**, 9273–9286.

29. J. W. Ondersma and T. W. Hamann, *J. Am. Chem. Soc.*, 2011, **133**, 8264–8271.

30. B. H. Farnum, Z. A. Morseth, M. K. Brennaman, J. M. Papanikolas and T. J. Meyer, *J. Am. Chem. Soc.*, 2014, **136**, 15869–15872.

31. R. Hubert, L. Dworak, J. E. Moser, M. Grätzel and J. Wachtveitl, *J. Phys. Chem. C*, 2016, **120**, 8534–8539.

32. J. Franck, *Trans. Faraday Soc.*, 1924, 536–542.

33. E. Condon, *Phys. Rev.*, 1926, **28**, 1182–1201.

34. E. U. Condon, *Phys. Rev.*, 1928, **32**, 858–872.

35. G. Gamow, *Nature*, 1928, **122**, 805–806.

36. G. Gamow, *Zeitschrift für Phys.*, 1928, **51**, 204–2012.

37. R. W. Gurney and E. U. Condon, *Nature*, 1928, **122**, 439.

38. D. Devault, *Q. Rev. Biophys.*, 1980, **13**, 387–564.

39. S. J. Formosinho, *J. Chem. Soc. Faraday Trans. II*, 1974, **70**, 605–620.

40. M. D. Newton and N. Sutin, *Annu. Rev. Phys. Chem.*, 1984, **35**, 437–480.

41. S. J. Formosinho, L. G. Arnaut and R. Fausto, *Prog. React. Kinet.*, 1998, **23**, 1–90.

42. L. G. Arnaut and S. J. Formosinho, *J. Photochem. Photobiol. A Chem.*, 1996, **100**, 15–34.

43. A. Jabłoński, *Nature*, 1933, 839–840.

44. M. Montalti, L. Prodi, A. Credi and M. T. Gandolfi, *Handbook of Photochemistry*, CRC Press, 3rd edn, 2006.

45. D. M. E. Freeman, A. J. Musser, J. M. Frost, H. L. Stern, A. K. Forster, K. J. Fallon, A. G. Rapidis, F. Cacialli, I. Mcculloch, T. M. Clarke, R. H. Friend and H. Bronstein, *J. Am. Chem. Soc.*, 2017, **139**, Just accepted.

46. U. Steiner, *Zeitschrift fur Naturforsch. A J. Phys. Sci.*, 1979, **34**, 1093–1098.

47. I. R. Gould, J. A. Boiani, E. B. Gaillard, J. L. Goodman and S. Farid, *J. Phys. Chem. A*, 2003, **107**, 3515–3524.

48. Z. E. X. Dance, S. M. Mickley, T. M. Wilson, A. B. Ricks, A. M. Scott, M. A. Ratner and M. R. Wasielewski, *J. Phys. Chem. A*, 2008, **112**, 4194–4201.

49. D. L. Dexter, *J. Chem. Phys.*, 1953, **21**, 836–850.

50. T. Förster, *Faraday Discuss. Chem. Soc.*, 1959, **27**, 7–17.

51. A. Weller, *Zeitschrift für Phys. Chemie*, 1982, **133**, 93–98.

52. D. Rehm and A. Weller, *Isr. J. Chem.*, 1970, **8**, 259–271.

53. H. Oevering, M. N. Paddon-Row, M. Heppener, A. M. O. Oliver, E. Cotsaris, J. W. Verhoeven and N. S. Hush, *J. Am. Chem. Soc.*, 1987, **109**, 3258–3269.

54. A. M. Kuznetsov and J. Ulstrup, *J. Chem. Phys.*, 1981, **75**, 2047–2055.

55. G. L. Closs, L. T. Calcaterra, N. J. Green, K. W. Penfield and J. R. Miller, *J. Phys. Chem.*, 1986, **90**, 3673–3683.

56. R. J. Cave, P. Siders and R. A. Marcus, *J. Phys. Chem.*, 1986, **90**, 1436–1444.

57. J. R. Miller, *Electron Transf. Inorganic, Org. Biol. Syst.*, 1991, pp. 265–276.

58. N. R. Lokan, M. N. Paddon-Row, M. Koeberg and J. W. Verhoeven, *J. Am. Chem. Soc.*, 2000, **122**, 5075–5081.

59. J. Sukegawa, C. Schubert, X. Zhu, H. Tsuji, D. M. Guldi and E. Nakamura, *Nat. Chem.*, 2014, **6**, 899–905.

60. G. L. Closs and J. R. Miller, *Science*, 1988, **240**, 440–447.

61. O. S. Wenger, *Acc. Chem. Res.*, 2011, **44**, 25–35.

62. M. J. Shephard and M. N. Paddon-Row, *J. Phys. Chem. A*, 1999, **103**, 3347–3350.

63. P. Pasman, G. F. Mes, N. W. Koper and J. W. Verhoeven, *J. Am. Chem. Soc.*, 1985, **107**, 5839–5843.

64. M. B. Zimmt and D. H. Waldeck, *J. Phys. Chem. A*, 2003, **107**, 3580–3597.

65. I. R. Gould, R. H. Young, R. E. Moody and S. Farid, *J. Phys. Chem.*, 1991, **95**, 2068–2080.

66. I. R. Gould, D. Ege, J. E. Moser and S. Farid, *J. Am. Chem. Soc.*, 1990, **112**, 4290–4301.

67. E. Winstein, E. Clippinger, A. H. Fainberg, R. Heck and G. C. Robinson, *J. Am. Chem. Soc.*, 1955, **78**, 328–335.

68. G. J. Kavarnos and N. J. Turro, *Chem. Rev.*, 1986, **86**, 401–449.

69. E. Lippert, *Zeitschrift fur Naturforsch. A J. Phys. Sci.*, 1955, **10**, 541–545.

70. N. Mataga, Y. Kaifu and M. Koizumi, *Bull. Chem. Soc. Jpn.*, 1955, **28**, 690–691.

71. D. Veldman, S. M. A. Chopin, S. C. J. Meskers and R. A. J. Janssen, *J. Phys. Chem. A*, 2008, **112**, 8617–8632.

72. R. A. Marcus and N. Sutin, *Biochim. Biophys. Acta*, 1985, **811**, 265–322.

73. R. A. Marcus, *J. Chem. Phys.*, 1956, **24**, 966–978.

74. R. A. Marcus, *Annu. Rev. Phys. Chem.*, 1964, **15**, 155.

75. X.-Y. Li, *Int. J. Quantum Chem.*, 2015, **115**, 700–721.

76. M. D. Johnson, J. R. Miller, N. S. Green and G. L. Closs, *J. Phys. Chem.*, 1989, **93**, 1173–1176.

77. M. D. Newton, M. V. Basilevsky and I. V. Rostov, *Chem. Phys.*, 1998, **232**, 201–210.

78. R. A. Marcus, *Discuss. Faraday Soc.*, 1960, **29**, 21–31.

79. R. A. Marcus, *Angew. Chemie, Int. Ed.*, 1993, **32**, 1111–1121.

80. J. V. Beitz and J. R. Miller, *J. Chem. Phys.*, 1979, **71**, 4579–4595.

81. J. R. Miller, J. V. Beitz and R. K. Huddleston, *J. Am. Chem. Soc.*, 1984, **106**, 5057–5068.

82. J. R. Miller, L. T. Calcaterra and G. L. Closs, *J. Am. Chem. Soc.*, 1984, **106**, 3047–3049.

83. M. R. Wasielewski, M. P. Niemczyk, W. A. Svec and E. B. Pewitt, *J. Am. Chem. Soc.*, 1985, **107**, 1080–1082.

84. I. R. Gould, D. Ege, S. L. Mattes and S. Farid, *J. Am. Chem. Soc.*, 1987, **109**, 3194–3196.

85. I. R. Gould, R. Moody and S. Farid, *J. Am. Chem. Soc.*, 1988, **110**, 1242–1244.

86. A. Rosspeintner, G. Angulo and E. Vauthey, *J. Am. Chem. Soc.*, 2014, **136**, 2026–2032.

87. A. A. H. Kadhum and G. A. Salmon, *J. Chem. Soc. Faraday Trans. 1*, 1986, **82**, 2521–2530.

88. C. Serpa and L. G. Arnaut, *J. Phys. Chem. A*, 2000, **104**, 11075–11086.

89. C. Serpa, P. J. S. Gomes, L. G. Arnaut, S. J. Formosinho, J. Pina and J. S. De Melo, *Chem. - A Eur. J.*, 2006, **12**, 5014–5023.

90. C. Serpa, P. J. S. Gomes, L. G. Arnaut, J. S. De Melo and S. J. Formosinho, *Chemphyschem*, 2006, **7**, 2533–2539.

91. N. Liang, J. R. Miller and G. L. Closs, *J. Am. Chem. Soc.*, 1990, **112**, 5353–5354.

92. J. Kroon, H. Oevering, J. W. Verhoeven, J. M. Warman, A. M. Oliver and M. N. Paddon-Row, *J. Phys. Chem.*, 1993, **97**, 5065–5069.

93. M. A. Smitha, E. Prasad and K. R. Gopidas, *J. Am. Chem. Soc.*, 2001, **123**, 1159–1165.

94. H. Lemmetyinen, T. Kumpulainen, M. Niemi, A. Efimov, J. Ranta, K. Stranius and N. V. Tkachenko, *Photochem. Photobiol. Sci.*, 2010, **9**, 949–959.

95. J. Jortner, *J. Chem. Phys.*, 1976, **64**, 4860–4867.

96. M. Bixon and J. Jortner, *J. Phys. Chem.*, 1991, **95**, 1941–1944.

97. J. Jortner and J. Ulstrup, *Chem. Phys. Lett.*, 1979, **63**, 236–239.

98. P. Pulay and G. Fogarasi, *J. Chem. Phys.*, 1981, **74**, 3999–4014.

99. R. A. Marcus and P. Siddarth, *Photoprocesses Transit. Met. Complexes, Biosyst. Other Mol. Exp. Theory*, NATO ASI Series, Kluwer: Dordrecht, 1992, p. 49.

100. L. G. Arnaut, S. J. Formosinho and H. D. Burrows, *Chemical Kinetics*, Elsevier, Amsterdam, 2007.

101. E. F. McCoy and I. G. Ross, *Aust. J. Chem.*, 1962, **15**, 573–590.

102. R. P. van Duyne and S. F. Fischer, *Chem. Phys.*, 1974, **5**, 183–197.

103. A. J. C. Varandas and S. J. Formosinho, *J. Chem. Soc. Faraday Trans. II*, 1986, **82**, 953–962.

104. L. G. Arnaut, A. A. C. C. Pais, S. J. Formosinho and M. Barroso, *J. Am. Chem. Soc.*, 2003, **125**, 5236–5246.

105. L. G. Arnaut and S. J. Formosinho, *Chem. - A Eur. J.*, 2008, **14**, 6578–6587.

106. S. J. Formosinho, *J. Chem. Soc. Perkin Trans. 2*, 1988, 839–846.

107. K. Yates, *J. Phys. Org. Chem.*, 1989, **2**, 300–322.

108. L. G. Arnaut and S. J. Formosinho, *J. Photochem. Photobiol. A Chem.*, 1993, **75**, 1–20.

109. I. V. Trushkov, N. D. Chuvylkin, A. S. Koz'min and N. S. Zefirov, *Russ. Chem. Bull.*, 1995, **44**, 777–800.

110. S. J. Formosinho and L. G. Arnaut, *J. Photochem. Photobiol. A Chem.*, 1994, **82**, 11–29.

111. L. G. Arnaut and S. J. Formosinho, *J. Photochem. Photobiol. A Chem.*, 1998, **118**, 173–181.

112. L. G. Arnaut, A. A. C. C. Pais and S. J. Formosinho, *J. Mol. Struct.*, 2001, **563-564**, 1–17.

113. L. G. Arnaut and S. J. Formosinho, *J. Mol. Struct. THEOCHEM*, 1991, **233**, 209–230.

2 Materials and Methods

2.1 Reagents and Samples

2.1.1 Bimolecular Studies

The 3,4-dimethylanisole (dMA, Aldrich, >99%) and isopropylidenomalononitrile (iPN, TCI Europe, >98%) were used as received. Naphthalene (Np, Aldrich, 99.8%) and pyrene (Py, Aldrich, >99%) were zone-refined. p-Xylene (Xy, Aldrich, 98%) and o-xylene (oXy, Aldrich, 98%) were vacuum distilled. Fumaronitrile (FN, Aldrich, 98%) was vacuum sublimed. Acetonitrile (ACN, HPLC grade), ethyl acetate (EAC, Carlo Erba, ≥99.9%) were used without additional purification. Cyclohexane (CHX, May & Baker, >95%) and n-heptane (HEP, J.T. Baker, >99%) were passed through a silica column. Di-n-buthyl ether (NBE, Acros Organics, ≥99.9%) was washed with diluted NaOH, then washed with water, dried over $CaCl_2$ and distilled. Isopropyl ether (IPE, Merck, 98%) was dried with$CaSO_4$ and passed through the activated alumina column. Chloroform (CHF, Carlo Erba, 99%) was washed with water, dried over $CaCl_2$ and distilled over CaH_2. Tetrahydrofuran (THF) was dried and distilled. 1,2-Dichloroethane (DCE) was distilled. Methyl acetate (MAC, Sigma Aldrich, 99.8%) was distilled after passing through an alumina column.

2.1.2 Intramolecular Studies

Compounds **1** and **2** were provided by Prof. Arménio Serra from the Chemical Engineering Department of University of Coimbra and used as received. The compound characterization is presented in Appendix A.

Acetonitrile (ACN, HPLC grade), ethyl acetate (EAC, Carlo Erba, $\geq$ 99.9%), dichloromethane (DCM, Sigma Aldrich, $\geq$99.9%), and chloroform (CHF, Carlo Erba, 99%) were used without additional purification. Di-n-buthyl ether (DBE, Acros Organics, $\geq$99.9%) was washed with diluted NaOH, then washed with water, dried over $CaCl_2$ and distilled. Isopropyl ether (IPE, Merck, 98%) was dried with$CaSO_4$ and passed through the activated alumina column.

2.2 Methods

2.2.1 Steady-State Absorption and Fluorescence

Absorption spectra were recorded with Shimadzu UV-2100 or Cary spectrometers. Fluorescence spectra were recorded on a Horiba-Jobin-Ivon SPEX Fluorog 3-22 spectrometer. All the fluorescence spectra were corrected for the wavelength response of the system. The low absorbance of studied samples was used to avoid self-absorption or inner filter effects. Temperature control was achieved using a cryostat Optistat DN2 (188-308 K). The maxima of the charge/transfer emission, for the data presented in chapter 3, were obtained after subtracting the scaled monomer emission and fitting a Gaussian function to the CT emission.

2.2.2 Time-Dependent Spectroscopy

2.2.2.1 Femtosecond Pump-Probe Transient Absorption

Experimental details: The amplified femtosecond Spectra-Physic Solstice -100F laser (Ti-sapphire laser, displaying a pulse width of 128 fs and 1 kHZ repetition rate) was used to produce the pump and the probe light. A fraction of the pump pulse at 795 nm passed through a Spectra-Physics TOPAS Prime F Optical Parametric Amplifier, which is responsible for producing tunable radiation between 235 and 22000 nm. The probe light in the UV range was generated by passing part of the 795 nm light from the Solstice-100F laser through a computerized optical delay (with a time window of up to 8 ns) and then focusing in a vertical translating CaF_2 crys-

tal to generate a white-light continuum in the UV-Vis region (340–650 nm), or a sapphire to generate a white-light continuum in the near-infrared spectral region (830-1400 nm). The signal collected by an optic fiber was sent to the broadband (340-1600 nm) HELIOS pump-probe femtosecond transient spectrometer from Ultrafast Systems. The scheme of the femtosecond pump-probe spectrometer is presented on Figure 2.1.

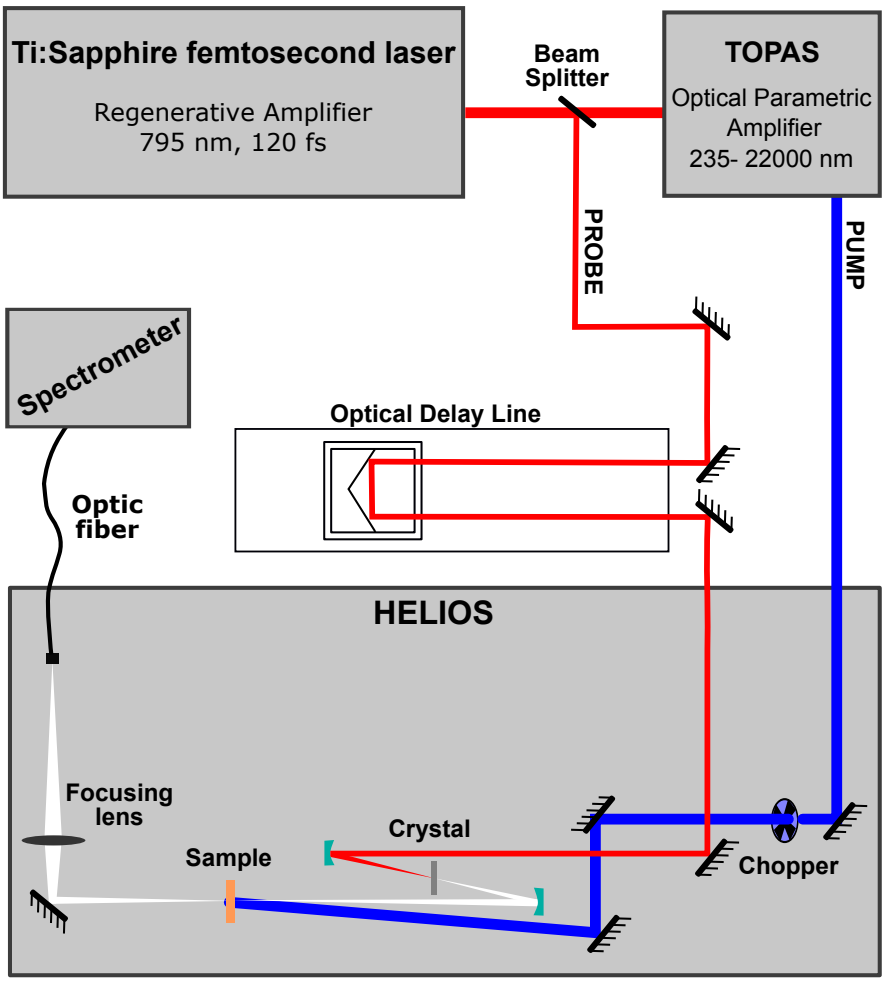

Figure 2.1 Schematic representation of the setup for the femtosecond transient absorption measurement.

All measurements were obtained in 1 or 2 mm quartz cuvettes, with absorption in the range 0.2-0.5 at the pump excitation wavelength. Samples of dMA, molecules **1** and **2** were excited with 283, 287 or 273 nm laser pulses at fluences of 3, 1 or 1.5 µJ/cm^2, respectively. To minimize photodegradation effects, the samples were

kept in movement using a motorized translating sample holder or stirred. The transient spectra were obtained by monitoring the optical density change of freshly prepared samples at 1 nm intervals in the UV-Vis (340-650 nm) and in the NIR (830-1400 nm) range. Depending of the signal quality, between 3 and 30 scans were collected and averaged. Each scan collected around 1000 time points at 310 different wavelengths. The solvent response was obtained in the same experimental conditions as the sample. Temperature control was achieved using a cryostat Optistat DN2 (188-308 K) or a cuvette holder FLASH 300 (253-328 K).

The observed transient absorption signal may contain three contributions:

- excited state absorption (ESA)- observed as a positive signal,
- ground state bleaching (GSB)- observed as a negative signal,
- stimulated emission (SE)- observed as negative signal.

Data analysis: Analysis of the data obtained by femtosecond transient absorption experiment consisted of the following steps:

1. **Subtraction of solvent response**- In the early time delays, a strong nonresonant signal of the solvent was observed. Depending of the solvent, it relaxed up to 1 ps. In order to eliminate this signal, for each one of the experimental conditions employed to study the samples, an experiment was performed with just the solvent in the cuvette. The normalized solvent response was subtracted from the sample data point measured under exactly the same conditions. This signal may affect the ultrafast lifetimes (up to 1.5 ps) for weakly absorbing transient species (which is the case in this work), therefore this value was chosen as the lower detection limit in these studies. The subtraction was performed via Surface Xplorer PRO program from Ultrafast Systems.

2. **Background subtraction-** Data files with a non-zero spectral baseline were corrected by subtracting from the original data the average of a few spectra measured before time zero. The subtraction was performed via Surface Xplorer PRO program.

3. **Chirp correction**- The transient spectra also need to be corrected for the dispersion of the probe light resulting from propagation through the crystal and sample. To perform chirp correction, the non-resonant fitting parameters are needed. They can be obtained automatically, by fitting solvent response function (applicable for all non-polar and middle polarity solvents) or manually, by adjusting time zero for different wavelengths in the studied samples (applicable for samples measured in acetonitrile) by using the Surface Xplorer software.

4. **Global analysis**- The Glotaran program[1] was used to perform global analysis by simultaneous analysis of at least 100 wavelengths. The sequential kinetic scheme with species of increasing lifetimes was used to fit the transient spectra collected for each sample, resulting in an Evolution Associated Spectra (EAS). The number of EAS required to fit the spectra was estimated by inspection of the residuals.

5. **Target analysis**-The information from the EAS was used to test, with the Glotaran program, how various target models fit to studied mechanisms.[1] A detailed description of studied models will be presented with the discussion of the results in chapter 4 and chapter 5.

2.2.2.2 Time-Correlated Single Photon Counting

Experimental details: Fluorescence decays (with lifetimes between 350 ps and 20 ns) were measured using a home-built time correlated single photon counting (TCSPC) apparatus, using as excitation source a Horiba-JI-IBH NanoLED (λ_{ex} = 282 nm). Fluorescence decays with shorter lifetimes were investigated using a picosecond-TCSPC apparatus (λ_{ex} = 272 − 273 nm). The excitation source consisted of a picosecond Spectra Physics mode-lock Tsunami laser (Ti:sapphire) model 3950 (repetition rate of about 82 MHz, tuning range 700-1000 nm), pumped by a Millennia Pro-10s, frequency-doubled continuous wave (CW), diode-pumped, solid-state laser (λ_{em}= 532 nm). A harmonic generator model GWU-23PS (Spectra-Physics) was

used to produce the third harmonic from the Ti-sapphire laser exciting beam frequency output.

Emission at right angle geometry was collected through a double subtractive Oriel Cornerstone 260 monochromator and detected by a Hamamatsu microchannel plate photomultiplier (R3809U-50). Signal acquisition and data processing was performed employing a Becker & Hickl SPC-630 TCSPC module. The scheme of the TCSPC setup is presented on Figure 2.2.

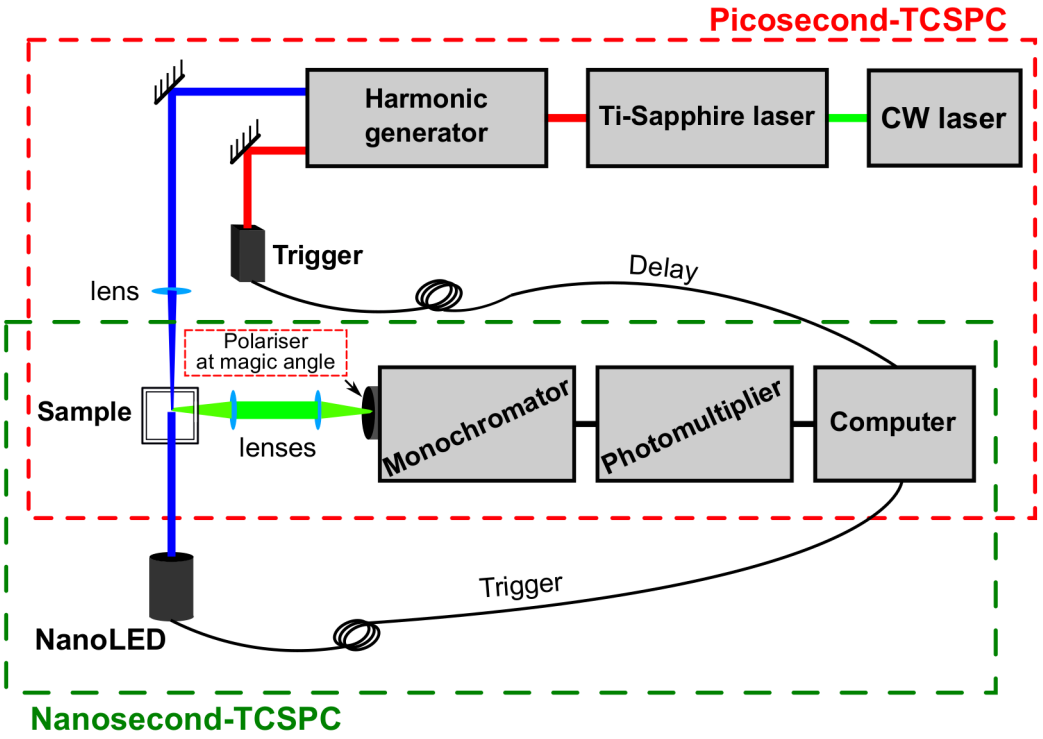

Figure 2.2 Schematic representation of the setup for the single photon counting measurement.

All the measurements were obtained in 5 or 10 mm quartz cuvettes. Samples were measured in the ambient atmosphere, except for sample solutions prepared for the bimolecular studies described in chapter 3, which were gently bubbled with solvent-saturated argon for 45 min prior to every experiment. Temperature control was achieved using a cryostat Optistat DN2 (188-308 K) or a cuvette holder FLASH 300 (253-328 K).

Data analysis: Deconvolution of the fluorescence decay curves was performed using the modulating function method, as implemented by G. Striker,[2] with automatic correction for the photomultiplier "wavelength shift", in the SAND program.

The biexponential data for intramolecular systems were analyzed using an adaptation of the Birks excimer mechanism. A detailed description is presented in chapter 4.

2.2.2.3 Flash Photolysis

Experimental details: The triplet-triplet absorption measurement setup consists of an Applied Photophysics laser flash photolysis apparatus pumped by the fourth harmonic (266 nm) of a Nd:YAG laser (Spectra Physics) and probed with a pulsed 150W Xe lamp. R928 photomultiplier from Hamamatsu is at a right angle to the excitation beam. The signal is collected by a Tektronix TDS 3052B oscilloscope and transferred to an IBM RISC computer. The optical density (OD) at different time delays and wavelengths is registered using the Applied Photophysics software. The scheme of the flash photolysis setup is presented on Figure 2.3.

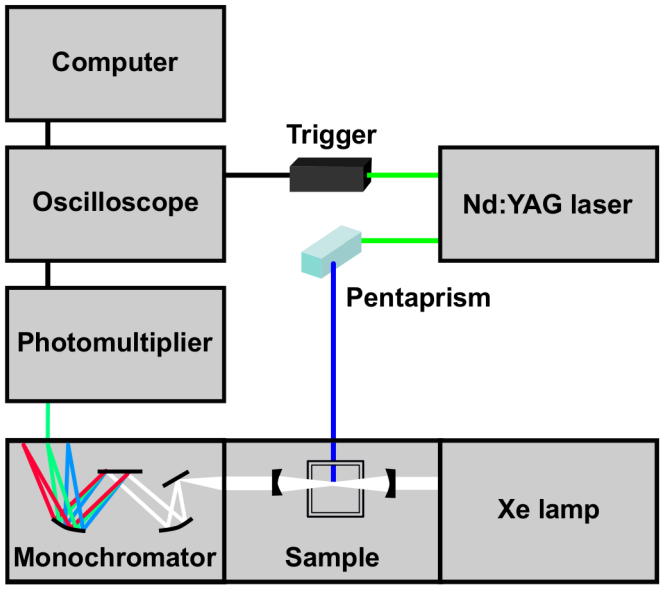

Figure 2.3 Schematic representation of the setup for the flash photolysis measurement.

The transient spectra were obtained by monitoring the optical density change at 5-10 nm intervals over the range 270-800 nm and averaging at least 3 decays at each wavelength. Samples for flash photolysis were measured in the presence of oxygen, and in an inert atmosphere (prior to experiment, samples were gently bubbled with nitrogen or argon for 20 min and sealed). To avoid multiphoton and triple-triplet annihilation effects low laser energy was used.

Data analysis: Exponential fitting was applied to the registered decays. The triplet molar absorption coefficient ε_T can be determined from the relationship:

$$\varepsilon_T = \frac{\varepsilon_S \times \Delta OD_T}{\triangle OD_S} \tag{2.1}$$

where ε_S is the singlet molar absorption coefficient, and ΔOD_S and ΔOD_T are obtained from the triplet-singlet difference transient absorption spectra.

The triplet quantum yield (Φ_T) values were calculated from:

$$\Phi_T^S = \Phi_T^{ref} \frac{\varepsilon_T^{ref}}{\varepsilon_T^S} \frac{\Delta OD^S}{\triangle OD^{ref}} \tag{2.2}$$

where the superscripts s and ref denote sample and reference. ε_T is the triplet molar absorption.[3]

2.2.3 Electronic Structure Calculations

The molecular structures and the energies of conformers of **1** were calculated with GAMESS[4] using the B3LYPV1R hybrid functional[5–8] and the 6-31G(d) Pople basis set for all atoms.[9] This level of theory has been widely used and is adequate for the description of the electronic transitions present in our systems.[10] Time-Dependent DFT (TDDFT) was used to optimize the excited states using the same functional. All singlet states were described using RHF formalism and the triplet state used UHF formalism. There was no relevant spin contamination on the UHF calculations, <S2>=2.022.

References

1. I. H. M. van Stokkum, D. S. Larsen and R. van Grondelle, *Biochim. Biophys. Acta- Bioenerg.*, 2004, **1657**, 82–104.

2. G. Striker, V. Subramaniam, C. A. M. Seidel and A. Volkmer, *J. Phys. Chem. B*, 1999, **103**, 8612–8617.

3. C. V. Kumar, L. Qin and P. K. Das, *J. Chem. Soc. Faraday Trans. 2*, 1984, **80**, 783–793.

4. M. W. Schmidt, K. K. Baldridge, J. A. Boatz, S. T. Elbert, M. S. Gordon, J. H. Jensen, S. Koseki, N. Matsunaga, K. A. Nguyen, S. Su, T. L. Windus, M. Dupuis and J. A. Montgomery, *J. Comput. Chem.*, 1993, **14**, 1347–1363.

5. A. D. Becke, *J. Chem. Phys.*, 1993, **98**, 5648–5652.

6. P. J. Stephens, F. J. Devlin, C. F. Chabalowski and M. J. Frisch, *J. Phys. Chem.*, 1995, **98**, 11623–11627.

7. F. J. Devlin, J. W. Finley, P. J. Stephens and M. J. Frisch, *J. Phys. Chem.*, 1995, **99**, 16883–16902.

8. R. H. Hertwig and W. Koch, *Chem. Phys. Lett.*, 1997, **268**, 345–351.

9. R. Ditchfield, W. J. Hehre and J. A. Pople, *J. Chem. Phys.*, 1971, **54**, 724–728.

10. S. S. Leang, F. Zahariev and M. S. Gordon, *J. Chem. Phys.*, 2012, **136**, 104101.

3 Dynamics of Radical Ion Pairs following Photoinduced Electron Transfer in Solvents with Low and Intermediate Polarities

In Section 1.1 the relevance of electron transfer in several fields was briefly presented. However, as shown in Sections 1.5.2.3-1.5.2.4, the experimental results obtained by various groups do not always follow the theoretical predictions of Marcus theory. Therefore, there exists a need to present a unified conceptual framework, which may help analyze electron transfer data obtained in very diverse systems, starting from bimolecular reactions in solution, through to surface reactions and also including ET reactions in proteins.

This chapter, focuses on the solvent- and temperature-dependencies of ET rates in bimolecular photoinduced electron transfer reactions. These studies are a continuation of the work performed previously in our research group,[1–3] where charge separation and charge recombination rates were analyzed using the nonadiabatic theories in comparison with the Intersecting-State Model (ISM). It was found that the ISM described more precisely the relationship between the experimental rate constants and their driving forces. This was especially observed in very exothermic reactions (ΔG^0=-70 kcal/mol), where charge recombination rates increased when the driving force increased, which can be tentatively assigned to the end of the

inverted region and the presence of a new "double inverted region". The ISM accounts for a possible increase of the reorganization energy with the driving force of the reaction, which is not included in nonadiabatic theories. Additionally, previous studies indicated that the polarity of the solvent does not influence ET rate in the way predicted by Marcus.[1–3]

Here, the bimolecular studies are conduced between well known aromatic hydrocarbons and fumaronitrile acting as electron donors and electron acceptor, respectively, in solvents with low or middle polarities. The structures of the molecules investigated are presented in Figure 3.1, together with their redox potentials.

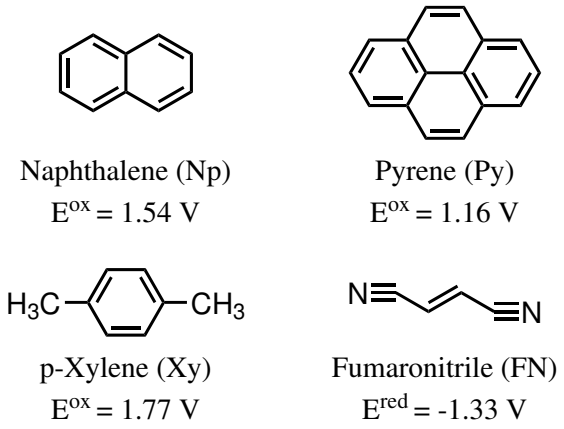

Figure 3.1 Structures of the studied molecules.

Fumaronitrile was chosen as the acceptor, due to its ability to form emissive charge transfer state/exciplex in the aromatic hydrocarbons/fumaronitrile systems, which was shown by earlier studies.[4–6] The presence of the emissive species allows for its better characterization.

Collected experimental data of charge recombinations for very exothermic reactions are compared with the ISM, and presented in the article entitled: **"Dynamics of Radical Ion Pairs following Photoinduced Electron Transfer in Solvents with Low and Intermediate Polarities**", published in *"Journal of Physical Chemistry B"* in 2015.[7] The findings from this study are discussed below. Fluorescence decays obtained by single photon counting are presented in Appendix B. ΔG^0_{LIP} in eq. 3.1 correspond to the eq. 1.16 presented in the chapter 1.

3.1 Introduction

The nature of radical ion pairs formed by photoinduced electron transfer (ET) from an electron donor (D) to an acceptor (A) has been subject to intense scrutiny for decades,[8–19] in view of their fundamental interest in biological and artificial solar energy conversion, and in the design of molecular level devices. The current view is that ET occurs over a range of donor-acceptor distances, r_c, and may originate contact radical ion pairs (CIP, or charge-transfer exciplexes), loose ion pairs (LIP, or solvent-separated ion pairs) or free ions in solution. These species can be distinguished by the values of r_c, which are $3<r_c<4$ Å for CIP, $6.5<r_c<8.8$ Å for LIP or $r_c>10$ Å for free ions.[9,13,20,21] The nature of such radical ion pairs determines their thermodynamics and kinetics, which ultimately control the efficiencies of charge separation, ion formation and isolated products.

A wide distribution of donor-acceptor distances may be observed in ion pairs when the ET rates are weakly dependent on r_c. Such rates decrease exponentially with r_c, $k_{ET} = k_0 exp\left[-\beta\left(r_c - r_0\right)\right]$, where β is the distance decay factor, r_0 is the donor-acceptor contact distance and k_0 is the ET rate in contact. ET rates in frozen toluene glass yielded β=1.23 Å^{-1}, and aqueous acid glasses gave β=1.59 Å^{-1},[22] similar to β=1.63 Å^{-1} observed for glycerol:methanol 9:1 mixtures at –18 °C.[3] The decay factors for ET across covalently linked donor-acceptor systems are typically smaller, $\beta<1.1$ Å^{-1}.[22] Solvent molecules can mediate ET to an extent comparable to that of covalent pathways between the donor and the acceptor, and values of $\beta\approx1$ Å^{-1} are frequently employed in liquid solutions.[23–31] ET across one single solvent molecule in U- and C-shaped donor-acceptor systems, that allow for one solvent molecule at a time on the "line of sight" between the donor and acceptor groups,[32,33] gave β values ranging from 0.64 to 0.97 Å^{-1}.[34] The value of β will ultimately depend on the alignment and energy of the active orbitals of donor, solvent and acceptor, but the available evidence is that β is sufficiently small to allow for competitive bimolecular photoinduced charge separations (PCS) leading directly to CIP or LIP. Figure 3.2 illustrates the competitive PCS channels leading to CIP (k_{qc}) or to LIP (k_{ql}), the

initial solvation of the CIP (k_s), the collapse of the LIP in a CIP (k_{-s}) or its separation in free ions (k_{sep}), and the charge recombinations in CIP (k_{CIP}) and LIP (k_{LIP}).

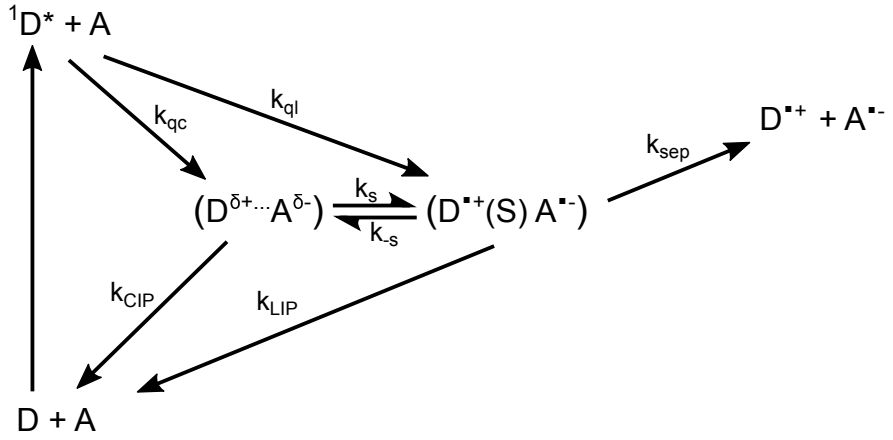

Figure 3.2 Species involved in photoinduced electron transfer reactions and mechanism of their conversions. Adapted from reference[7].

ET reactions exhibit peculiar free-energy dependence. The rates of weakly exothermic bimolecular PCS increase with the exothermicity of the reactions, become controlled by diffusion when $\Delta G^0 \approx -10$ kcal/mol, and remain controlled by diffusion to at least $\Delta G^0 = -60$ kcal/mol.[8] This behavior contrasts with the decrease of ET rates with the reaction energy observed for very exothermic ET between rigidly held D and A, known as the Marcus inverted region.[1,12,35–37] This difference is particularly striking when comparing bimolecular PCS with first-order charge recombinations in radical ion pairs of the same molecular species in the same solvent, and stimulated the formulation of various theoretical models and systematic experimental testing.[12,14,31,38–40] The most frequently invoked explanation for the absence of inverted regions in bimolecular PCS is that, as the reactions become more exothermic, the transfer of the electron occurs at increasingly larger donor-acceptor separations.[38,41] In fact, following the two-spheres dielectric continuum model,[42] solvent reorganization energies (λ_s) increase for large donor-acceptor separations, and may displace the onset of the inverted region to lower ΔG^0, at the cost of reducing the electronic coupling for the transfer. A formulation of this hypothesis suggested

that r_c may reach 12 Å at ΔG^0= –60 kcal/mol.[43]

Recent studies of time-resolved magnetic field effects[18] and ultrafast time-resolved absorption and infrared spectroscopies[19,44] showed that the hypothesis of bimolecular PCS leading directly to free ions (r_c>10 Å) is inconsistent with compelling evidence for competitive direct formation of CIP and LIP even in polar solvents such as acetonitrile. The relative rates depend on the polarity of the solvent, with $k_{qc}>k_{ql}$ for $\varepsilon<16$,[17] and are related with the free-energies of these reactions. The change in thermodynamic preference from a CIP to a LIP with an increase in the polarity of solvents at room temperature was described by Weller in terms of the semi-empirical relations, in eV,[9]

$$\begin{aligned}\Delta G^0_{exc} &= E^{ox}_D - E^{red}_A - \frac{\mu^2}{\rho^3}\left[f(\varepsilon) - f(n_D)\right] - E^* + 0.15 + T\Delta S^0 \\ \Delta G^0_{LIP} &= E^{ox}_D - E^{red}_A + \frac{e_0^2}{\varepsilon}\left(\frac{1}{r} - \frac{1}{r_c}\right) - E^* - \frac{0.39}{r}\end{aligned} \tag{3.1}$$

where E^{ox}_D and E^{red}_A are the oxidation and reduction potentials of donor and acceptor, E^* is the excited state energy of D^*, r is the average radius of the reactants, μ^2/ρ^3= 0.75 eV and ΔS^0= 0.777 meV for a typical exciplex,[9] and e_0^2=$e^2N_A/4\pi\varepsilon_0$. Exciplex (or CIP) formation is typically accompanied by the observation of a broad and structureless emission, red-shifted relative to the emission of the molecular components of the exciplex. LIPs have much lower electronic couplings and, consequently, much weaker emissions. CIPs and LIPs can be distinguished on the basis of the dependence of their emission maxima on the polarity of the solvent, expressed by the Lippert-Mataga equation[45,46]

$$\begin{aligned}\bar{\nu}_{ex} &= \bar{\nu}_{ex}(0) - \frac{2}{hc}\frac{\mu^2}{\rho^3}\left[f(\varepsilon) - \frac{1}{2}f(n_D)\right] \\ f(\varepsilon) &= \frac{\varepsilon - 1}{2\varepsilon + 1};\ f(n_D) = \frac{n_D^2 - 1}{2n_D^2 + 1}\end{aligned} \tag{3.2}$$

where μ is the dipole moment of the fluorescence state and ρ the effective radius of the solvent cavity in which the ion pair fits. Usually a series of solvents with different dielectric constants ε and refractive indexes n_D is employed to obtain the

dipole moment of the emissive species from the slope of eq. 3.2. Alternatively, the temperature dependence of the fluorescence maxima in one single solvent can be plotted as a function of $f(\varepsilon) - 1/2 f(n_D)$ making use of the temperature dependencies of ε and n_D. For example, in methyl acetate ε increases from 6.7 at 35 °C to 7.4 at 0 °C.[47]

We have shown that the exciplexes formed between p-xylene (Xy), naphthalene (Np) or pyrene (Py) and fumaronitrile (FN) in weakly polar solvents should also be regarded as CIPs.[1] Their low fluorescence quantum yields reflect the small radiative rate constants and are typical of systems with high dipole moments.[48] In this work we show that photoinduced ET directly forms CIPs in weakly polar solvents with rates close to diffusion and that the monoexponential decays observed are associated with CIP lifetimes. In such solvents the formation of LIPs is endothermic and this excludes ET at distance as the mechanism to bypass the inverted region in weakly polar solvents. We also show that the temperature dependence of the methyl acetate dielectric constant leads to thermochromism of exciplex emission and a strong decrease of the exciplex emission at lower temperatures.

3.2 Results and Discussion

3.2.1 Steady-State Fluorescence

Figure 3.3 shows the steady-state fluorescence spectra of Np/FN in various solvents. Similar data was obtained for the Py/FN and Xy/FN systems. The emission of the CT state in all the systems presents a bathochromic shift with the increase of the solvent polarity, whereas the monomer emission remains unchanged. For example, the Py/FN emission maximum is displaced from 452 nm in cyclohexane, to 532 nm in isopropyl ether, and to 616 nm in 1,2-dichloroethane. Arguably, the fluorescence maxima of the broad and weak fluorescence bands observed for higher polarity solvents may depend on the correction factors employed to account for the wavelength sensitivity of the fluorescence detector.[49] However, we observed similar solvent dependencies for systems (Py, Np or Xy as donors and FN as acceptor) that fluoresce at quite distinct wavelengths and necessarily have distinct correction factors. The strong solvatochromism observed for these systems is typical of polar exciplexes and has been employed to characterize the degree of charge separation.[50–52]

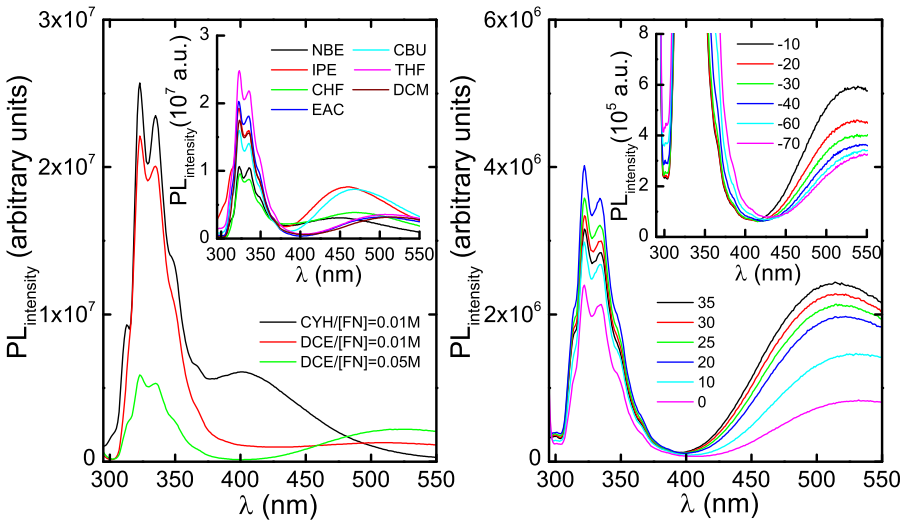

Figure 3.3 Left: Fluorescence of Np/FN in cyclohexane (black line) and in 1,2-dichloroethane (red line) at 20^{o}C for [FN] = 0.01 M, and for [FN] = 0.05 M in 1,2-dichloroethane (green line) in order to make visible the fluorescence from the CT state. The inset illustrates fluorescence in various solvents. Right: Fluorescence of Np/FN in methyl acetate at the temperatures indicated in the plot, using [FN]=0.05 M. Adapted from reference[7].

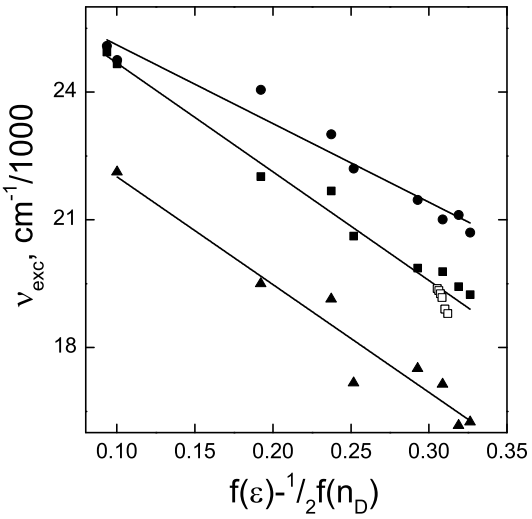

Figure 3.4 Lippert-Mataga plots expressing the dependence of CT band emission maximum on the solvent polarity function, for Xy/FN (circles), Np/FN (squares) and Py/FN (triangles) at room temperature and for Np/FN in methyl acetate from 35 to 0 °C (open squares). Adapted from reference [7].

The solvatochromic behavior of the CT emission can be conveniently interpreted in the framework of eq. 3.2, as shown in Figure 3.4. According to eq. 3.2, the slopes of the lines presented in Figure 3.4 are related to the dipole moments and to the effective radii of the emissive species. The effective radii can be calculated with molecular models and compared with independent data. The effective radius, ρ, can be estimated as the radius of the equivalent sphere inaccessible to the solvent given by a Connolly surface.[53] The structures of the molecules that originate the emissive species were optimized using the AM1 method, and the volumes of donor, acceptor and solvent (e.g., isopropyl ether and methyl acetate) were calculated using a point probe. The calculated equivalent radii are 3.4 Å for isopropyl ether and 2.7 Å for methyl acetate. The contact re-entrant volume of the emissive species was then calculated with these solvent molecule probes. The lower limit for the equivalent cavity radius of Np/FN in isopropyl ether is ρ>4.5 Å and in methyl acetate we obtained ρ>4 Å, in good agreement with the 5 Å value typically used for exciplexes.[50] X-ray data on ion-radical associates of similar species revealed that they lie coplanar with interplanar π-separations r_c≈3.1±0.3 Å.[54,55] A full charge separation across a

3.1±0.3 Å distance corresponds to μ= 15±1.5 D. Assuming that this dipole moment is applicable to the emissive species and that the effective radius is ρ= 4.5 Å, we calculate a slope of 24,700 cm^{-1} for the Lippert-Mataga. The experimental slopes range from 18,500 cm^{-1} for Xy/FN to 25,300 cm^{-1} for Py/FN. Thus, the emissive species can be appropriately described as a CIP between an aromatic hydrocarbon radical cation and FN^{-}.

The nature of the emissive species seems to be the same in all these conditions, although eq. 3.1 with r= 3 Å and r_c= 6.5 Å predicts that the free energy of LIPs decreases below that of CIPs when $f(\varepsilon) - {}^1/_2 f(n_D)$>0.3, or ε>7, at room temperature. With our solvent probes, the value of the cavity radius calculated with Connolly surfaces is not very sensitive to the donor-acceptor distance: using r_c= 7 Å we obtained 5.15≤ρ≤5.33 Å. A full charge separation in a LIP with r_c= 7.0 Å, gives μ= 33.6 D. This dipole moment and ρ= 5.33 Å should lead to a slope of 75,000 cm^{-1} in a Lippert-Mataga plot, much higher than the slope calculated for CIPs. The assignment of the CT emission exclusively to a CIP with significant feedback from the corresponding LIP in solvents of intermediate polarity is consistent with other assignments in the literature.[21]

Using E^*= 4.51 eV and E_D^{ox}= 1.77 eV for p-xylene, E^*= 3.99 eV and E_D^{ox}= 1.54 eV for naphthalene, E^*=3.337 eV and E_D^{ox}= 1.16 eV for pyrene, E_A^{red}= –1.33 eV for fumaronitrile,[56,57] the literature values for the dielectric constants and refractive indexes of the solvents,[47,58] and r = 3 Å and r_c= 6.5 Å, we estimate exothermic and irreversible PCS for all the systems studied in this work. This is depicted in Figure 3.2 in terms of the lower energies of the CIP and LIP states with respect to the locally excited (monomer) state. The formation of free ions ($r_c = \infty$) in our systems is endothermic with respect to the free energy of the corresponding LIP. This simplifies the kinetic scheme, because the predominant decay pathways of the CIP and LIP must be the decay to the reactants ground state.

Figure 3.3 also shows the temperature dependence of the CT emission in methyl acetate. This emission presents an interesting thermochromism, with a displacement

of the emission maximum of the Np/FN CT fluorescence from 514 nm at 35 °C to 532 nm at 0 °C and then to 547 nm at –70 °C. Interestingly, this bathochromic shift is more accentuated than expected from the temperature dependence of the dielectric constant of methyl acetate, that increases from 6.7 at 35 °C to 7.4 at 0 °C.[47] The values reported for the temperature dependence of the dielectric constant of methyl acetate, $d\varepsilon/dT$, range between 0.02 and 0.03 for this range of temperatures and are not reliable known at lower temperatures.[47,59] This limits the significance of the increased slope observed for the thermochromism presented in Figure 3.4. Nevertheless, the bathochromic shift of the CT emission band is accompanied by a strong decrease in intensity of this band. The emission intensity in methyl acetate decreases by a factor of 2.9 from 35 °C to 0 °C, and by a factor of 7.5 from 35 °C to –70 °C.

The decrease in emission intensity with an increase in ε can be analyzed in terms of a CT emission coming from equilibrated CIP and LIP species. The equilibrium constant $K_{eq} = exp\left[-\left(\Delta G^0_{exp} - \Delta G^0_{LIP}\right)/RT\right]$ increases from 0.3 to 0.4 from 35 °C to 0 °C, which favors the population of LIP species. However, this shift in the equilibrium position is insufficient to account for the decrease of the CIP emission by a factor of 2.9 in this temperature range. It is unlikely that the radiative rate of the CIP appreciably changes in this temperature range. Alternatively, at lower temperatures, the slower diffusion may reduce the monomer quenching efficiency and, consequently, diminish the CT emission intensity. Indeed, at temperatures below –20 °C there is a systematic increase in the monomer emission intensity with the lowering of the temperature, which may indicate that a smaller fraction of monomer is quenched. However, in the 35 °C to 0 °C temperature range the most likely explanation for the strong and systematic decrease of the CT emission is that CIP and LIP are not equilibrated, i.e., the rates of their decays (k_{CIP}, k_{LIP}) are competitive with the rates of their interconversion (k_s, k_{-s}). Vauthey and co-workers recently showed that photoinduced ET from 9-cyanoanthracene to phthalic anhydride in tetrahydrofuran ($\varepsilon = 7.58$) leads to CIP and LIP with $k_s = 2.2\times10^9\ s^{-1}$ and $k_{-s} = 2.0\times10^9\ s^{-1}$,

and a decay rate constant k_{CIP}= 1.6×10^9 s^{-1}.[19] The similarity between these rate constants does not allow for the establishment of a pre-equilibrium between CIP and LIP before decays.

3.2.2 Kinetics and Quantum Yields

Figure 3.2 shows two alternative channels to produce CIP: direct formation of the CIP by electron transfer in contact between donor and acceptor, or long-distance PCS to form a LIP followed by collapse to the CIP. We investigated these two alternative mechanisms in weakly polar solvents measuring the temperature dependence of the PCS rates. The decay of the monomer emission in the presence of fumaronitrile and the rise time of exciplex fluorescence were measured at different temperatures in n-heptane, using a TCSPC method previously described for similar reactions in isopropyl ether.[2] Figure 3.5 illustrates an Arrhenius plot of the rate constants in n-heptane, together with the diffusion rates calculated with the Stokes-Einstein equation and the temperature-dependence of the solvent viscosity.[58] Second-order charge-separation rates in the Py/FN system in n-heptane are controlled by diffusion at all the temperatures represented in the plot and can be described by an activation energy E_a= 2.7 kcal/mol. This activation energy is incompatible with the existence of LIPs as intermediates in the ET reactions because the formation of Py/FN LIPs is endothermic by 8.5 kcal/mol at room temperature. LIPs cannot be intermediates in the diffusion-controlled PCS in n-heptane.

Global analysis of Np/FN emission decays in methyl acetate, dichloromethane and 1,2-dichloroethane gave adequate monoexponential fits for the decay of the monomer emission, which corresponded to the rise time of the CT emission, and only one exponential decay was required to fit the CT emission decay. Nevertheless, the quality of the fit is slightly eroded at lower temperatures, which indicates that the first-order approximation for the kinetics of the CT emission may breakdown in more polar solvents. The Appendix B shows that the first-order fit to the CT emission in methyl acetate at room temperature has χ^2= 1.32 and that χ^2 increases

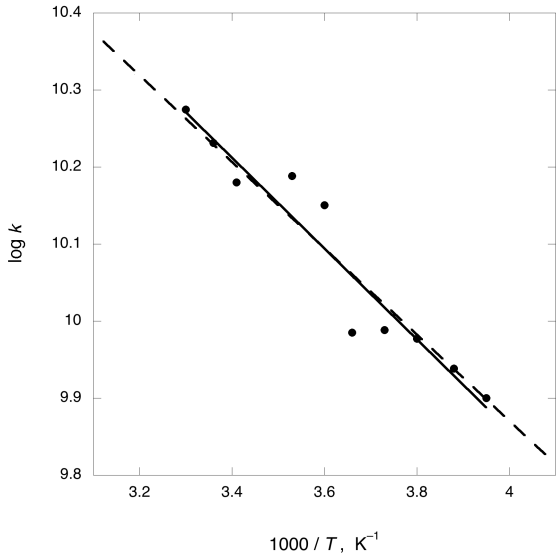

Figure 3.5 Arrhenius plots for the experimental data on PET in Py/FN (best fit in full line) and for diffusion rate constants given by the application of the Stokes-Einstein equation to n-heptane (dashed line). Adapted from reference [7].

to 2.11 at –30 °C. The emission originating from the CIP in these conditions may have a significant feedback from the LIP and should be nonexponential, as observed for tetracyanobenzene/alkylbenzene CIP decays in 1,2-dichloroethane.[21] However, as will be shown below, at the free energies of the Np/FN CIP or LIP charge recombinations in these solvents, the rates of these charge recombinations are expected to be very similar and may lead to decays that can be fitted with a single exponential. Table 3.1 presents the rate constants calculated as the reciprocal of the CT emission decays.

Table 3.1 Rates of Figure 3.2, in units of $10^7\,s^{-1}$, for the naphthalene/fumaronitrile system.

Solvent	T/°C	ε	$1/\tau_{CIP}$	$1/\tau_{LIP}$	k_{SEP}
	20	6.9	6.8		
Methyl acetate	-15	≈ 7.7	18		
	-30		19		
CH_2Cl_2	20	8.93	9.5	1.9-2.9[a]	0.28[a]
$C_2H_4Cl_2$	20	10.36	16	14-22[a]	0.77[a]

[a] From transient absorption measurements.

The formation of free ions from the LIP in dichloromethane and 1,2-dichloroethane is endothermic by 6.7 and 5.7 kcal/mol, respectively. Given the nanosecond lifetimes measured by TCSPC for these systems, the separation of the ions should be a minor decay pathway. We measured the rise time and quantum yield of the naphthalene$^{\bullet+}$ free ion by flash photolysis to obtain additional information on the decay pathway leading to free ions.

The molar extinction coefficient of the naphthalene cation $\left(\varepsilon_{Np^+}\right)$ in solution remains associated with a large uncertainty.[60] At room temperature, values between 5300 $M^{-1}cm^{-1}$ [61] and 2970 $M^{-1}cm^{-1}$ [62] have been reported. We measured this quantity by secondary electron transfer in a 0.15 M naphthalene and 1×10^{-1} M dicyanobenzene (Np/DCB) acetonitrile solution in the presence of aniline 5×10^{-4} M, which is recognized as a radical scavenger with a high and known molar extinction coefficient ($\varepsilon_{Ani^+} = 12050\ M^{-1}cm^{-1}$ at 385 nm in aniline).[63] The secondary electron transfer to the scavenger is exothermic by at least 9 kcal/mol, and thus is diffusion controlled and quantitative.[64] In these conditions, the scavenger is a good monitor of the naphthalene cation. The value of ε_{Np^+} is related to the ratio of transient absorption of the naphthalene cation and the monitor cation, $\varepsilon_{Np+} = \left(\Delta A_{Ani^+}/\Delta A_{Np^+}\right)\varepsilon_{Ani^+}$. Assuming a unit quantum yield for the secondary electron transfer and using the transient absorptions of the naphthalene cation in the Np/DCB system and of the aniline cation in the Np/DCB/Ani system, we obtained $\varepsilon_{Np^+} = 3400\ M^{-1}cm^{-1}$ at 685 nm for the naphthalene cation in acetonitrile.

The transient absorption of Np$^{\bullet+}$ in dichloromethane is shown in Figure 3.6. It has a broad absorption band with a maximum at 685 nm and is expected to be similar for CIP, LIP or free ions. Mataga and co-workers[65] have shown that the transient absorptions of such species have approximately the same spectra and extinction coefficients, and can only be distinguished by their kinetics. Thus, we must rely on lifetimes to ascribe the Np$^{\bullet+}$ transient spectra to any of these forms in dichloromethane or in 1,2-dichloroethane. We measured nanosecond rise times for Np$^{\bullet+}$ in dichloromethane and in 1,2-dichloroethane (357 ns and 130 ns, respec-

tively) and microsecond decays (4 μs and 2 μs, respectively). The decays are typical of free ions in solution. According to scheme (Figure 3.2), the reciprocal of the rise times give the rate constants for the separation of the ions, k_{sep}= 2.8×10^6 and 7.7×10^6 s^{-1} in dichloromethane and in 1,2-dichloroethane, respectively, which are consistent with the endothermicities in these solvents and a collision frequency of 10^{11} M^{-1}s^{-1}. This suggests a sequential mechanism $\left(^1D^* + A\right) \rightarrow \left(D^{\delta+}A^{\delta-}\right) \rightarrow \left(D^{\bullet+}\,(S)\,A^{\bullet-}\right) \rightarrow D^{\bullet+} + A^{\bullet-}$ in these more polar solvents. The naphthalene triplet was not detected in our experiments with Np/FN in chlorinated solvents, consistent with results obtained with low polarity solvents.[11]

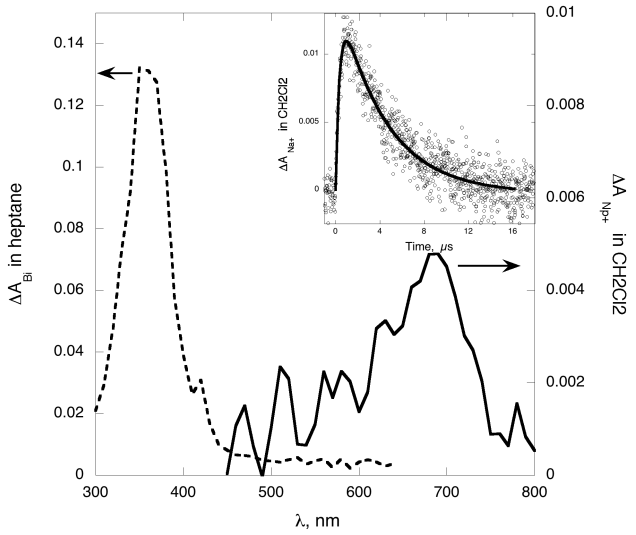

Figure 3.6 Transient absorption spectra of naphthalene radical cation Np$^{\bullet+}$ (full line) and biphenyl triplet (dashed line) in dichloromethane. Inset: rise time and decay of Np$^{\bullet+}$ transient absorption. Adapted from reference[7].

The free ion quantum yields of Np$^{\bullet+}$ in dichloromethane or in 1,2-dichloroethane can be obtained from the intensities of the transient absorptivities of Np$^{\bullet+}$ in the Np/FN system $\left(\Delta A_{Np^+}\right)$ and of the biphenyl triplet (ΔA_{Bi}, Φ_T = 0.84, ε_T^{Bi}= 2.71×10^4 M^{-1}cm^{-1}) in a reference solution, given $\Phi_{sep} = \Phi_T \left(\Delta A_{Np^+}/\varepsilon_{Np^+}\right) / \left(\Delta A_{Bi}/\varepsilon_T^{Bi}\right)$. Using the values of Delcourt and Rossi or our own values for ε_{Np^+}, we obtain Φ_{sep}= 0.094 or 0.147 in dichloromethane and Φ_{sep}= 0.035 or 0.053 in 1,2-dichloroethane, respectively. These quantum yields with the corresponding k_{sep} and the definition of the free-ion quantum yield ($\tau = \Phi_{sep}/k_{sep}$), give the precursor life-

times $\tau = 35$ or 52 ns in dichloromethane and $\tau = 4.5$ or 6.9 ns in 1,2-dichloroethane, depending on the value selected for ε_{Np^+}. The precursors of the free ions are the LIP and the corresponding decay rate constants are presented in Table 3.1.

The CIP charge recombination rates obtained in this work are consistent with those of analogous systems,[1,2,21,66,67] and confirm the absence of significant medium effects in such reactions.[1,68] The charge recombination assigned for the LIP in 1,2-dichloroethane fits in the free-energy dependence of other LIP charge recombinations measured in this solvent,[21] as illustrated in Figure 3.7. The charge recombination free energies of the Np/FN CIP and LIP are in the –69 to –72 kcal/mol range and the corresponding rate constants are expected to fall 0.5-2$\times 10^8\,s^{-1}$ range, as observed. All the free energies illustrated in this plot were re-calculated with eq. 3.1 using consistent values for the redox potentials.[56] The lines represent calculations with the Intersecting-State Model,[39] and have been published before.[1,2]

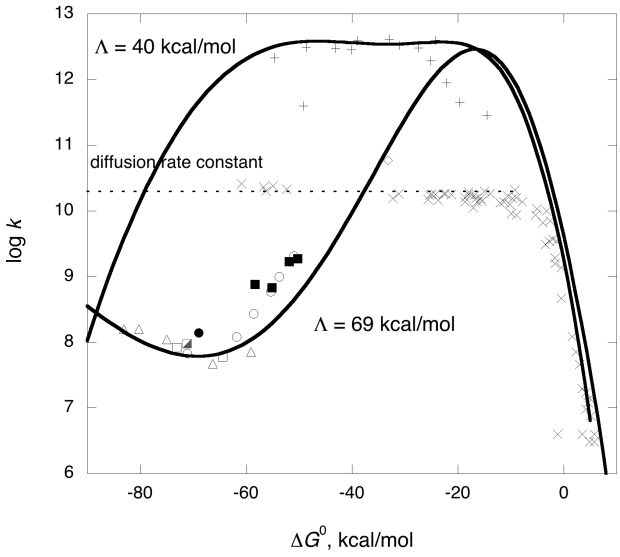

Figure 3.7 Free energy relationships of charge recombinations in CIP formed in weakly polar solvents (open symbols) and in LIP formed in 1,2-dichloroethane (■),[21] and of bimolecular PCS in acetonitrile (×[8] and +[69]). Aromatic hydrocarbons and FN in heptane (△),[1] isopropyl ether (□)[2] and methyl acetate (○), hexamethylbenzene and tetracyanoethylene in cyclohexane (lozenge);[67] circles also represent alkylbenzenes and tetracyanobenzene in chloroform.[70] The half-filled square represents naphthalene and FN in dichloromethane. The full lines represent calculations with the Intersecting-State Model using the values of the fitted parameter Λ presented in the plot that have been published elsewhere. Adapted from reference[7].

Figure 3.7 also compares the charge recombinations rates in CIP with those of bimolecular PCS originally obtained by Rehm and Weller [8] and the more recent data reported by Vauthey and co-workers beyond the diffusion limit of acetonitrile. [69] The striking difference between the free-energy relationships of these closely related ETs, and the difficulty to observe the Marcus inverted region in PCS, has been explained by ET at increasingly larger donor-acceptor separations as the reactions become more exothermic, with the consequent increase in the solvent reorganization energy. [38] This and other recent work show that bimolecular PCS forms CIPs competitively with LIPs, [15,18] which implies that the solvent reorganization energy cannot increase appreciable with the donor-acceptor distance and compensate the exponential decay of the ET rate with that distance. Figure 3.7 presents calculations with the Intersecting-State Model, that rationalize the difference between charge recombinations and PCS in terms of a parameter Λ related to the dissipation of the reaction energy by accepting modes. [1,39] These calculations have been presented and discussed elsewhere. [3] In the framework of this alternative model, the increase in the reorganization energy is related with the driving force of the reaction rather than with the donor-acceptor distance, and the value of the parameter Λ is associated with the availability of good energy-accepting modes such as the low-frequency donor-acceptor stretch present in exciplexes.

3.2.3 Conclusions

The slopes of the Lippert-Mataga plots of exciplexes formed between fumaronitrile and electronically excited p-xylene, naphthalene or pyrene in various solvents at room temperature are consistent with nearly complete charge separations in contact ion pairs. The kinetics of photoinduced charge separations from electronically excited aromatic hydrocarbons to fumaronitrile in weakly polar solvents are indicative of the sequential mechanism: $\left(^1D^* + A\right) \rightarrow \left(D^{\delta+}A^{\delta-}\right) \rightarrow \left(D^{\bullet+}\left(S\right)A^{\bullet-}\right) \rightarrow D^{\bullet+} + A^{\bullet-}$. This work adds to the accumulating evidence that bimolecular PCS between donor and acceptor can directly produce both contact and loose ion pairs.

Exciplex emission in methyl acetate is strongly thermochromic. Thermochromic Lippert-Mataga plots have been reported before for covalently linked donor-acceptor systems,[71] but the extent of the exciplex thermochromism is remarkable because it is even more pronounced than the solvatochromism of the same exciplex. Interestingly, the thermochromism is accompanied by a strong decrease in emission intensity. This suggests that the decays of the CIP and/or LIP are competitive with the establishment of equilibrium between these two species.

CIPs and LIPs formed between aromatic hydrocarbons and nitriles decay predominantly by very exothermic charge recombinations in weakly and moderately polar solvents (ε<11), where the dissociation into free ions is substantially endothermic (ΔG^0>4 kcal/mol) and inefficient (Φ_{sep}<0.2). The charge recombination rates seem to be relatively independent of the nature of the solvent and for ultra-exothermic reactions (ΔG^0<–60 kcal/mol) they are also weakly dependent on the driving force of the reaction.

The downwards revision of the solvent reorganization energies with the more accurate models of Newton[55] and others,[72] poses an interesting challenge to ET theories because the revised values are a factor of two lower for polar solvents than those given by the Marcus two-sphere dielectric continuum model.[42] Moreover, the hypothesis that bimolecular PCS occur at long distance and have such large solvent reorganization that the onset of the Marcus inverted region is displaced to exothermicities ΔG^0<–60 kcal/mol, is not supported by dynamics of contact and loose ion pair formation. The rates of very exothermic bimolecular PCS offer at the best a tenuous evidence for the Marcus inverted region, in contrast with ET in rigid systems first shown by Miller to have pronounced inverted regions.[73] It is perhaps unexpected that full the theoretical description of electron transfer reactions, one of the most fundamental processes in Chemistry, did not yet reach closure.

3.3 Summary and Future Direction

This chapter focused on the bimolecular photoinduced electron transfer reaction in systems containing aromatic hydrocarbons and fumaronitrile as electron donors and electron acceptor, respectively. The choice of the chromophores allowed the investigation of the charge recombinations rates for very exothermic reactions. The rates with moderate exothermicities lie in the inverted region. However, further increase of the driving forces, above -70 kcal/mol, led to the increase of the CR rate. The CR data obtained from this work and the references values taken from the literature were well described using ISM. The charge recombination rate was not dependent on the polarity of the solvent in the way predicted by Marcus theory. These results are consistent with previously published data.[1–3]

It was shown that photoexcitation of the donor led to the formation of a contact ion pair/ exciplex rather than direct formation of the free ions. Studying the bimolecular ET did not allow for probing the charge separation rates, which are diffusion-limited.

In order to overcome the diffusion of charges and be able to probe the charge separation rates close to the optimal region, it is necessary to study first order reactions by using covalently linked donor-acceptor systems. Additionally, molecules for these types of intramolecular studies, can be designed to reduce unknown variables influencing the ET such as the distance, orientation, electronic coupling etc.. This approach should allow for the exploration of free-energy dependence for even more exothermic ET reactions and, thus, the dependence of the CR rate on the driving forces of the reactions.

References

1. C. Serpa, P. J. S. Gomes, L. G. Arnaut, S. J. Formosinho, J. Pina and J. S. De Melo, *Chem. - A Eur. J.*, 2006, **12**, 5014–5023.

2. C. Serpa, P. J. S. Gomes, L. G. Arnaut, J. S. De Melo and S. J. Formosinho, *Chemphyschem*, 2006, **7**, 2533–2539.

3. P. J. S. Gomes, C. Serpa, R. M. D. Nunes, L. G. Arnaut and S. J. Formosinho, *J. Phys. Chem. A*, 2010, **114**, 2778–2787.

4. D. Creed, P. H. Wine, R. A. Caldwell and L. A. Melton, *J. Am. Chem. Soc.*, 1976, **98**, 621–623.

5. R. A. Caldwell and D. Creed, *J. Am. Chem. Soc.*, 1979, **101**, 6960–6965.

6. F. D. Lewis and J. T. Simpson, *J. Phys. Chem.*, 1979, **83**, 2015–2019.

7. K. K. Mentel, R. M. D. Nunes, C. Serpa and L. G. Arnaut, *J. Phys. Chem. B*, 2015, **119**, 7571–7578.

8. D. Rehm and A. Weller, *Isr. J. Chem.*, 1970, **8**, 259–271.

9. A. Weller, *Zeitschrift für Phys. Chemie*, 1982, **133**, 93–98.

10. I. R. Gould, R. H. Young, R. E. Moody and S. Farid, *J. Phys. Chem.*, 1991, **95**, 2068–2080.

11. C. Serpa and L. G. Arnaut, *J. Phys. Chem. A*, 2000, **104**, 11075–11086.

12. N. Mataga, H. Chosrowjan and S. Taniguchi, *J. Photochem. Photobiol. C Photochem. Rev.*, 2005, **6**, 37–79.

13. E. Vauthey, *J. Photochem. Photobiol. A Chem.*, 2006, **179**, 1–12.

14. M. G. Kuzmin, I. V. Soboleva and E. V. Dolotova, *J. Phys. Chem. A*, 2007, **111**, 206–215.

15. D. R. Kattnig, A. Rosspeintner and G. Grampp, *Angew. Chemie - Int. Ed.*, 2008, **47**, 960–962.

16. O. F. Mohammed, K. Adamczyk, N. Banerji, J. Dreyer, B. Lang, E. T. J. Nibbering and E. Vauthey, *Angew. Chemie, Int. Ed.*, 2008, **47**, 9044–9048.

17. S. Richert, A. Rosspeintner, S. Landgraf, G. Grampp, E. Vauthey, D. R. Kattnig, G. Grampp, E. Vauthey and D. R. Kattnig, *J. Am. Chem. Soc.*, 2013, **135**, 15144–15152.

18. H. M. Hoang, T. B. V. Pham, G. Grampp and D. R. Kattnig, *J. Phys. Chem. Lett.*, 2014, **5**, 3188–3194.

19. M. Koch, R. Letrun and E. Vauthey, *J. Am. Chem. Soc.*, 2014, **136**, 4066–4074.

20. T. Kakitani, A. Yoshimori and N. Mataga, *J. Phys. Chem.*, 1992, **96**, 5385–5392.

21. B. R. Arnold, D. Noukakis, S. Farid, J. L. Goodman and I. R. Gould, *J. Am. Chem. Soc.*, 1995, **117**, 4399–4400.

22. O. S. Wenger, *Science*, 2005, **307**, 99–102.

23. S. Murata, S. Y. Matsuzaki and M. Tachiya, *J. Phys. Chem.*, 1995, **99**, 5354–5358.

24. S. Murata and M. Tachiya, *J. Phys. Chem.*, 1996, **100**, 4064–4070.

25. S. F. Swallen, K. Weidemaier, H. L. Tavernier and M. D. Fayer, *J. Phys. Chem.*, 1996, **100**, 8106–8117.

26. L. Burel, M. Mostafavi, S. Murata and M. Tachiya, *J. Phys. Chem. A*, 1999, **103**, 5882–5888.

27. M. A. Smitha, E. Prasad and K. R. Gopidas, *J. Am. Chem. Soc.*, 2001, **123**, 1159–1165.

28. V. S. Gladkikh, A. I. Burshtein, H. L. Tavernier and M. D. Fayer, *J. Phys. Chem. A*, 2002, **106**, 6982–6990.

29. V. O. Saik, A. A. Goun, J. Nanda, K. Shirota, H. L. Tavernier and M. D. Fayer, *J. Phys. Chem. A*, 2004, **108**, 6696–6703.

30. M. Tachiya and K. Seki, *J. Phys. Chem. A*, 2007, **111**, 9553–9559.

31. A. Rosspeintner, D. R. Kattnig, G. Angulo, S. Landgraf and G. Grampp, *Chem. - A Eur. J.*, 2008, **14**, 6213–6221.

32. N. R. Lokan, M. N. Paddon-Row, M. Koeberg and J. W. Verhoeven, *J. Am. Chem. Soc.*, 2000, **122**, 5075–5081.

33. A. M. Napper, I. Read, R. Kaplan, M. B. Zimmt and D. H. Waldeck, *J. Phys. Chem. A*, 2002, **106**, 5288–5296.

34. M. B. Zimmt and D. H. Waldeck, *J. Phys. Chem. A*, 2003, **107**, 3580–3597.

35. R. A. Marcus, *Discuss. Faraday Soc.*, 1960, **29**, 21–31.

36. G. L. Closs, L. T. Calcaterra, N. J. Green, K. W. Penfield and J. R. Miller, *J. Phys. Chem.*, 1986, **90**, 3673–3683.

37. I. R. Gould, D. Ege, S. L. Mattes and S. Farid, *J. Am. Chem. Soc.*, 1987, **109**, 3194–3196.

38. R. A. Marcus and P. Siders, *J. Phys. Chem.*, 1982, **86**, 622–630.

39. S. J. Formosinho, L. G. Arnaut and R. Fausto, *Prog. React. Kinet.*, 1998, **23**, 1–90.

40. S. Murata and M. Tachiya, *J. Phys. Chem. A*, 2007, **111**, 9240–9248.

41. M. Tachiya and S. Murata, *J. Phys. Chem.*, 1992, **96**, 8441–8444.

42. R. A. Marcus, *J. Chem. Phys.*, 1956, **24**, 966–978.

43. T. Kakitani, N. Matsuda, A. Yoshimori and N. Mataga, *Prog. React. Kinet.*, 1995, **20**, 347–381.

44. O. F. Mohammed and E. Vauthey, *J. Phys. Chem. A*, 2008, **112**, 5804–5809.

45. N. Mataga, Y. Kaifu and M. Koizumi, *Bull. Chem. Soc. Jpn.*, 1955, **28**, 690–691.

46. E. Lippert, *Zeitschrift fur Naturforsch. A J. Phys. Sci.*, 1955, **10**, 541–545.

47. D. R. Lide, *Handbook of Chemistry and Physics*, Internet V edn, 2005.

48. S. E. Mylon, S. N. Smirnov and C. L. Braun, *J. Phys. Chem. A*, 1998, **102**, 6558–6564.

49. H. Oevering, J. W. Verhoeven, M. N. Paddon-Row and J. M. Warman, *Tetrahedron*, 1989, **45**, 4751–4766.

50. H. Beens, H. Knibbe and A. Weller, *J. Chem. Phys.*, 1967, **47**, 1183–1184.

51. M. R. Wasielewski, D. W. Minsek, M. P. Niemczyk, W. A. Svec and N.-C. Yang, *J. Am. Chem. Soc.*, 1990, **112**, 2823–2824.

52. F. Brouwer, *Conform. Anal. Mol. Excit. States*, Wiley-VCH, New York, 2000.

53. M. L. Connolly, *Science*, 1983, **221**, 709–713.

54. S. V. Rosokha and J. K. Kochi, *Acc. Chem. Res.*, 2008, **41**, 641–653.

55. S. V. Rosokha, M. D. Newton, A. S. Jalilov and J. K. Kochi, *J. Am. Chem. Soc.*, 2008, **130**, 1944–1952.

56. E. S. Pysh and N. C. Yang, *J. Am. Chem. Soc.*, 1963, **85**, 2124–2130.

57. S. L. Murov, I. Carmichael and G. L. Hug, *Handbook of Photochemistry*, Marcel Dekker, Inc., New York, 2nd edn, 1993.

58. Y. Marcus, *The Properties of Solvents*, 1998, vol. 53, pp. 1689–1699.

59. J. C. Gjaldbaek and E. K. Andersen, *Acta Chem. Scand.*, 1954, **8**, 1398–1413.

60. K. R. Naqvi and T. B. Melø, *Chem. Phys. Lett.*, 2006, **428**, 83–87.

61. M. O. Delcourt and M. J. Rossi, *J. Phys. Chem.*, 1982, **86**, 3233–3239.

62. R. Gschwind and E. Haselbach, *Helv. Chim. Acta*, 1979, **62**, 941–955.

63. R. Cooper and J. K. Thomas, *J. Chem. Phys.*, 1968, **48**, 5103–5109.

64. I. R. Gould, D. Ege, J. E. Moser and S. Farid, *J. Am. Chem. Soc.*, 1990, **112**, 4290–4301.

65. S. Ojima, H. Miyasaka and N. Mataga, *J. Phys. Chem.*, 1990, **94**, 7534–7539.

66. I. R. Gould, D. Noukakis, L. Gomez-Jahn, R. H. Young, J. L. Goodman and S. Farid, *Chem. Phys.*, 1993, **176**, 439–456.

67. K. Wynne, C. Galli and R. M. Hochstrasser, *J. Chem. Phys.*, 1994, **100**, 4797–4810.

68. H. Miyasaka, S. Kotani, A. Itaya, G. Schweitzer, F. C. DeSchryver and N. Mataga, *J. Phys. Chem. B*, 1997, **101**, 7978–7984.

69. A. Rosspeintner, G. Angulo and E. Vauthey, *J. Am. Chem. Soc.*, 2014, **136**, 2026–2032.

70. I. R. Gould, D. Noukakis, L. Gomez- Jahn, J. L. Goodman and S. Farid, *J. Am. Chem. Soc.*, 1993, **115**, 4405–4406.

71. M. Goes, M. De Groot, M. Koeberg, J. W. Verhoeven, N. R. Lokan, M. J. Shephard and M. N. Paddon-Row, *J. Phys. Chem. A*, 2002, **106**, 2129–2134.

72. H.-S. Ren, M.-J. Ming, J.-Y. Ma and X.-Y. Li, *J. Phys. Chem. A*, 2013, **117**, 8017–8025.

73. J. V. Beitz and J. R. Miller, *J. Chem. Phys.*, 1979, **71**, 4579–4595.

4 Lifting Exothermic Rate Restrictions in Electron Transfers - Faster with a Barrier?

It was pointed out in chapter 1 and 3 that studies in intramolecular systems are crucial for a better understanding of the electron transfer process. In this chapter, we focus on the photoinduced intramolecular electron transfer in rigidly bridged donor/acceptor systems. For this purpose, two steroid derivatives, compounds **1** and **2**, were investigated.[1] Their structures, together with the ones of parent donors and acceptor molecules are shown on Figure 4.1. Compound **1** and **2** differ by the presence and absence of a methoxy group attached to the aromatic ring, what makes the latter a better electron-donor. Both molecules contain a 1,1-dicyanoethene group connected to the steroid ring D, that plays the role of an electron-acceptor.

These compounds have several structural characteristics that facilitate the study of electron transfer reactions:

1. Due to the rigid structure of the bridge, the relative distance and orientation of the donor and acceptor moieties is well-defined. This prevents the molecule from undergoing large structural changes before and after excitation,[2] and minimizes the occurrence of radiationless processes other than ET. In addition, the short separation distance ensures a relatively high electronic coupling.

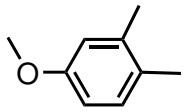

3,4-Dimethylanisole (dMA)
E^{ox} = 1.37 V

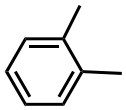

o-Xylene (oXy)
E^{ox} = 2.09 V

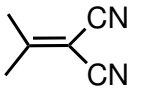

Isopropylidenemalononitrile (iPN)
E^{red} = -1.69 V

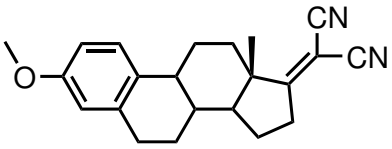

1
3-methoxy-1,3,5(10)-estratrien-17-yliden)malononitrile

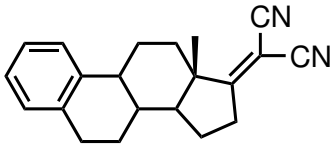

2
1,3,5(10)-estratrien-17-yliden)malononitrile

Figure 4.1 Structures of **1** and **2,** together with other structurally related donors (dMA, oXY) and acceptor (iPN) molecules.

2. Planar structures with all-trans saturated bonds, assure a dominant role of through-bond interaction over through-solvent interaction. Additionally, due to lack of π-bonds, electron delocalization does not play a role in ET.

3. The redox properties of the donor and acceptor allow the investigation of charge recombination in very exothermic reactions.

4. The optically-transparent dicyanoethene acceptor excludes energy transfer as a possible quenching pathway of a locally-excited singlet state.

Electron transfer reaction followed by emission from the intramolecular exciplex/ charge-transfer state in **1** has been investigated by Verhoeven and co-workers in 1985.[1] They studied ET in n-hexane, diethyl ether, acetonitrile and methanol, and observed quenching of the fluorescence emission of a locally excited singlet state ($^1\mathbf{1}$) in all solvents. However, formation of the emissive charge-transfer state ($^1\mathbf{1}^{\pm}$) was only observed in diethyl ether (τ_{CT}=19 ns). They estimated an electron transfer

rate of $k_{ET} > 10^{11}\mathrm{s}^{-1}$, but precise measurement of the rates was beyond their experimental detection limit.

In this chapter, compounds **1** and **2** were investigated using several techniques which allow the characterization of ultrafast to relatively slow processes. The studies of free-energy and temperature dependencies were performed in a set of middle polarity solvents. Collected experimental data were compared with the theoretical predictions and organized in form of the article entitled: **"Lifting Exothermic Rate Restrictions in Electron Transfers - Faster with a Barrier?"**, which was submitted to the *Journal of the American Chemical Society* on July 2017. The findings presented in this article, extended by some additional information are discussed below.

4.1 Introduction

Electron transfer (ET) reactions are arguably the simplest chemical reactions but they have not yet ceased to intrigue chemists. They are implicated in fundamental processes in Chemistry and Biology,[3–5] and have been under intense scrutiny since Marcus related ET rates to solvent (λ_s) and molecular vibration (λ_v) reorganization energies.[6,7] The most distinctive features of ET reactions are: (i) a free-energy dependence characterized by an increase in the rates as their exothermicities increase, followed by their decrease for very exothermic reaction (the Marcus "inverted" region); (ii) remarkably fast rates even when electron donor and acceptor moieties are separated by long and rigid spacers.[8,9] A particularly convenient strategy to trigger ET reactions is the electronic excitation of the electron donor or acceptor, and photoinduced ET reactions have found applications in solar cells,[10–15] organic light-emitting diodes (OLEDs),[16] water splitting[17–19] and optoelectronics.[20,21] Electron donor-acceptor moieties covalently linked by a rigid spacer provide valuable insight into ET rates because they allow for precise control of both V and $\triangle G^0$,[3,22,23] and are particularly relevant for the fabrication of solar energy conversion and organic electronic devices.[24,25] The rigid donor-spacer-acceptor molecules synthesized in this

work were designed with a view to explore the Marcus "inverted" region, the relevance of solvent *vs.* molecular reorganization energies, and the origin of energy barriers in ET reactions. Our systems enable the control over ET reactions covering 100 kcal/mol in exothermicities and 140°C in temperature. We show that exothermic rate restrictions have a limit, that dielectric continuum models overestimates λ_s in weakly and moderately polar solvents (i.e., dielectric constants between 2.6 and 16), and that the activationless rates in the inverted region are followed by faster rates with positive activation energies (E_a) at higher exothermicities. The new findings can be explained by the increase of the reorganization energy with the driving force of the reactions.

The ability to explore the free-energy dependence of very exothermic ET reactions, often believed to be deep in the Marcus inverted region and slow, depends on the design of molecular systems that can be investigated over wide $\triangle G^0$ and T ranges without changes in reaction mechanism or electronic coupling. Compounds **1**[1] and **2** (Figure 4.1) have stable and high-energy chromophores based on the benzene ring that act as electron donors in the excited singlet state, covalently linked via a rigid spacer to stable and optically transparent dicyanoethene working as an electron acceptor. Intersystem crossing in the charge-separated state reached by photoinduced ET may compete with charge recombination to the ground state, and lead to triplet charge-separated species that may undergo charge recombination to the locally-excited triplet state. This decay channel was controlled keeping the D–A distance sufficiently short to enable charge separation (k_{CS}) and charge recombination (k_{CR}) rates competitive with intersystems crossing (k_{isc}) rates, but long enough to allow for proper characterization of charge transfer species. The rigidity of the system is also critical both to provide well-defined reactive species, electronic coupling and to minimize radiationless processes other than ET.

4.2 Results and Discussion

The synthesis of estrone derivatives **1** and **2** is outlined in Figure 4.2 and followed described procedures[9,26,27], described in Appendix A. Characterization of **1** and **2** is also presented in Appendix A.

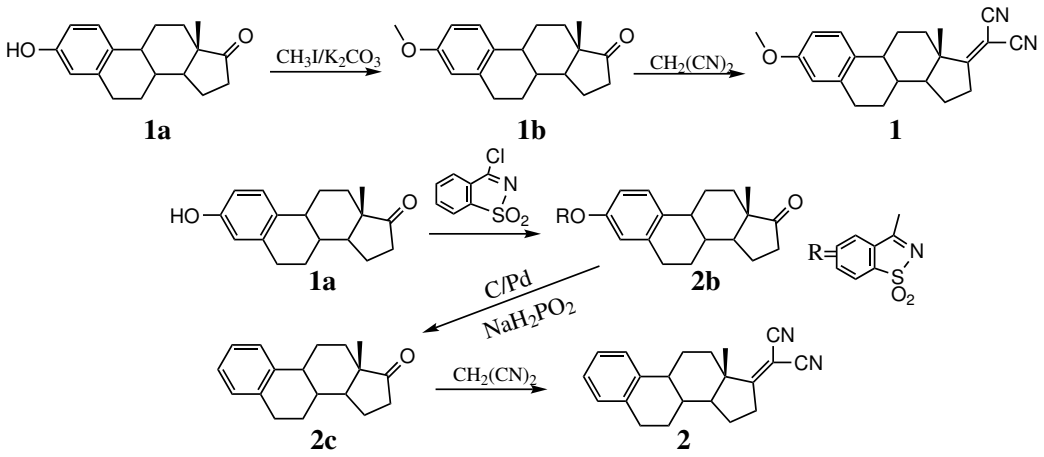

Figure 4.2 Synthesis of **1** and **2**

Conformational search with GAMESS[28] using the B3LYPV1R hybrid functional[29–31] and the 6-31G(d) Pople basis set for all atoms,[32] revealed the presence of only one low energy conformer in the ground state of **1**, with a distance from the center of the aromatic ring to the carbon bond to the two CN groups r_c= 7.8 Å and an edge-to-edge distance r_e= 5.9 Å. All singlet states were described using RHF formalism and the triplet state used UHF formalism. There was no relevant spin contamination on the UHF calculations, <S2>=2.022. The frontier molecular orbitals of electron donor and acceptor states are shown in Figure 4.3. The singly occupied molecular orbitals of $^1\mathbf{1}^{\pm}$ are localized in benzene and dicyanoethene moieties. Interestingly, the nitrile groups are rotated by 82° in $^3\mathbf{1}^{\pm}$ with respect to $^1\mathbf{1}^{\pm}$, while the C=C bond increases from 1.36 Å in $^1\mathbf{1}$, 1.43 Å in $^1\mathbf{1}^{\pm}$ to 1.47 Å in $^3\mathbf{1}^{\pm}$ (Table 4.1). However, the nitrile groups have very similar orientations in $^1\mathbf{1}$, $^1\mathbf{1}^{\pm}$ and **1**, which means that the twisting of these groups is not involved in the reaction coordinates of singlet state charge separation and recombination.

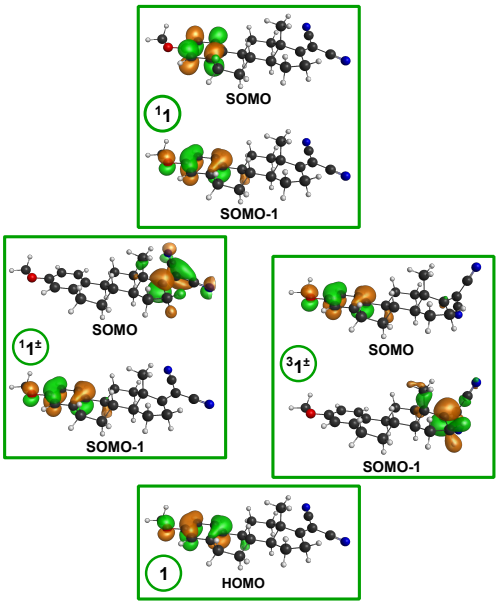

Figure 4.3 Relevant frontier molecular orbitals for molecule **1**.

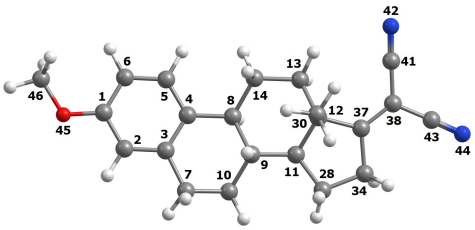

Figure 4.4 Numeration of the atoms in molecule **1**.

Table 4.1 Bond lengths (in Å) of benzene and dicyanoetylene moieties relevant for charge recombination, calculated by GAMESS. Numeration of the atoms is presented in Figure 4.4

	1	^{1}**1**	^{1}**1**$^\pm$	^{3}**1**$^\pm$
C1-C6	1.3979	1.4173	1.4248	1.3976
C5-C6	1.3957	1.4223	1.3717	1.3957
C4-C5	1.3996	1.4273	1.4295	1.3997
C3-C4	1.4133	1.4350	1.4425	1.4136
C2-C3	1.3948	1.4306	1.3757	1.3949
C1-C2	1.3981	1.4192	1.4240	1.3979
C4-C8	1.5306	1.5161	1.5097	1.5309
C1-O45	1.3663	1.3545	1.3209	1.3666
C43-N44	1.1635	1.1635	1.1739	1.1717
C38-C41	1.4349	1.4349	1.4109	1.4106
C37=C38	1.3606	1.3606	1.4324	1.4690
C38-C43	1.4365	1.4365	1.4132	1.4101
C41-N42	1.1635	1.1635	1.1755	1.1718

Electronic excitation of **1** is expected to lead to the ultrafast generation of its lowest singlet state ($^1\mathbf{1}$) followed by fast ET to a longer-lived charge-separated state ($^1\mathbf{1}^{\pm}$). The charge recombination rate ($^1k_{CR}$) of $^1\mathbf{1}^{\pm}$ to the ground state may have to compete with intersystem crossing rate ($^1k_{isc}$) to the triplet manifold. Hyperfine coupling is known to bring the electron spins to a triplet alignment with a rate constant of $\approx 10^8\,\mathrm{s}^{-1}$ for orbitals a few nanometers apart, with small singlet–triplet energy splitting (hfc-isc mechanism).[33] Alternatively, when the spin flip is coupled with a change in angular momentum, namely when the electron donating and accepting molecular orbitals are perpendicular, spin-orbit coupling is particularly efficient in promoting intersystems crossing (soc-isc mechanism).[34,35] The charge-separated triplet state ($^3\mathbf{1}^{\pm}$) may then return to $^1\mathbf{1}^{\pm}$ ($^3k_{isc}$), or decay to the long-lived triplet state ($^3\mathbf{1}$) by triplet charge recombination ($^3k_{CR}$) when $^3\mathbf{1}$ is energetically accessible ($E_T < E_{CT}$). The triplet yield of $^3\mathbf{1}$ is conveniently monitored by flash photolysis in view of its microsecond lifetime. Direct $^3\mathbf{1}^{\pm} \rightarrow \mathbf{1}$ spin-forbidden charge recombination may only compete with exothermic $^3\mathbf{1}^{\pm} \rightarrow {}^3\mathbf{1}$ when strong spin-orbit coupling is enabled by perpendicular electron donating and accepting molecular orbitals (soc-isc mechanism). On the other hand, the involvement of the triplet manifold may lead to bi-exponential decays of $^1\mathbf{1}^{\pm}$. The energies of $^1\mathbf{1}^{\pm}$ and $^3\mathbf{1}^{\pm}$ are dependent of the polarity of the solvent and, at least for this reason, charge recombination rates will depend of the solvent. Figure 4.5 presents the various decay pathways investigated in this work.

The spectroscopy of $^1\mathbf{1}$ gives $E_{S1} = 99\,\mathrm{kcal/mol}$. The triplet energy of $^3\mathbf{1}$, $E_{T1} = 80\,\mathrm{kcal/mol}$, was estimated from the phosphorescence of dMA (Figure C.1) and is consistent with the literature value for 1-methoxy-4-methylbenzene, $E_{T1} = 78\,\mathrm{kcal/mol}$.[36] The oxidation potential of **1** ($E_{ox} = 1.37\,\mathrm{V}$ vs SCE) was estimated from the oxidation potential of anisole[37] ($E_{ox} = 1.76\,\mathrm{V}$ vs SCE) by adding a correction value (-0.39 V), that accounts for the difference between the model molecules, benzene and o-xylene.[38] The average ionic radii of D^+ ($r_+ = 3.5$ Å) and A^- ($r_- = 3.2$ Å) were calculated by using the molar volume of the neutral molecules (described by

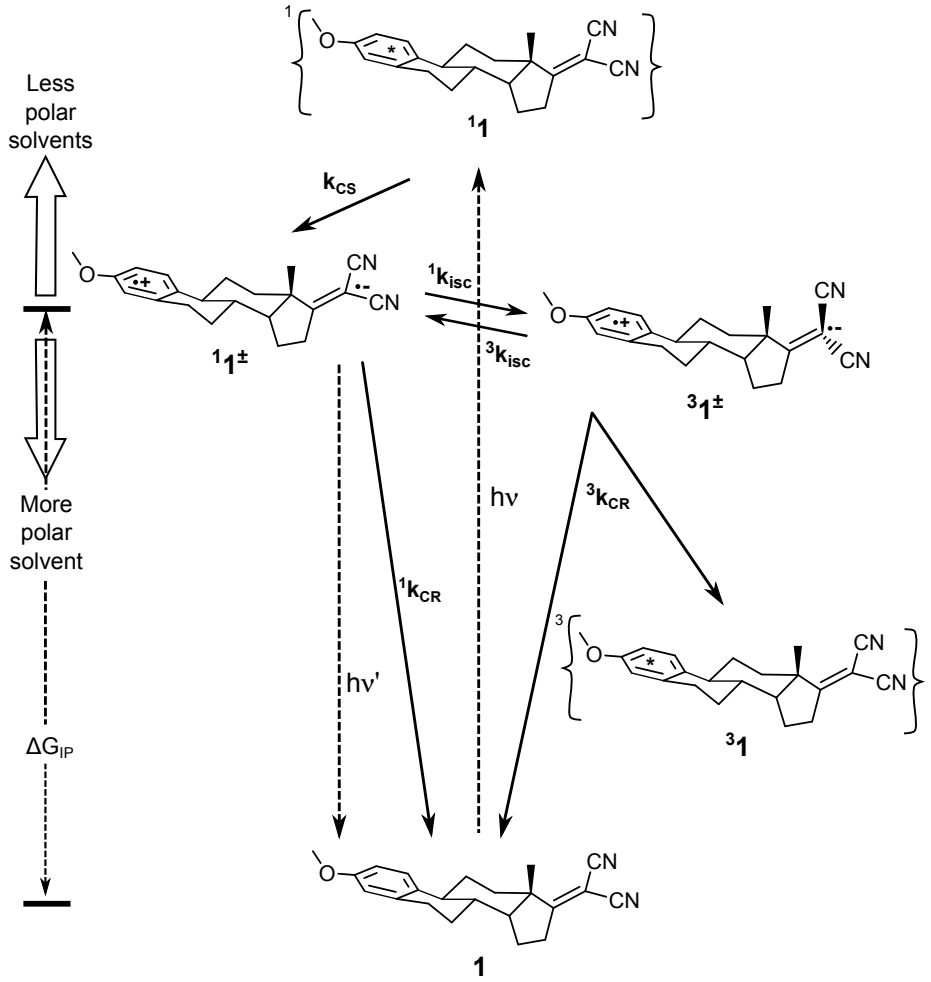

Figure 4.5 LE and CT states of **1**, and their charge separation and charge recombination rate constants. The vibrational relaxation from the initially populated Franck-Condon state is omitted for clarity. The energies of $^1\mathbf{1}^{\pm}$ and $^3\mathbf{1}^{\pm}$ depend on the solvent polarity. Molecule **2** is as **1** but without the methoxy group.

eq. 1.17), and by using anisole and fumaronitrile as donor and acceptor model molecules, respectively. The free-energy of $^1\mathbf{1}^{\pm}$ in a solvent of dielectric constant ε is given by the Weller expression[39] (eq. 1.21). Using the distance and redox potentials appropriate for **1**, we calculated ΔG_{CT} values of 86 kcal/mol in n-butyl ether (NBE) and 74 kcal/mol in dichloromethane (DCM) at room temperature (using data from Table C.1). In more polar solvents (e.g., DCM) $^3\mathbf{1}$ may not be energetically accessible from the charge-transfer states and the charge recombination of $^1\mathbf{1}^{\pm}$ may be sufficiently fast to originate single-exponential decays. In lower polarity solvents (e.g., NBE), where the charge-transfer states have higher energies, the system may

evolve along the reaction coordinate $^1\mathbf{1}^{\pm} \rightarrow {}^3\mathbf{1}^{\pm} \rightarrow {}^3\mathbf{1}$ competitively with charge recombination $^1\mathbf{1}^{\pm} \rightarrow \mathbf{1}$. Hence, in such solvents, the triplet manifold may be reached and allow for some reversibility leading to biexponential $^1\mathbf{1}^{\pm}$. Similar results were obtained for **2**, but the o-xylene (oXY) moiety has smaller ionic radius $r_+ = 3.3$ Å, higher singlet (E_{S1}=104 kcal/mol) as well as a higher oxidation potential (E_{ox}=2.09 V vs SCE),[38] which are reflected in energies of $^{1,3}\mathbf{2}^{\pm}$ CT states that are higher than the triplet energy of oXY (E_{T1}=82 kcal/mol),[36] for the solvents studied in this work. The calculated free-energies of $^1\mathbf{2}^{\pm}$ cover the range of exothermicities from $\Delta G_{CT} = 103$ kcal/mol in NBE to 91 kcal/mol in DCM at room temperature.

The absorption spectrum of **1** and **2** are compared with the sum spectra of model compounds in Figure 4.6. We observed a small bathochromic shift in the lowest energy absorption maximum of **1** relative to dMA+iPN (from 283 to 287 nm) and of **2** relative to oXy+iPN (from 271 to 273 nm). This is consistent with a weak coupling between donor and acceptor moieties in the ground state. The absorption spectra of **1** and **2** were not affected by the change of the solvent polarity.

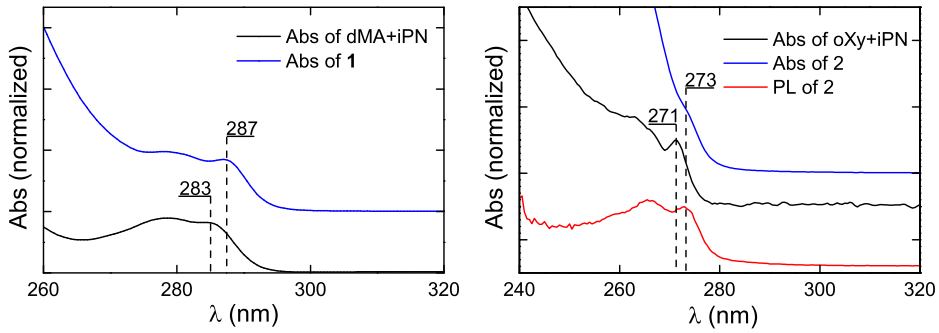

Figure 4.6 Left: Absorption spectrum of **1** and sum spectra of dMA+iPN (0.1mM each) in isopropyl ether. Right: Absorption spectrum of **2** in comparison with its fluorescence excitation spectrum and sum spectra of oXy+iPN (0.1mM each) in DCM.

The fluorescence spectrum of dMA in isopropyl ether (IPE), collected upon excitation at 283 nm, shows a band with maximum at 301 nm, corresponding to the ^1D, which is quenched by the addition of iPN (Figure 4.7). The absorption spectrum of the acceptor excludes energy transfer as a quenching mechanism in dMA/iPN donor/acceptor pair system.[40] We did not observe a formation of new band, which

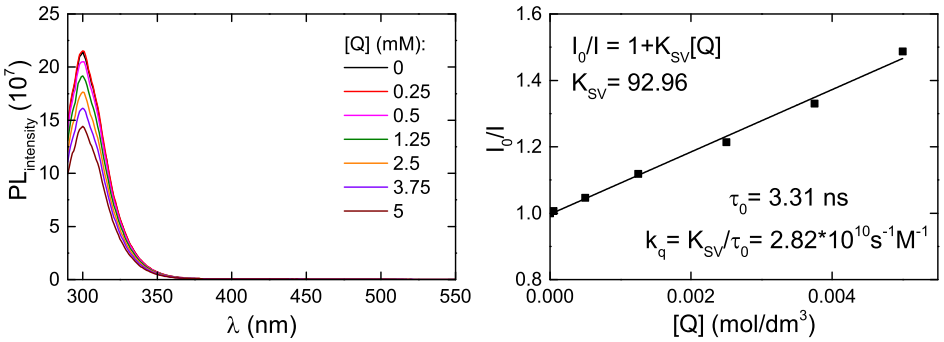

Figure 4.7 Fluorescence spectra of dMA in IPE (left) in the presence of various concentration of the iPN and corresponding Stern-Volmer plot (right). τ_0 was taken from SPC.

could correspond to the charge-transfer species. Lack of the emissive CT state, when iPN plays role of an electron-acceptor was reported previously in the literature.[40] The change of acceptor from FN (presented in chapter 3) to iPN (its constitutional isomer) enhanced the electron affinity of the acceptor and as a result, increased the energy gap between ^1D and the CT state (~8.3 kcal/mol). The quenching rate constant was determined from the Stern-Volmer plot ([iPN] = 0-5 mM) and is equal to $k_q = 2.82 \cdot 10^{10}\,\mathrm{s^{-1}M^{-1}}$ in IPE (Figure 4.7). The studies of the dMA/iPN system are consistent with diffusion-controlled quenching by ET with the generation of the species with the strong charge-transfer character. Transient absorption spectroscopy needs to be employed to study the non-emissive CT state.

Steady-state fluorescence of **1** (λ_{ex}=287 nm) shows a virtually complete quenching of the locally-excited singlet state, $^1\mathbf{1}$, which is poorly visible at 303 nm ($\Phi_{PL}<$ 0.001) in comparison with the emission of the model dMA/iPN system. A low Φ_{PL} value indicates the small importance of the radiative transition ($^1\mathbf{1} \rightarrow \mathbf{1}$) in the methoxybenzene excited-state deactivation. The level of quenching suggests an efficient electron transfer from the donor to the rigidly bridged acceptor, which corresponds to $^1\mathbf{1} \rightarrow {}^1\mathbf{1}^{\pm}$ transition. In the weakly polar solvents a new broad, structureless band assigned to the charge-transfer state, was observed. This band was red-shifted in comparison with locally-excited state emission, with maximum at 400, 420, 469, 490 and 515 nm in n-butyl ether (NBE), isopropyl ether (IPE), chloroform (CHF), ethyl acetate (EAC) and dichloromethane (DCM), respectively.

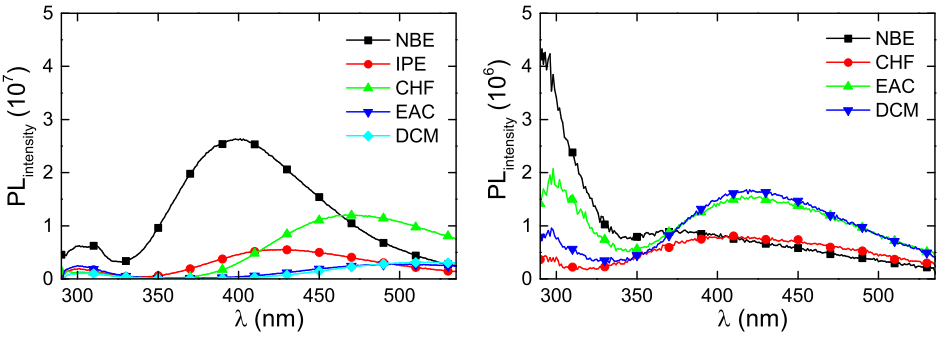

Figure 4.8 Emission spectra of molecule **1** (left) and **2** (right) measured after excitation at 287 and 273 nm, respectively, measured in the solvents indicated in the figure.

The fluorescence spectrum of **2** (λ_{ex}=273 nm) exhibits a poorly visible band with maximum at 290 nm, corresponding to the ^{1}**2**. The emission intensity of ^{1}**2**$^{\pm}$ was weaker and the bathochromic shift was less pronounced than in ^{1}**1**$^{\pm}$. The maximum of the CT state bands was found at 375, 400, 419, 420 nm in NBE, CHF, EAC and DCM, respectively. The fluorescence spectra of **1** and **2** in various solvents are shown in Figure 4.8.

The solvent dependencies of CT emission for **1** and **2** are presented using Lippert-Mataga plot in Figure 4.9. Table 4.2 provides the values of ε and n_D and Δf. The slope of the Lippert-Mataga plot together with the long axis of **1** and ellipsoidal approximation,[1] lead to a dipole moment μ=35 D. A full charge separation at r_c=7.8 Å should correspond to μ=37 D. GAMESS calculations also give μ=37 D. Hence, electronic excitation of **1** in solvents with ε>3 leads to an essentially complete electron transfer. The slope of the Lippert-Mataga plat of **2** leads to μ=26 D, but the CT state ^{1}**2**$^{\pm}$ can still be regarded as the result of an ET reaction.

Table 4.2 Values used to calculate the dipol moment using Lippert-Mataga plot.

Solvent	ε	n_D	Δf	$\bar{\nu}_{CT}$ $(10^3\,cm^{-1})$	
				1	2
NBE	3.10	1.399	0.194	25.0	26.2
IPE	4.19	1.368	0.248	23.8	-
CHF	4.81	1.446	0.253	21.3	24.4
EAC	6.08	1.372	0.293	20.4	23.8
DCM	9.00	1.424	0.319	19.4	23.8

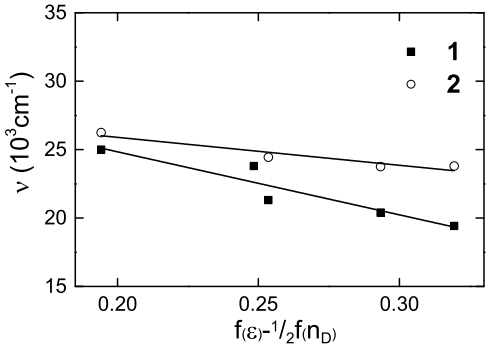

Figure 4.9 Lippert-Mataga plots of **1** (black squares) and of **2** (open circles).

The thermochromic shift of the charge-transfer band has also been observed. The CT emission spectra of **1** in IPE (198-293 K) and of **2** in DCM (223-300 K) are shown in Figure 4.10. The thermochromic behavior was accompanied with the increase of emission intensity, what it is in contradiction to data obtained for bi-molecular system in methyl acetate (chapter 3). The thermochromism was more pronounced in **1** in IPE, the CT emission gradually shifted to the longer wavelength with an average of ∼27 cm^{-1}/K. For **2** in DCM an average shift was ∼16 cm^{-1}/K. The CT emission shift is related to the changes in the solvent dielectric constant, which occur by altering the temperature.

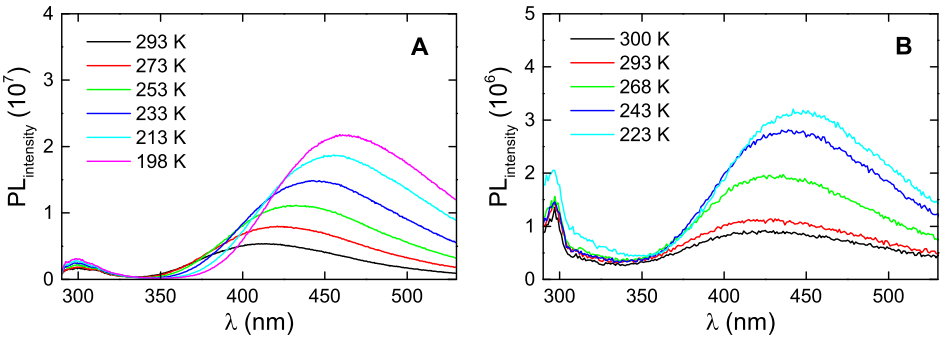

Figure 4.10 Fluorescence spectra of: (A) **1** in isopropyl ether ($\lambda_{ex} = 287\,nm$) and (B) **2** in dichloromethane ($\lambda_{ex} = 273\,nm$, Raman band was not subtracted) measured at various temperatures.

The weak and short-lived fluorescence of $^1\mathbf{1}$ or $^1\mathbf{2}$ motivated the use of ultrafast transient absorption to determine their lifetimes. Three Evolution-Associated Spectra (EAS) were needed to describe the dynamics of dMA in isopropyl ether (IPE). The excitation of dMA generates a Franck-Condon state $\left(^1D^*\right)$ that relaxes in 1.4 ps to the singlet state $\left(^1D\right)$, which then decays in 3.1 ns and leaves a persistent species assigned to triplet state $\left(^3D\right)$. Hence, a kinetic model of three consecutive first-order reactions $^1D^* \rightarrow {}^1D\,(\rightarrow) \rightarrow {}^3D$ is adequate to describe this system. Figure 4.11 presents the transient spectra collected at various time delay and the Evolution-Associated Spectra (EAS) obtained with Glotaran. The quenching of $^1D^*$ by 0.1 M iPN occurs over a range of distances as the donor and acceptor molecules diffuse in solution. Most meaningful are the shortest-lived EAS, spectroscopically similar to $^1D^*$, and the longed-lived one, with a ~460 nm band characteristic of the anisole radical cation.[41]

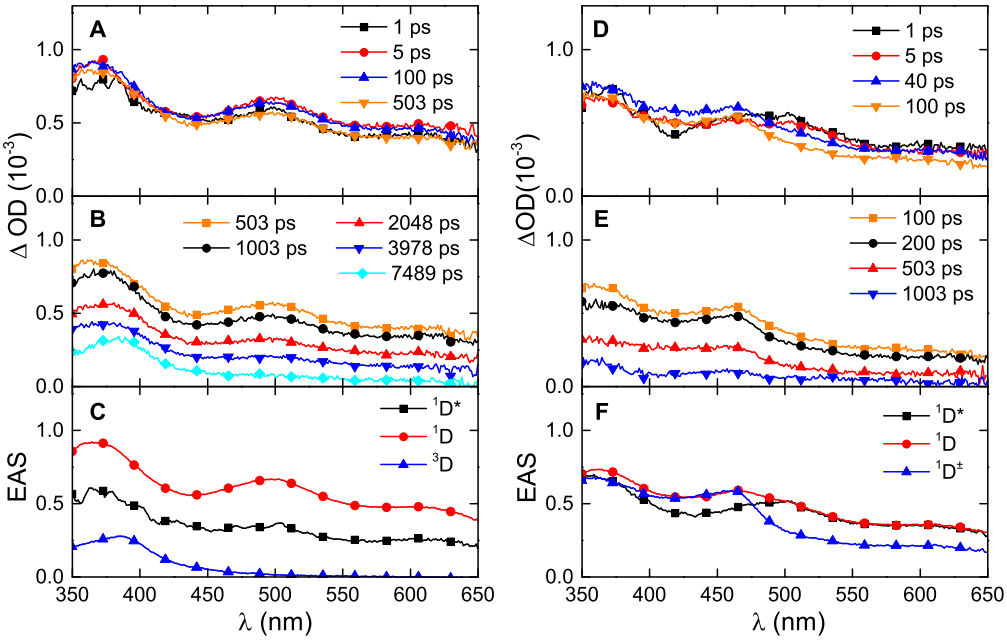

Figure 4.11 Transient absorption spectra of 3,4-dimethylanisole in isopropyl ether in short and long time scales, either in the absence (A,B) and presence of 0.1 M of isopropylidene-malononitrile (D,E). Evolution-Associated Spectra in the absence (C) and presence (F) of acceptor are presented.

Apart from the ultrafast lifetime below 1 ps assigned to the decay of the Franck-Condon state, two lifetimes between 1 ps and 20 ns are necessary to fit transient absorption spectra of **1** in dichloromethane, ethyl acetate and chloroform, and three lifetimes are needed for ethers at room temperature, whereas three lifetimes are necessary for **2**. Target analysis using the model of Figure 4.5 gives the Species Associated Spectra (SAS) shown in Figure 4.12 and Figure C.4. A species with a spectrum similar to that of ^1D and a lifetime between 4 and 10 ps was observed in all solvents and assigned to $^1\mathbf{1}$. A species generated from $^1\mathbf{1}$ and a band at 472–477 nm was assigned to $^1\mathbf{1}^{\pm}$. It was found that **1** in chlorinated solvents and ethyl acetate follow first-order kinetics $^1\mathbf{1} \rightarrow {}^1\mathbf{1}^{\pm} \rightarrow \mathbf{1}$. In ethers, an additional species was found necessary to fit the spectra, its spectrum was similar to that of $^1\mathbf{1}^{\pm}$ and was assigned to $^3\mathbf{1}^{\pm}$. The intersystem crossing pathway, $^1\mathbf{1}^{\pm} \rightleftharpoons {}^3\mathbf{1}^{\pm}$, was included in the target analysis model for these solvents. Transient absorption spectra of **1** in EAC and IPE at various time delays are presented in Figure 4.12. A simultaneous decay of the shoulder between 500 and 650 nm and rise of the band with maximum around 475 nm can be observed (Figure 4.12 A). 2D images of the collected data are presented in Figure C.2. Analogous assignments were made for **2**, although the bands are weaker. Measured ΔOD were on the limit of the experimental detection, thus it was possible to calculated Species-Associated Spectra only in chloroform (Figure 4.13 F), using the same target model as for **1** in ethers. Global analysis was applied to the others solvents, giving us information about the number of transient species and their lifetimes. The electron transfer is slightly slower in **2** (9-46 ps) in comparison with **1**, however lifetime of charge transfer state is clearly shorter in the former one, for which driving forces are larger. The transient spectra collected at various time delays in EAC and CHF are shown in Figure 4.13. Table 4.3 and Table 4.4 present the lifetimes obtained by the target analysis.

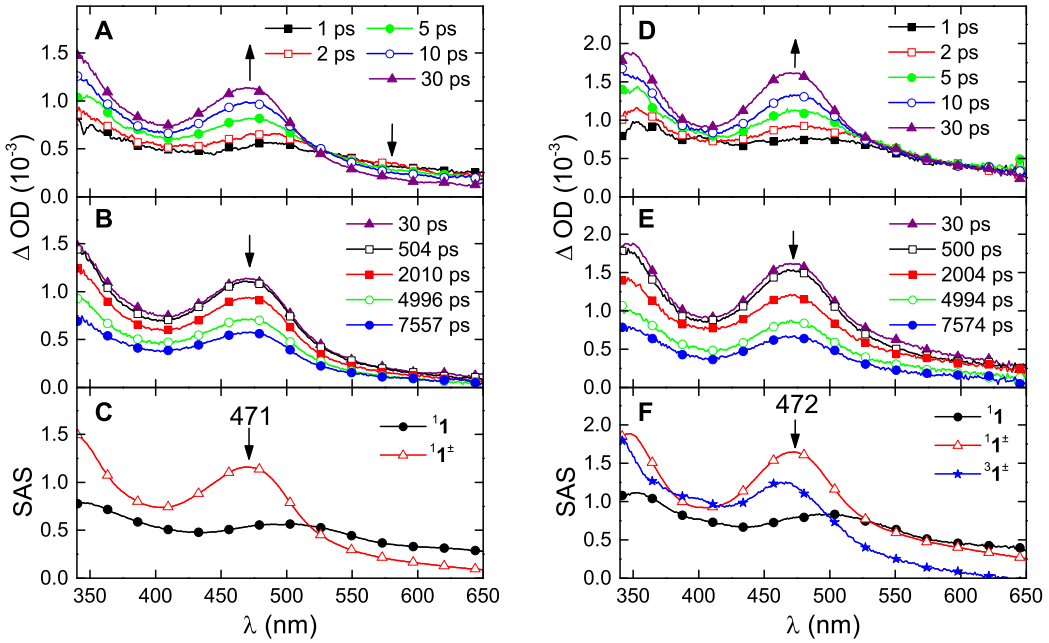

Figure 4.12 Transient absorption spectra of **1** in ethyl acetate (A,B) and isopropyl ether (D, E), at various time delays and corresponding Species-Associated Spectra (C, F).

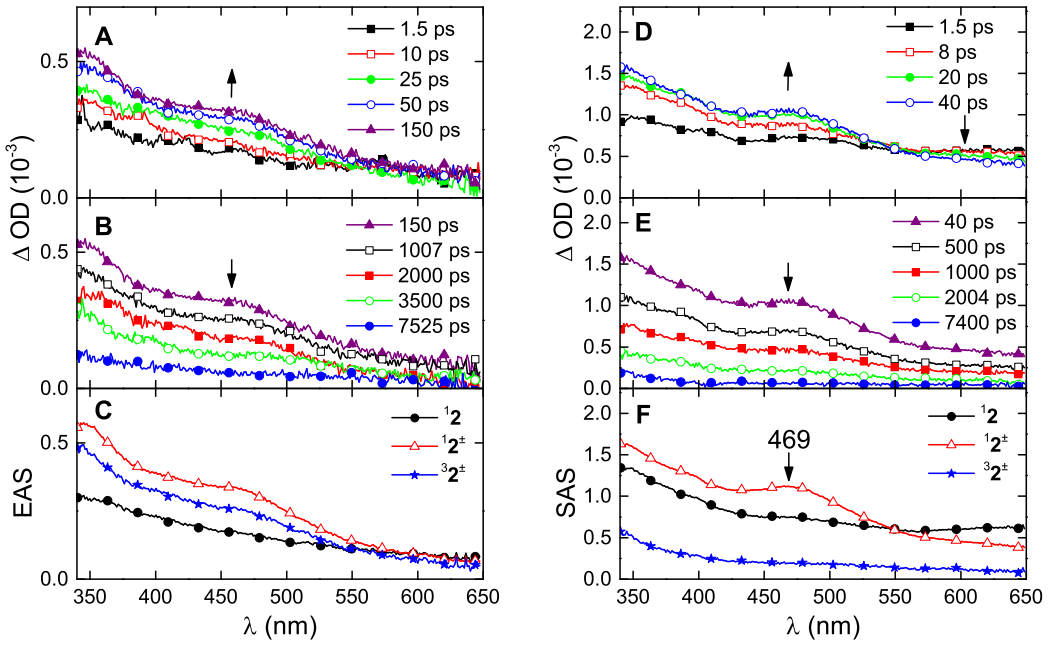

Figure 4.13 Transient absorption spectra of **2** in ethyl acetate (A,B) and chloroform (D, E), at various time delays and corresponding Evolution-Associated Spectra in ethyl acetate (C) and Species-Associated Spectra in chloroform (F).

Table 4.3 Lifetimes of Species-Associated Spectra of **1** obtained by femtosecond transient absorption.

Solvent	T(K)	τ_{CS}	τ_1	τ_2
NBE	323	8.23 ps	0.93 ns	5.41 ns
	308	6.62 ps	0.70 ns	8.09 ns
	293	8.42 ps	1.76 ns	10.26 ns
	276	8. 40 ps	1.21 ns	14.29 ns
	253	7.85 ps	0.52 ns	17.87 ns
IPE	293	8.70 ps	1.40 ns	9.43 ns
CHF[a]	323	3.97 ps	-	10.20 ns
	293	6.60 ps	-	14.68 ns
	276	6.63 ps	-	13.81 ns
	253	7.96 ps	-	13.26 ns
EAC	293	8.23 ps	-	10.15 ns
DCM	293	4.06 ps	-	13.82 ns
	276	3.95 ps	-	11.58 ns
	253	4.34 ps	-	9.53 ns
	223	4.07 ps	-	9.45 ns
	188	5.01 ps	-	5.65 ns

[a] an additional decay lifetime would improve the fitting but with the spectrum unrelated to all other spectra observed in this work. Solvent purity significantly changes the contribution of this additional lifetime to the fitting.

Table 4.4 Lifetimes of Evolution-Associated Spectra of **2** obtained by femtosecond transient absorption at 293K.

Solvent	τ_{CS}	τ_1	τ_2	τ_{tail}
NBE	46.23 ps	-	0.22 ns	6.47 ns
CHF	12.09 ps	-	1.00 ns	13.53 ns
EAC	39.15 ps	0.45 ns	4.90 ns	
DCM	9.31 ps	0.20 ns	6.96 ns	

Fluorescence lifetime, $\tau_F(D)$, of dMA in IPE, EAC and DCM (measured in the presence of oxygen) was adequately fitted with monoexponential decay function and lifetimes of 3.31, 4.35 and 0.88 ns were obtained, respectively, using TCSPC (Figure 4.14). $\tau_F(D)$ obtained in DCM is shorter, due to enhanced intersystem crossing to triplet state $({}^3D)$, increased by solvent heavy atom effect.

The fluorescence from $^1\mathbf{1}$ or $^1\mathbf{2}$ was too short-lived and/or weak for use of picosecond SPC apparatus. Therefore, the lifetimes of $^1\mathbf{1}$ and $^1\mathbf{2}$ could only be studied with ultrafast transient absorption. On the other hand, populated charge-transfer states were emissive and thus, the fluorescence decays of $^1\mathbf{1}^{\pm}$ and $^1\mathbf{2}^{\pm}$ could be conveniently followed by SPC, using a 350 ps NanoLED excitation at 282 nm or a 5 ps laser excitation at 272 nm, respectively.

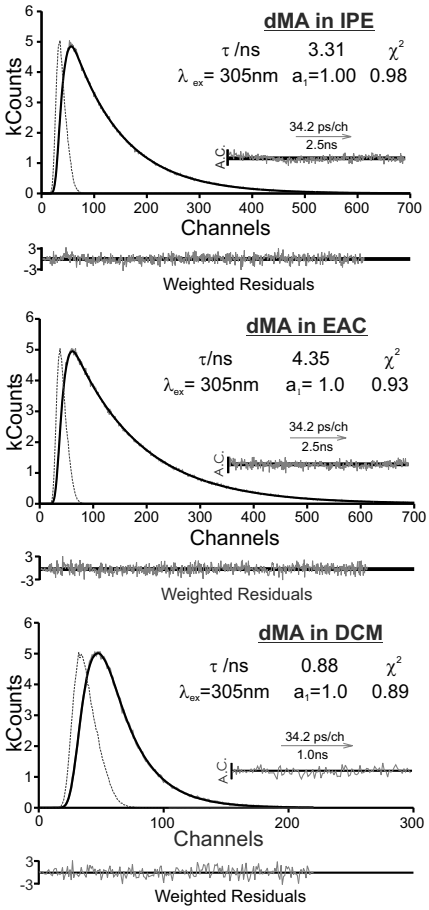

Figure 4.14 Fluorescence decays of dMA with applied monoexponential fitting in IPE, EAC and DCM, after excitation at 282 nm, at 20°C.

Fluorescence decay fitting for $^1\mathbf{1}^{\pm}$ in DCM, EAC and CHF was monoexponential in all studied temperatures. However two exponentials were required to fit the decays of $^1\mathbf{1}^{\pm}$ in the lower polarity solvents such as NBE and IPE and to the decays of $^1\mathbf{2}^{\pm}$ in all studied solvents and temperatures. Here, $^1\mathbf{2}^{\pm}$ is higher in the energy that $^3\mathbf{2}$ in all solvents. Collected decays at room temperature are presented in Figure 4.15 for **1** and Figure 4.16 for **2**, the decays in other temperatures can be found in Appendix C. All collected fluorescence lifetimes and their weights to the decays (measured close to the maximum of the fluorescence emission) are presented in Table 4.5 for **1** and Table 4.6 for **2**.

Table 4.5 Lifetimes of $^1\mathbf{1}^{\pm}$ obtained by SPC in various solvents and temperatures.

Solvent	T (K)	λ_{em} (nm)	τ_1 / a_1	τ_2/ a_2
NBE	323	390	0.8 ns / 21%	4.3 ns / 79%
	308	395	1.3 ns / 24%	6.5 ns / 76%
	303	395	1.0 ns / 38%	10.0 ns / 62%
	293	400	1.9 ns / 29%	9.0 ns / 71%
	276	410	2.9 ns / 25%	11.4 ns / 75%
	258	420	3.7 ns / 16%	13.1 ns / 84%
	253	410	2.9 ns/ 23%	16.1 ns / 77%
	243	430	2.4 ns / 16%	20.6 ns / 84%
	238	435	4.9 ns / 19%	22.8 ns / 81 %
	203	445	8.8 ns / 15%	46.8 ns / 85%
	193	445	13.9 ns / 15%	56.3 ns / 85%
IPE	293	420	1.1 ns / 32%	8.7 ns / 68%
CHF	328	450	-	16.7 ns / 100%
	318	455	-	16.7 ns / 100%
	308	460	-	17.7 ns /100%
	293	470	-	17.4 ns / 100%
	276	480	-	15.2 ns / 100%
	258	480	-	13.0 ns / 100%
EAC	293	490	-	10.4 ns / 100%
DCM	293	490	-	13.7 ns / 100%
	276	520	-	11.2 ns / 100%
	253	525	-	9.3 ns / 100%
	223	540	-	8.4 ns / 100%
	188	545	-	5.6 ns / 100%

Table 4.6 Lifetimes of $^1\mathbf{2}^{\pm}$ obtained by SPC in various solvents and temperatures.

Solvent	T (K)	λ_{em} (nm)	τ_1 / a_1	τ_2/ a_2
NBE	293	375	0.28 ns / 50%	2.08 ns / 50%
CHF	308	395	0.52 ns / 66%	2.28 ns / 34%
	293[a]	400	0.44±0.14 ns/ 49%	1.93±0.16 ns / 51%
	273	405	0.33 ns / 42%	2.60 ns / 58%
	238	417	0.23 ns / 39%	3.41 ns / 61%
	218	423	0.29 ns / 32%	3.76 ns / 68%
EAC	293[a]	420	0.34±0.04 ns / 26%	3.21±0.17 ns / 74%
DCM	293[a]	420	0.35±0.06 ns / 30%	3.86±0.20 ns / 70%
	276	425	0.38 ns / 28%	4.14 ns / 72%
	263	430	0.46 ns / 26%	4.32 ns / 74%
	243	441	0.41 ns / 26%	4.50 ns / 74%
	213	449	0.47 ns / 25%	4.58 ns / 75%
	188	456	0.47 ns / 26%	4.61 ns / 74%

[a] Average and sample standard deviation of three to six independent measurements.

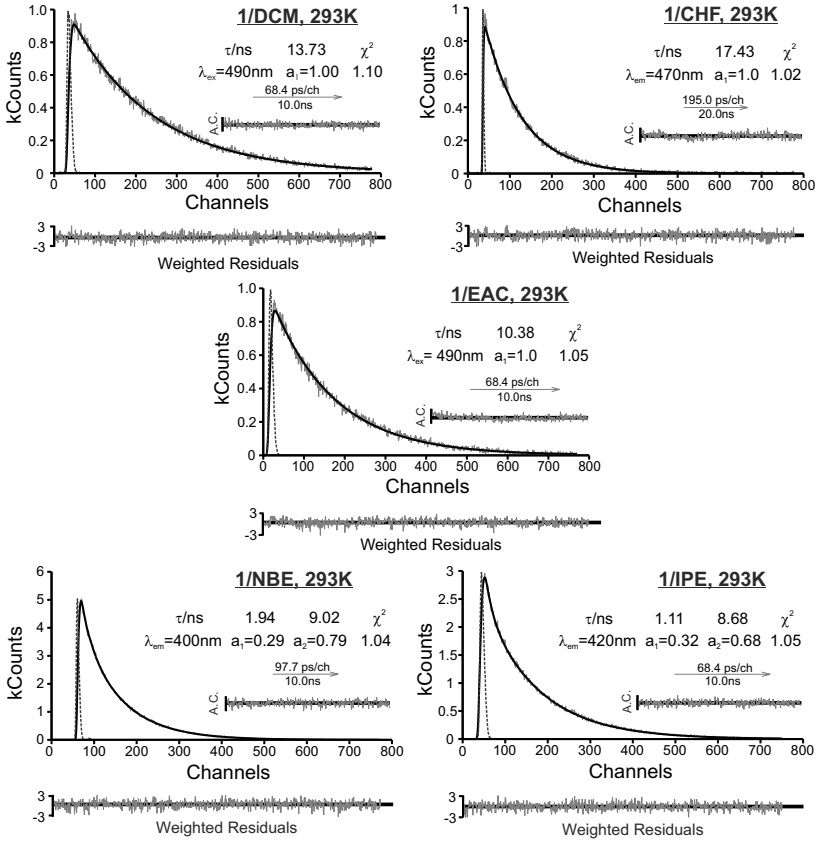

Figure 4.15 SPC decays of CT state of **1**, with applied monoexponential fitting in DCM, CHF and EAC and biexponential fitting in NBE and IPE ($\lambda_{ex} = 282\,\text{nm}$, 20°C).

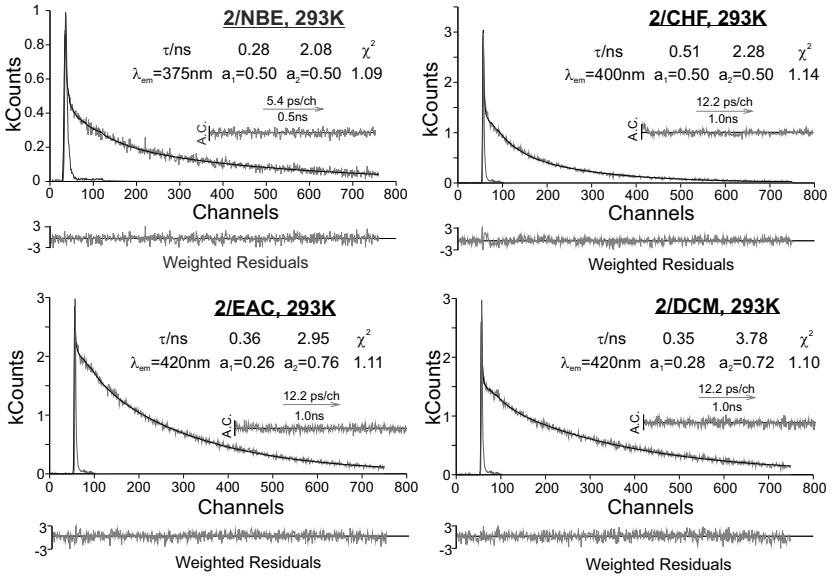

Figure 4.16 SPC decays of CT state of **2** with applied biexponential fitting in various solvents ($\lambda_{ex} = 273\,\text{nm}$, 20°C).

The mechanism in Figure 4.5 is analogous to that presented by Birks for excimer-exciplex decays and was solved to relate the rate constants to the lifetimes fitted to the SPC data. The difference is that in the Birks mechanism two monomers have to diffuse to yield the excimer and this is a bimolecular reaction, whereas in our mechanism intersystem crossing between singlet and triplet states of the CT species are first-order reactions. The important consequence of this difference is that the rate of the decay of the monomer in the Birks mechanism (corresponding to ${}^1k_{CR}$ in mechanism on Figure 4.17) can be obtained at high dilution of the monomer, when it becomes the only relevant decay of the monomer (corresponding to ${}^1CT$ in our mechanism), whereas in our mechanism there is no independent experimental measurement to obtain ${}^1k_{CR}$. As will be shown below, this can be circumvented with a reasonable estimate of the ratio between ${}^1k_{isc}$ and ${}^3k_{isc}$.

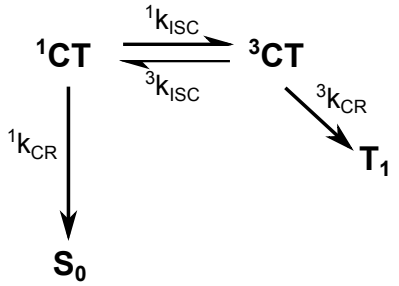

Figure 4.17 Modified Birks excimer mechanism used to treat bi-exponential SPC data.

The time evolution of ${}^1CT$ and ${}^3CT$ intensities can be obtained from differential equations

$$\frac{d\left[{}^1CT\right]}{dt} = {}^3k_{isc}\left[{}^3CT\right] - {}^1k_{isc}\left[{}^1CT\right] - {}^1k_{CR}\left[{}^1CT\right] \tag{4.1}$$

$$\frac{d\left[{}^3CT\right]}{dt} = {}^1k_{isc}\left[{}^1CT\right] - {}^3k_{isc}\left[{}^3CT\right] - {}^3k_{CR}\left[{}^3CT\right] \tag{4.2}$$

which are equivalent to that of the Birks mechanism

$$I_{1CT} = a_{11}e^{-\lambda_1 t} + a_{12}e^{-\lambda_2 t} = \frac{\left[{}^1CT\right]_0}{\lambda_2 - \lambda_1}\left\{(\lambda_2 - k_x)\,e^{-\lambda_1 t} + (k_x - \lambda_1)\,e^{-\lambda_2 t}\right\} \tag{4.3}$$

$$I_{3CT} = a_{21}e^{-\lambda_1 t} + a_{22}e^{-\lambda_2 t} = \frac{{}^1k_{isc}\left[{}^1CT\right]_0}{\lambda_2 - \lambda_1}\left(e^{-\lambda_1 t} - e^{-\lambda_2 t}\right) \tag{4.4}$$

where

$$\lambda_1 = \frac{1}{2}\left[(k_x + k_y) - \sqrt{(k_x - k_y)^2 + 4\,{}^1k_{isc}\,{}^3k_{isc}}\right] \tag{4.5}$$

$$\lambda_2 = \frac{1}{2}\left[(k_x + k_y) + \sqrt{(k_x - k_y)^2 + 4\,{}^1k_{isc}\,{}^3k_{isc}}\right] \tag{4.6}$$

with

$$k_x = {}^1k_{isc} + {}^1k_{CR} \tag{4.7}$$

$$k_y = {}^3k_{isc} + {}^3k_{CR} \tag{4.8}$$

and

$$\lambda_1\lambda_2 = k_x k_y - {}^1k_{isc}\,{}^3k_{isc} \tag{4.9}$$

$$\lambda_1 + \lambda_2 = k_x + k_y \tag{4.10}$$

Only the emission from ^1CT is observed. Hence, it can be used the relation

$$\frac{a_{11}}{a_{12}} = \frac{\lambda_2 - k_x}{k_x - \lambda_1} \tag{4.11}$$

to obtain

$$k_x = \frac{\lambda_1 a_{11} + \lambda_2 a_{12}}{a_{11} + a_{12}} - {}^1k_{CR} \tag{4.12}$$

Hence,

$${}^1k_{isc} = \frac{\lambda_1 a_{11} + \lambda_2 a_{12}}{a_{11} + a_{12}} \tag{4.13}$$

$${}^3k_{isc} = \frac{k_x\left(\lambda_1 + \lambda_2 - k_x\right) - \lambda_1\lambda_2}{{}^1k_{isc}} \tag{4.14}$$

$${}^3k_{CR} = \lambda_1 + \lambda_2 - k_x - {}^3k_{isc} \tag{4.15}$$

It is shown that $^1k_{CR}$, $^3k_{CR}$, $^1k_{isc}$ and $^3k_{isc}$ (Table 4.7) can be obtained from the SPC data knowing the singlet-triplet energy splitting. There are three degenerate ^3CT states with equal populations and each one of them intersystem crosses to the ^1CT state with the same rate $\left(^3k_{isc}/3\right)$. Including the statistical factor of 1/3 in the $^1k_{isc}$ /$^3k_{isc}$ ratio, if the energy of the ^1CT state is 0.3 kcal/mol above that of the ^3CT state, the singlet-triplet energy splitting required to calculate the micro-constants is $\Delta E_{ST} = 0.3$ kcal/mol. This is precisely the value calculated for singlet/triplet energy gap in CS states of rigid donor/acceptor systems separated by 5CC single bonds.[42]

Table 4.7 Micro-constants extracted from SPC data using the adapted Birks mechanism with ΔE_{ST}= 0.3 kcal/mol.

System	T (K)	$^1k_{CR}(s^{-1})$	$^3k_{isc}(s^{-1})$	$^1k_{isc}(s^{-1})$	$^3k_{CR}(s^{-1})$
	323	1.24×10^8	5.17×10^8	3.24×10^8	5.05×10^8
	308	9.32×10^7	3.50×10^8	2.14×10^8	2.90×10^8
	303	1.05×10^8	5.74×10^8	3.49×10^8	9.21×10^7
	293	8.66×10^7	2.38×10^8	1.42×10^8	1.60×10^8
	276	6.82×10^7	1.45×10^8	8.40×10^7	1.32×10^8
1/NBE	258	5.38×10^7	9.56×10^7	5.32×10^7	1.45×10^8
	253	3.81×10^7	1.62×10^8	8.93×10^7	1.22×10^8
	243	7.97×10^6	1.88×10^8	1.01×10^8	1.75×10^8
	238	2.82×10^7	8.66×10^7	4.59×10^7	8.90×10^7
	203	1.25×10^7	4.81×10^7	2.29×10^7	5.18×10^7
	193	1.28×10^7	2.86×10^7	1.31×10^7	3.53×10^7
1/IPE	293	8.20×10^7	4.59×10^8	2.74×10^8	1.77×10^8
2/NBE	293	8.38×10^8	2.00×10^9	1.19×10^9	2.05×10^7
	308	8.62×10^8	9.01×10^8	5.52×10^8	2.05×10^7
	293[a]	6.74×10^8	1.30×10^9	7.74×10^8	1.93×10^8
2/CHF	273	5.09×10^8	1.72×10^9	9.91×10^8	1.93×10^8
	238	4.22×10^8	2.71×10^9	1.44×10^9	7.04×10^7
	218	2.34×10^8	2.10×10^9	1.05×10^9	3.32×10^8
2/EAC	293[a]	1.20×10^8	1.52×10^9	9.07×10^8	7.50×10^8
	293[a]	1.25×10^8	1.57×10^9	9.35×10^9	5.37×10^8
	276	9.77×10^7	1.42×10^9	8.20×10^9	5.37×10^8
2/DCM	263	9.53×10^7	1.13×10^9	6.38×10^8	5.39×10^8
	243	7.58×10^7	1.36×10^9	7.28×10^8	5.63×10^8
	213	1.14×10^8	1.18×10^9	5.79×10^8	4.76×10^8
	188	1.48×10^8	1.25×10^9	5.58×10^8	3.94×10^8

[a] Average of three to six independent measurements

Table 4.8 Free energies and ET rate constants.

System	T (K)	ΔG^0_{CS} (kcal/mol)	$^1k_{CS}$ (s^{-1})	ΔG^0_{CR} (kcal/mol)	$^1k_{CR}$ (s^{-1})	$1/\tau_2$ (s^{-1})
	323	-11.4	1.22×10^{11}	-87.3	1.24×10^{8}	1.85×10^{8}
	308	-12.0	1.51×10^{11}	-86.7	9.32×10^{7}	1.24×10^{8}
	303	-12.2		-86.5	1.05×10^{8}	
	293	-12.7	1.19×10^{11}	-86.0	8.66×10^{7}	9.75×10^{7}
	276	-13.6	1.19×10^{11}	-85.1	6.82×10^{7}	7.00×10^{7}
1/NBE	258	-14.6		-84.0	5.38×10^{7}	
	253	-14.9	1.27×10^{11}	-83.7	3.81×10^{7}	5.60×10^{7}
	238	-15.8		-82.9	2.82×10^{7}	
	203	-17.8		-80.8	1.25×10^{7}	
	193	-18.4		-80.3	1.28×10^{7}	
1/IPE	293	-17.5	1.15×10^{11}	-81.2	8.20×10^{7}	1.06×10^{8}
	328	-17.6	2.52×10^{11a}	-81.1	5.99×10^{7}	9.80×10^{7a}
	318	-18.0		-80.6	5.99×10^{7}	
	308	-18.5		-80.2	5.65×10^{7}	
1/CHF	293	-19.2	1.52×10^{11}	-79.5	5.75×10^{7}	6.81×10^{7}
	276	-20.0	1.46×10^{11}	-78.7	6.58×10^{7}	7.24×10^{7}
	258	-20.7	1.26×10^{11b}	-77.9	7.69×10^{7}	7.54×10^{7b}
1/EAC	293	-21.7	1.22×10^{11}	-77.0	9.62×10^{7}	9.85×10^{7}
	293	-24.7	2.46×10^{11}	-74.0	7.30×10^{7}	7.24×10^{7}
	276	-25.1	2.53×10^{11}	-73.6	8.93×10^{7}	8.64×10^{7}
1/DCM	253	-25.7	2.30×10^{11}	-72.9	1.08×10^{8}	1.05×10^{8}
	223	-26.5	2.46×10^{11}	-72.2	1.19×10^{8}	1.06×10^{8}
	188	-27.3	2.00×10^{11}	-71.4	1.79×10^{8}	1.77×10^{8}
2/NBE	293	-0.4	2.16×10^{10}	-103.4	8.38×10^{8}	4.55×10^{9}
	308	-6.5		-97.3	8.62×10^{8}	
	293	-7.2	8.27×10^{10}	-96.6	$6.74\pm1.25\times10^{8c}$	1.00×10^{9}
2/CHF	273	-8.1		-95.6	5.09×10^{8}	
	238	-9.6		-94.1	4.22×10^{8}	
	218	-10.4		-93.3	2.34×10^{8}	
2/EAC	293	-9.8	2.55×10^{10}	-94.0	$1.20\pm0.27\times10^{8c}$	2.04×10^{8}
	293	-12.9	1.07×10^{11}	-90.8	$1.25\pm0.72\times10^{8c}$	1.44×10^{8}
	276	-13.4		-90.3	9.77×10^{7}	
	263	-13.8		-90.0	9.53×10^{7}	
2/DCM	243	-14.3		-89.4	7.58×10^{7}	
	213	-15.1		-88.6	1.14×10^{8}	
	188	-15.7		-88.0	1.48×10^{8}	

[a] At 323 K. [b] At 253 K. [c] Average and sample standard deviation of three to six independent measurements, representative of the error bars of rate constants obtained by single photon counting.

Table 4.8 shows that the $^1k_{CR}$ rate constants obtained from lifetimes of the single exponential decays measured by SPC, namely those of the systems **1**/CHF, **1**/EAC and **1**/DCM, are in excellent agreement with the reciprocal of **1** obtained by target analysis of transient spectra, with the possible exception of **1**/CHF at 323-328 K. Figure C.3 shows that at 323 K the transient absorption of **1**/CHF has a feature nearly absent at lower temperatures, which can be assigned to a complex formed between the anionic groups of $^1\mathbf{1}^{\pm}$ and a chlorine atom. This assignment is based on literature reports on similar species,[43] on the increase of the intensity of this feature with the removal of the stabilizer from the solvent, and on the decrease of this feature when the solvent is kept at lower temperatures.

The reciprocal of **2** is just slightly above the $^1k_{CR}$ rate constants obtained with the Birks mechanism and SPC data using $\Delta E_{ST} = 0.3$ kcal/mol (**1**/NBE, **1**/IPE and **2**), with the exception of **2**/NBE at 293 K. $^1\mathbf{2}^{\pm}$ in NBE has the lowest fluorescence emission (Figure 4.8) and a weak transient absorption spectrum, both contributing to larger errors in the measurement of $^1k_{CR}$. Additionally, the charge separation may not be totally irreversible in this system in view of its small exothermicity. Our best estimate is $^1k_{CR}$=$(2 \pm 1) \times 10^9\,\mathrm{s}^{-1}$ for **2**/NBE at 293 K, which is a remarkably high ET rate for a driving force $-\Delta G^0 = 103.4$ kcal/mol. This charge-recombination rate is many orders of magnitude faster than expected from conventional wisdom for an ET deep into the inverted region.

The SPC and transient absorption data are consistent with a ^1CT lifetime dominated by charge recombination ($^1k_{CR}$) but having other additional decay pathways. The values of $^1k_{isc}$ and $^3k_{isc}$ obtained for **1** using the modified Birks mechanism at room temperature are in the (1-5)$\times 10^8\,\mathrm{s}^{-1}$ range, consistent with the rates expected from the hfc-isc mechanism. The corresponding values for **2** are slightly larger, in the (1-2)$\times 10^9\,\mathrm{s}^{-1}$ range, possible due to the higher mixture of locally-excited state character in $\mathbf{2}^{\pm}$. Additionally, it can be seen that values of $^3k_{CR}$ and $^3k_{isc}$ in **1** are comparable, which makes population of $^3\mathbf{1}$ plausible. On the other hand, back intersystem crossing from $^3\mathbf{2}^{\pm}$ to $^1\mathbf{2}^{\pm}$ is faster than charge recombination to the $^3\mathbf{2}$.

It is tempting to assign the fast rates ($^1k_{CR}$>$10^8\,s^{-1}$) observed for ΔG^0< –75 kcal/mol to a change in mechanism. Hypothetically, an alternative decay pathway (e.g., intersystem crossing, fluorescence or photodecomposition) would become increasingly important in the less polar solvents and dominate the decay of ^1CT. We used flash photolysis to generate ^{3}**1** upon excitation of **1** at 266 nm in various solvents and compared ^{3}**1** with the triplet state of dMA under the same conditions (Figure 4.18). Flash photolysis of **1** in NBE generated a transient with a band at 330 nm and a lifetime of 2.0 ± 0.2 µs, that is quenched in the presence of oxygen, in good agreement with the triplet decay of anisole (τ_T=2.1 ± 0.2 µs, Φ_T=0.64).[36] We calculate Φ_T= 0.14 for **1** in NBE from the ratio of the initial decay intensities of ^{3}**1** and dMA, and assuming similar Φ_T for dMA and anisole. Attempts to see ^{3}**1** in DCM, EAC and CHF were unsuccessful, corroborating the estimates that $|\Delta G_{IP}|\leq E_{T1}$ in more polar solvents. We could not detect ^{3}**2** in the same experimental conditions. Decay to ^{3}**2** can be ruled out as a significant contributor to the decay of $\mathbf{2}^{\pm}$ because delayed fluorescence emission with microsecond lifetime is not observed. As mentioned before, the fluorescence of $^1\mathbf{2}^{\pm}$ is a small fraction of the fluorescence of oXy in NBE, which rules out the possibility of the radiative channel become the dominant decay channel of the CT species. The photostabilities of **1** and **2** were checked measuring their absorption spectra before and after the laser experiments and no relevant absorption changes were observed.

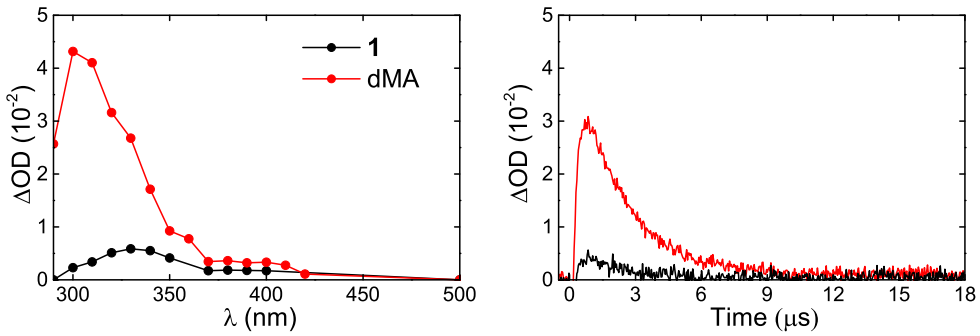

Figure 4.18 Triplet state spectrum of dMA and **1** in di-n-butyl ether. Left: time-resolved transient absorption spectra upon excitation at 266 nm. Right: triplet decays profiles of dMA at 300 nm (red) and **1** at 330 nm (black) in the absence of oxygen.

The temperature dependence of ${}^1k_{CR}$ provides further insight into the end of the inverted region at $\Delta G^0 \approx -75$ kcal/mol. ET rates in the inverted region are believed to be essentially temperature independent,[44–46] but negative effective activation energies may be observed in intramolecular charge recombination reactions when the dielectric constant of the solvent decreases as the temperature is increased or when a state favorable for ET is depopulated with an increase in temperature.[47] The temperature dependence of charge recombination in an intramolecular D–A systems was recently shown to exhibit an inverted parabola dependence on $1/T$, and this was presented as the "cleanest confirmation" of the Marcus energy gap law.[48] The bell-shaped Arrhenius law was assigned to the temperature dependence of the solvation free energies.

Table 4.8 shows that ${}^1k_{CR}$ and $1/\tau_2$ of ${}^1\mathbf{1}^{\pm}$ in DCM decrease when the temperature increases, and lead to $E_a = -0.86 \pm 0.10$ kcal/mol. This negative activation of an elementary reaction can be assigned to the change in the exothermicity of the charge recombination, from –74.0 to –71.4 kcal/mol, associated with the increase of ε from 9.0 at 293 K to 15.5 at 187 K (Table C.1). These changes in temperature also lead to a strong thermochromic CT fluorescence (Figure 4.10), further corroborating the change of ΔG_0 with T. The more exothermic reaction, at the higher temperature, is slower because it takes place in the inverted region. On the other hand, ${}^1k_{CR}$ and $1/\tau_2$ of ${}^1\mathbf{1}^{\pm}$ in NBE increase when the temperature increases, and lead to $E_a = 2.32 \pm 0.12$ kcal/mol. The same activationless behavior is expected for charge recombinations of ${}^1\mathbf{1}^{\pm}$ in DCM and in NBE. Hence, the change from $E_a < 0$ for $\Delta G^0 > -75$ kcal/mol to $E_a > 0$ for $\Delta G^0 < -75$ kcal/mol is compelling evidence that the increase of ET rates observed for very exothermic reactions is indeed intrinsic to their free-energy dependence and not the result of a change in mechanism. The most exothermic charge recombinations in NBE take place at higher temperatures and are faster. The charge recombinations of ${}^1\mathbf{1}^{\pm}$ in CHF cover the range of ΔG^0 from –77.9 to –81.1 kcal/mol and are practically activationless, as they occur at the end of the inverted region. Figure 4.19 presents the Arrhenius plots of these sys-

tems. The change from negative to positive apparent activation energies takes place at $\Delta G^0 \approx -75\,\text{kcal/mol}$, where the exothermic rate restrictions predicted by Marcus theory are lifted for these systems.

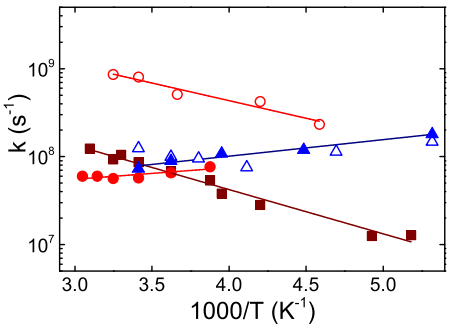

Figure 4.19 Charge recombination as a function of temperature dependence of **1** (full symbols) and **2** (open symbols) in NBE (squares), CHF (circles) and DCM (triangles).

The shorter fluorescence decay of $^1\mathbf{2}^{\pm}$ at higher temperatures in CHF leads to the extraordinary observation that charge recombination is faster in $^1\mathbf{2}^{\pm}$ than in $^1\mathbf{1}^{\pm}$ ($6.7 \times 10^8\,\text{s}^{-1}$ vs. $5.8 \times 10^7\,\text{s}^{-1}$ at 293 K) in CHF but $E_a = 1.83 \pm 0.25\,\text{kcal/mol}$ for $^1\mathbf{2}^{\pm}$ and $E_a = -0.61 \pm 0.20\,\text{kcal/mol}$ for $^1\mathbf{1}^{\pm}$. This is an unprecedented case of elementary reactions following the same mechanism where the reaction with an apparent energy barrier is one order of magnitude faster than the barrierless reaction. Figure 4.20 plots $^1k_{CR}$ as a function of ΔG^0 using the dielectric constant dependence on the temperature to show that a significant part of the temperature dependence observed can be assigned to the dependence of ε on T.

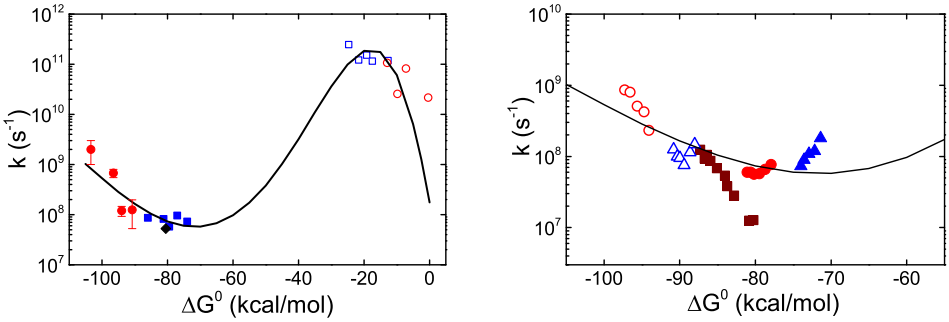

Figure 4.20 Left: Charge separation (open symbols) and charge recombination (closed symbols) in **1** (blue squares) and **2** (red circles) obtained in this work, and charge recombination in **1** in diethyl ether (♦)[1] as a function of the driving force at 293K. Right: Charge recombination of **1** (full symbols) and **2** (open symbols) as a function of the driving force at various temperatures in NBE (squares), CHF (circles) and DCM (triangles).

It must be emphasized that the new free-energy relationship shown in Figure 4.20 is not biased by mechanistic interpretations of the kinetic data. The target analysis of the transient absorption and the modified Birks kinetic scheme employed to interpret the fluorescence decays are required to obtain the proper micro-constants, but the essential features of the end of the inverted region are already present in the raw data. Figure 4.21 shows the kinetic traces of the transient absorption at 470 nm, where the aromatic radical cation absorbs. It is clear that the lifetimes of $^1\mathbf{2}^{\pm}$ in the various solvents follow the order $\tau_{DCM} > \tau_{EAC} > \tau_{CHF} > \tau_{NBE}$, i.e., the fastest decay corresponds to the less polar solvent and most exothermic reaction, precisely the opposite of the prediction of Marcus theory.

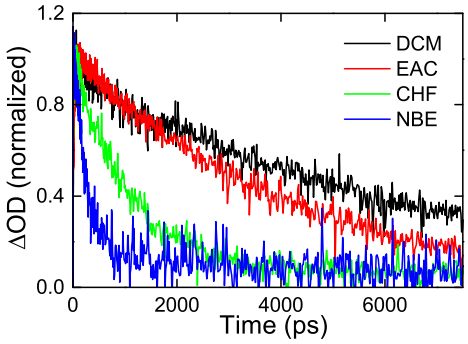

Figure 4.21 Decays of $^1\mathbf{2}^{\pm}$ at 470 nm in the solvents indicated in the plot. The solvent response was subtracted from decays and the chirp correction was made according to Surface Xplorer, and then the decays were normalized by the maximum absorption change, to be plotted together.

Figure 4.22 shows the fluorescence decays of $^1\mathbf{1}^{\pm}$ in DCM and in NBE that illustrate the increase lifetime with the temperature in the first system and the decrease in the latter one, which are the basis for the change from negative to positive activation energies at the end of the inverted region. This figure also presents the fluorescence decays of $^1\mathbf{1}^{\pm}$ and $^1\mathbf{2}^{\pm}$ in CHF, which allow us to appreciate the same phenomenon when the molecules, rather than the solvents, are changed.

The ET rate constants plotted in Figure 4.20 challenge the established view of ET reactions: Marcus inverted region ends at –75 kcal/mol, the activation energy changes from negative to positive at this driving force, all moderately polar solvents

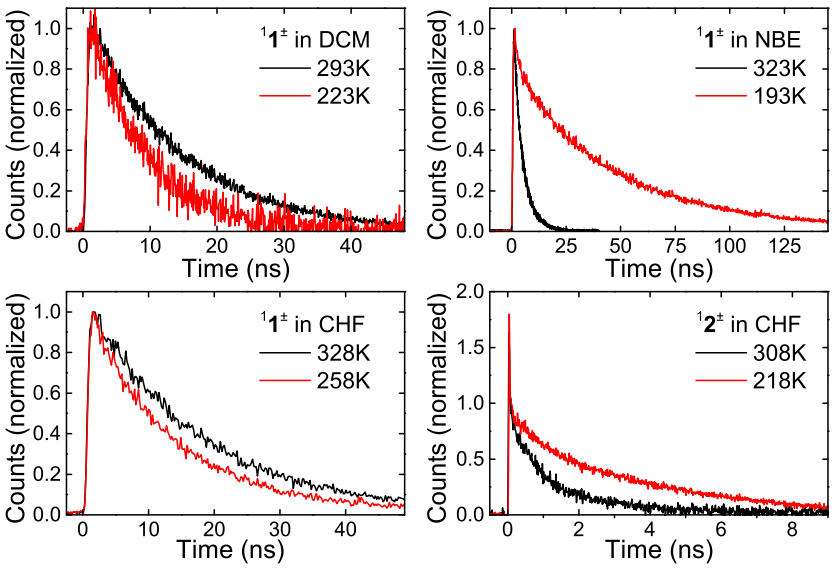

Figure 4.22 Fluorescence decays at various temperatures of $^1\mathbf{1}^{\pm}$ in di-n-butyl ether, $^1\mathbf{1}^{\pm}$ in dichloromethane and $^1\mathbf{1}^{\pm}$ in chloroform normalized at maximum, and $^1\mathbf{2}^{\pm}$ in chloroform normalized at 100 ps.

fit the same free-energy dependence, and the less polar solvents (ethers) do not have the lowest rates of the inverted region. For example, $^1k_{CR}$ increases from 8.7×10^7 s^{-1} for $^1\mathbf{1}^{\pm}$ (ΔG^0= –86 kcal/mol) to 8.4×10^8 s^{-1} for $^1\mathbf{2}^{\pm}$ (ΔG^0= –103 kcal/mol) in NBE, and decreases to 1.4×10^8 s^{-1} for $^1\mathbf{2}^{\pm}$ in DCM (ΔG^0= –91 kcal/mol). As shown above, this new behavior cannot be assigned to a change in mechanism, namely to the predominance of $^3\mathbf{1}^{\pm} \rightarrow {}^3\mathbf{1}$ charge recombinations when the exothermicity of $^1\mathbf{1}^{\pm} \rightarrow {}^1\mathbf{1}$ exceeds –75 kcal/mol, because that should lead to a large Φ_T and Figure 4.18 shows that $\Phi_T < 0.14$.

ET rates are often expressed as the product between the donor-acceptor electronic coupling strength (V) and a Franck-Condon weighted density of states ($FCWD$)

$$k = \frac{2\pi}{\hbar}\left|V^2\right| FCWD \tag{4.16}$$

where V is related to the probability of electron tunneling from donor to acceptor in the activated complex. The temperature independence of very exothermic ETs is appropriately described by the quantum-mechanical expression of $FCWD$[49–51]

$$FCWD = \frac{1}{\sqrt{4\pi\lambda_s k_B T}} \sum_{n=0}^{\infty} e^{-S} \frac{S^n}{n!} exp\left[-\frac{\left(\Delta G^0 + \lambda_s + n\hbar\omega_v\right)^2}{4\lambda_s k_B T}\right] \tag{4.17}$$

where the high frequency vibrations are treated as a single high frequency vibrational mode ($h\omega$) with a reduced displacement $S = \lambda_v/\hbar\omega_v$. This expression proved very valuable to interpret ET reactions in the inverted region using values of V, λ_s, λ_v and $\hbar\omega_v$ from various sources. A possible limitation of this approach to very exothermic ET reactions is the neglect of anharmonicity in the intramolecular modes. A significantly flatter dependence on exoergicity is predicted for the maximum rates using anharmonic modes,[52] but for very exothermic reactions the steep decrease of the rates with the exoergicity is maintained and does not explain the lifting of exothermic rate restrictions. Another possible limitation is that vibrational frequencies $\hbar\omega_\nu$=1500 cm^{-1} are often used to represent aromatic donors and acceptors,[22] but the coupling to very high frequency modes (e.g., $\hbar\omega_v$= 3000 cm^{-1} C–H vibration) could increase $FCWD$ at very high driving forces.[53] Although it may be expected that very high frequency modes play an increasingly important role as the exoergicity of the reactions increases, even considering their small reduced displacements, a criterion to add progressively more contributions of the very high frequency modes is necessary to reproduce the increase of $^1k_{CR}$ for ΔG^0< -75 kcal/mol, and this criterion is not known.

Another challenge with eq. 4.17 is the selection of the adequate solvent reorganization energy for the calculations. According to eq. 1.26 proposed by Marcus, the values of λ_s for molecule **2** range from 11 kcal/mol in n-butyl ether to 22 kcal/mol in dichloromethane. It is increasingly clear that the dielectric continuum approximation overestimates λ_s,[54] probably by a factor of two.[55–57] Li presented a correction for calculation of λ_s, by using the constrained equilibrium principle (eq. 1.27)[57] that lowers the estimates to 3 and 9 kcal/mol for n-butyl ether and dichloromethane, respectively. These calculations suggest λ_s= 6±3 kcal/mol for our weakly and moderately polar solvents. The fastest rates, which should correspond to $-\Delta G^0 = \lambda$,

were observed for the charge separations with $\Delta G^0 \approx -20\,\text{kcal/mol}$, which indicates that the major contribution to $FCWD$ originates from high-frequency molecular vibrations corresponding to the electron donor and electron acceptor centers. This is further corroborated by the observation that the ET rates of **1** measured in deuterated chloroform were indistinguishable from the rates in CHF. In view of the dominance of the high-frequency modes and of the barrierless rates observed, we pursue below an interpretation of ET rates in **1** and **2** as radiationless transitions in large molecules. The Section 1.5.3 show that ET rates can be described as nuclear tunneling of promoting and accepting modes of effective mass μ_{DA}[58,59]

$$k = \nu exp\left[-\frac{\Delta x\sqrt{2\mu_{DA}\Delta E^{\ddagger}}}{\hbar}\right] \tag{4.18}$$

where ν is the reaction frequency, and Δx and $\Delta E^{\ddagger}$ are represented in Figure 4.23.

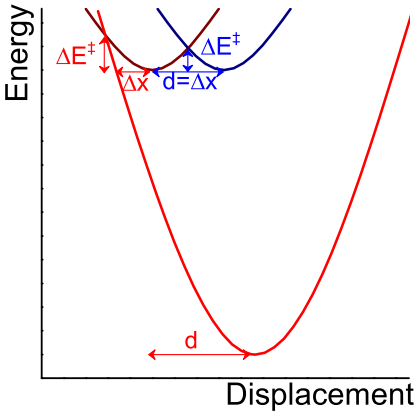

Figure 4.23 ET coordinate using a single mode approximation illustrating the tunneling barrier width (Δx) and height $\left(\Delta E^{\ddagger}\right)$, and increase of d with ΔG^0 given by ISM.

The nonadiabatic multiphonon formalism leads to an equation analogous to eq. 4.18 when the contribution of the solvent is neglected and the nuclear distortions are described by an averaged single mode.[60] In fact, eq. 4.18 is a particular case of the WKB approximation for nuclear tunneling through a barrier formed by intersecting parabolas with their minima separated by a displacement d. The reaction frequency ν is related to the electronic coupling between initial and final states, V. When the donor and acceptor are separated by a long spacer, the electronic frequency in

the donor must be multiplied by the electron tunneling probability to obtain the reaction frequency, $\nu = \nu_{el}\chi$, where $\chi = exp(-r_c\beta)$. Representing the spacer by a square energy barrier with the optical dielectric constant ε_{op} ($\varepsilon_{op} = n_D^2$, $n_D \approx 1.4$ on the basis of cyclohexane), and using $\nu_{el} \approx 5 \times 10^{14}\,\mathrm{s}^{-1}$ for the aromatic donor,[61] we calculated $\beta = 1.27\,\text{Å}^{-1}$ (from eq. 1.6) and $\nu \approx 2 \times 10^{11}\,\mathrm{s}^{-1}$.

In view of the relations between Δx, ΔG^0, d and the force constant of the high frequency vibrational mode (f), shown in Figure 4.23 and discussed in Section 1.5.3, the calculation of the ET rate constant using eq. 4.18 requires the displacement d and the effective reduced mass μ_{DA}. This latter parameter is obtained from the reduced masses of the oscillators involved in the radiationless transitions. For the case of **1** and **2**, one of the moieties can be approximated as the benzene ring and the other as dicyanoethylene. We have shown before that the average of the force constants of the relevant oscillators gives $f_{CC} \approx 1.15 \times 10^3\,\mathrm{kcal/(mol\,Å^2)}$, and that the effective reduced masses are $\mu_{benzene}=3\mu_{CC}$, $\mu_{dicyanoethylene}=\mu_{CC}+2\mu_{CN}$,[46,62–64] what give $\mu_{donor} = 19\,\mathrm{amu}$ and $\mu_{acceptor} = 18\,\mathrm{amu}$. When the donor and acceptor modes are described by the averaged single mode, the displacement d is estimated as the square root of the mean squared displacements,[58,65,66] which yields to $d = 0.164\,\text{Å}$ for charge separation and $d = 0.162$ Å for charge recombination reactions.

Alternatively, in this work, we estimated d using the Intersecting-State Model. According to ISM, the total displacement for an averaged single mode of equilibrium bond length l_{eq} is given by[54]

$$d = \frac{a'}{2n^{\ddagger}} ln\left[\frac{1+g}{1-1/(1+g)}\right](l_{r,eq} + l_{p,eq}), \qquad g = exp\left(\sqrt{2n^{\ddagger}}\Delta G^0/\Lambda\right) \tag{4.19}$$

where $a' = 0.156$ is a scaling constant and $n^{\ddagger}$ is the averaged bond order. When $\Delta G^0 = 0$, d is independent of Λ and averaging the values of the aromatic and dicyanoethene moieties ($n^{\ddagger} = 1.75$, $l_{eq} = 1.37\,\text{Å}$, $f = 1.14 \times 10^3\,\mathrm{kcal\,mol^{-1}\,Å^{-2}}$),[46,62,64] we obtain $d = 0.169\,\text{Å}$. This is in good agreement with the square root of the mean squared displacements calculated by GAMESS and yields an intrinsic barrier $\Delta G_0^{\ddagger} = \lambda/4 \approx 4\,\mathrm{kcal/mol}$. The nuclear tunneling rate constants calculated with eq. 4.18

employed Δx calculated with eqs. 1.49-1.52, effective reduced masses calculated with eq. 1.44 and $\nu \approx 2\times10^{11}\,\mathrm{s}^{-1}$. The tunneling rates are larger that thermal activation rates calculated over the same energy barrier with eq. 1.54 for $\Delta G^0 <$ -20 kcal/mol. However, thermal activation dominates the rates in the normal region. Figure 4.20 combines the thermal activates in the normal region with the tunneling rates elsewhere.

The interesting feature of ISM is that, for finite values of Λ, d increases with $|\Delta G^0|$, i.e., the reorganization energy increases with the driving force of the reaction. This increase is associated with the disposal of the reaction energy in otherwise spectator modes when a large amount of energy must be dissipated. The coupling parameter Λ, regulating the disposal of excess reaction energy, is the only parameter of ISM that is not calculated from molecular properties. Figure 4.20 shows that eqs. 4.18 and 4.19 with parameters typical of aromatic and dicyanoethene modes and Λ=70 kcal/mol, used for similar systems,[62,64] describe remarkably well the driving force and the temperature dependencies of ET rates. A more refined description of the temperature dependence should also consider that the contributions of the high-frequency modes may change with the temperature. Rather than adding an extra layer of complexity to the theory, at this point we wish to emphasize that the transition to positive activation energies occurs at the driving force of the beggining of the new "normal" region.

The ability to describe the new free-energy dependence disclosed in this work comes from the increase of the reorganization energy with the driving force embedded in ISM. Admittedly, the remarkable agreement obtained may benefit from some compensation between the neglect of λ_s, the method to obtain d and the value of Λ selected for the calculations. More than emphasizing a quantitative agreement between calculated and experimental rates, which is favored by the choice of the parameters employed, it must be stressed that it is possible to model the end of the inverted region when λ increases with $|\Delta G^0|$.

4.3 Conclusions

The dogma of chemical reactivity is that, for elementary reactions following the same mechanism, higher energy barriers lead to slower reactions. We observed faster ET rates with higher activation energies. This paradox is solved realizing that higher temperatures decrease ε and increase charge recombination exothermicities, which increase their reorganization energies. Established ET theories need to be revised to accommodate the increase of λ with $|\Delta G^0|$ and the end of Marcus inverted region. The ability to describe these phenomena with a tunneling model and d given by ISM, suggests that the reaction energy is increasingly dissipated to accepting very high-frequency modes, not covered by the frontier molecular orbitals, as the reactions become more exothermic. The contribution of these additional modes increases the reorganization energy with the driving force. The coupling of reactive modes to otherwise spectator modes suggests that the lifetimes of high-energy charge-separated states in molecular electronics and photovoltaic cells can be lengthened, and the efficiencies improved, uncoupling donor and acceptor moieties from spectator modes. The local mode behavior of such modes should decrease charge recombination rates of very exothermic ET.

4.4 Summary and Future Direction

This chapter presented the first studies of ultraexothermic reactions, which could be performed due to the proper choice of donor and acceptor groups. Studies on intramolecular systems, where the donor and acceptor are held at fixed distance, allows a better characterization of the processes occurring before and after electron transfer. We were able to probe very fast charge separation processes (4-50 ps), that would not be possible in the bimolecular system, due to the diffusion-limited kinetics.

Molecules **1** and **2** have been examined in several solvents of varying dielectric properties (ε=2.8-16) and temperatures (288-328K), giving charge recombination

rates following the same free-energy relationship, and allowing us to observe a new "double-inverted region". These findings may be explained by the dominant role of the intramolecular high-frequency modes, rather than solvent dynamic motions.

Of future interest are studies in polar solvents. With such studies, it would be possible to find out if the rate vs free-energy dependence has the same behavior as in low and moderate polarity solvents.

References

1. P. Pasman, G. F. Mes, N. W. Koper and J. W. Verhoeven, *J. Am. Chem. Soc.*, 1985, **107**, 5839–5843.

2. H. Morrison, *Acc. Chem. Res.*, 1979, **12**, 383–389.

3. J. R. Winkler and H. B. Gray, *J. Am. Chem. Soc.*, 2014, **136**, 2930–2939.

4. N. P. Co, R. M. Young, A. L. Smeigh, M. R. Wasielewski and B. M. Hoffman, *J. Am. Chem. Soc.*, 2014, **136**, 12730–12736.

5. S. E. Canton, K. S. Kjær, G. Vankó, T. B. van Driel, S.-I. Adachi, A. Bordage, C. Bressler, P. Chabera, M. Christensen, A. O. Dohn, A. Galler, W. Gawelda, D. Gosztola, K. Haldrup, T. Harlang, Y. Liu, K. B. Møller, Z. Németh, S. Nozawa, M. Pápai, T. Sato, T. Sato, K. Suarez-Alcantara, T. Togashi, K. Tono, J. Uhlig, D. A. Vithanage, K. Wärnmark, M. Yabashi, J. Zhang, V. Sundström and M. M. Nielsen, *Nat. Commun.*, 2015, **6**, 6359.

6. R. A. Marcus, *J. Chem. Phys.*, 1956, **24**, 966–978.

7. R. A. Marcus, *Discuss. Faraday Soc.*, 1960, **29**, 21–31.

8. L. T. Calcaterra, G. L. Closs and J. R. Miller, *J. Am. Chem. Soc.*, 1983, **105**, 670–671.

9. H. Oevering, M. N. Paddon-Row, M. Heppener, A. M. O. Oliver, E. Cotsaris, J. W. Verhoeven and N. S. Hush, *J. Am. Chem. Soc.*, 1987, **109**, 3258–3269.

10. A. Rao, P. C. Y. Chow, S. Gélinas, C. W. Schlenker, C.-z. Li, H.-L. Yip, A. K. Jen, D. S. Ginger and R. H. Friend, *Nature*, 2013, **500**, 435–440.

11. W. Chang, D. N. Congreve, E. Hontz, M. E. Bahlke, D. P. McMahon, S. Reineke, T. C. Wu, V. Bulović, T. Van Voorhis and M. a. Baldo, *Nat. Commun.*, 2015, **6**, 6415.

12. R. Ihly, K. S. Mistry, A. J. Ferguson, T. T. Clikeman, B. W. Larson, O. Reid, O. V. Boltalina, S. H. Strauss, G. Rumbles and J. L. Blackburn, *Nat. Chem.*, 2016, **8**, 603–609.

13. K. H. Hendriks, A. S. G. Wijpkema, J. J. van Franeker, M. M. Wienk and R. a. J. Janssen, *J. Am. Chem. Soc.*, 2016, **138**, 10026–10031.

14. X. Zhang, Y. Xu, F. Giordano, M. Schreier, N. Pellet, Y. Hu, C. Yi, N. Robertson, J. Hua, S. M. Zakeeruddin, H. Tian and M. Grätzel, *J. Am. Chem. Soc.*, 2016, **138**, 10742–10745.

15. T. Higashino, T. Yamada, M. Yamamoto, A. Furube, N. V. Tkachenko, T. Miura, Y. Kobori, R. Jono, K. Yamashita and H. Imahori, *Angew. Chemie - Int. Ed.*, 2016, **55**, 629–633.

16. H. Uoyama, K. Goushi, K. Shizu, H. Nomura and C. Adachi, *Nature*, 2012, **492**, 234–238.

17. M. Barroso, A. J. Cowan, S. R. Pendlebury, M. Grätzel, D. R. Klug and J. R. Durrant, *J. Am. Chem. Soc.*, 2011, **133**, 14868–14871.

18. S. Berardi, G. La Ganga, M. Natali, I. Bazzan, F. Puntoriero, A. Sartorel, F. Scandola, S. Campagna and M. Bonchio, *J. Am. Chem. Soc.*, 2012, **134**, 11104–11107.

19. M. Barroso, S. R. Pendlebury, A. J. Cowan and J. R. Durrant, *Chem. Sci.*, 2013, **4**, 2724–2734.

20. C. Schubert, J. . T. Margraf, T. Clark and D. M. Guldi, *Chem. Soc. Rev.*, 2015, **44**, 988–998.

21. M. Mollahosseini, E. Karunaratne, G. N. Gibson, J. A. Gascón and F. Papadimitrakopoulos, *J. Am. Chem. Soc.*, 2016, **138**, 5904–5915.

22. G. L. Closs and J. R. Miller, *Science*, 1988, **240**, 440–447.

23. J. Sukegawa, C. Schubert, X. Zhu, H. Tsuji, D. M. Guldi and E. Nakamura, *Nat. Chem.*, 2014, **6**, 899–905.

24. X. Gong, R. M. Young, K. J. Hartlieb, C. Miller, Y. Wu, H. Xiao, P. Li, N. Hafezi, J. Zhou, L. Ma, T. Cheng, W. A. Goddard, O. K. Farha, J. T. Hupp, M. R. Wasielewski and J. F. Stoddart, *J. Am. Chem. Soc.*, 2017, **139**, 4107–4116.

25. D. M. E. Freeman, A. J. Musser, J. M. Frost, H. L. Stern, A. K. Forster, K. J. Fallon, A. G. Rapidis, F. Cacialli, I. Mcculloch, T. M. Clarke, R. H. Friend and H. Bronstein, *J. Am. Chem. Soc.*, 2017, **139**, Just accepted.

26. A. F. Brigas and R. A. Johnstone, *Tetrahedron Lett.*, 1990, **31**, 5789.

27. J. M. Lawson, D. C. Craig, A. M. Oliver and M. N. Paddon-Row, *Tetrahedron*, 1995, **51**, 3841.

28. M. W. Schmidt, K. K. Baldridge, J. A. Boatz, S. T. Elbert, M. S. Gordon, J. H. Jensen, S. Koseki, N. Matsunaga, K. A. Nguyen, S. Su, T. L. Windus, M. Dupuis and J. A. Montgomery, *J. Comput. Chem.*, 1993, **14**, 1347–1363.

29. A. D. Becke, *J. Chem. Phys.*, 1993, **98**, 5648–5652.

30. P. J. Stephens, F. J. Devlin, C. F. Chabalowski and M. J. Frisch, *J. Phys. Chem.*, 1995, **98**, 11623–11627.

31. R. H. Hertwig and W. Koch, *Chem. Phys. Lett.*, 1997, **268**, 345–351.

32. R. Ditchfield, W. J. Hehre and J. A. Pople, *J. Chem. Phys.*, 1971, **54**, 724–728.

33. A. Weller, H. Staerk and R. Treichel, *Faraday Discuss. Chem. Soc.*, 1984, **78**, 271–278.

34. I. V. Khudyakov, Y. A. Serebrennikov and N. J. Turro, *Chem. Rev.*, 1993, **93**, 537–570.

35. Z. E. X. Dance, S. M. Mickley, T. M. Wilson, A. B. Ricks, A. M. Scott, M. A. Ratner and M. R. Wasielewski, *J. Phys. Chem. A*, 2008, **112**, 4194–4201.

36. M. Montalti, L. Prodi, A. Credi and M. T. Gandolfi, *Handbook of Photochemistry*, CRC Press, 3rd edn, 2006.

37. A. Zweig, W. G. Hodgson and W. H. Jura, *J. Am. Chem. Soc.*, 1964, **86**, 4124–4129.

38. P. B. Merkel, P. Luo, J. P. Dinnocenzo and S. Farid, *J. Org. Chem.*, 2009, **74**, 5163–5173.

39. A. Weller, *Zeitschrift für Phys. Chemie*, 1982, **133**, 93–98.

40. P. Pasman, J. W. Verhoeven and T. J. de Boer, *Chem. Phys. Lett.*, 1978, **59**, 381–385.

41. S. Takamuku, S. Komitsu and S. Toki, *Radiatiation Phys. Chem.*, 1989, **34**, 553–559.

42. M. N. Paddon-Row and M. J. Shephard, *J. Phys. Chem. A*, 2002, **106**, 2935–2944.

43. A. C. Crowther, S. L. Carrier, T. J. Preston and F. F. Crim, *J. Phys. Chem. A*, 2008, **112**, 12081–12089.

44. N. Liang, J. R. Miller and G. L. Closs, *J. Am. Chem. Soc.*, 1990, **112**, 5353–5354.

45. J. Kroon, H. Oevering, J. W. Verhoeven, J. M. Warman, A. M. Oliver and M. N. Paddon-Row, *J. Phys. Chem.*, 1993, **97**, 5065–5069.

46. C. Serpa, P. J. S. Gomes, L. G. Arnaut, J. S. De Melo and S. J. Formosinho, *Chemphyschem*, 2006, **7**, 2533–2539.

47. A. M. Scott and M. R. Wasielewski, *J. Am. Chem. Soc.*, 2011, **133**, 3005–3013.

48. M. M. Waskasi, G. Kodis, A. L. Moore, T. A. Moore and D. V. Matyushov, *J. Am. Chem. Soc.*, 2016, **138**, 9251–9257.

49. M. Bixon and J. Jortner, *J. Phys. Chem.*, 1991, **95**, 1941–1944.

50. R. A. Marcus and P. Siddarth, *Photoprocesses Transit. Met. Complexes, Biosyst. Other Mol. Exp. Theory*, NATO ASI Series, Kluwer: Dordrecht, 1992, p. 49.

51. L. G. Arnaut, S. J. Formosinho and H. D. Burrows, *Chemical Kinetics*, Elsevier, Amsterdam, 2007.

52. S. Yeganeh and M. A. Ratner, *J. Chem. Phys.*, 2006, **124**, 044108.

53. M. Bixon, J. Jortner, J. Cortes, H. Heitele and M. E. Michel-Beyerle, *J. Phys. Chem.*, 1994, **98**, 7289–7299.

54. S. J. Formosinho, L. G. Arnaut and R. Fausto, *Prog. React. Kinet.*, 1998, **23**, 1–90.

55. M. D. Newton, M. V. Basilevsky and I. V. Rostov, *Chem. Phys.*, 1998, **232**, 201–210.

56. H.-S. Ren, M.-J. Ming, J.-Y. Ma and X.-Y. Li, *J. Phys. Chem. A*, 2013, **117**, 8017–8025.

57. X.-Y. Li, *Int. J. Quantum Chem.*, 2015, **115**, 700–721.

58. S. J. Formosinho, *J. Chem. Soc. Faraday Trans. II*, 1974, **70**, 605–620.

59. S. J. Formosinho and L. G. Arnaut, *Adv. Photochem.*, 1991, **16**, 67.

60. J. Jortner and J. Ulstrup, *Chem. Phys. Lett.*, 1979, **63**, 236–239.

61. S. J. Formosinho and L. G. Arnaut, *Bull. Chem. Soc. Jpn.*, 1997, **70**, 977.

62. C. Serpa, P. J. S. Gomes, L. G. Arnaut, S. J. Formosinho, J. Pina and J. S. De Melo, *Chem. - A Eur. J.*, 2006, **12**, 5014–5023.

63. P. J. S. Gomes, C. Serpa, R. M. D. Nunes, L. G. Arnaut and S. J. Formosinho, *J. Phys. Chem. A*, 2010, **114**, 2778–2787.

64. K. K. Mentel, R. M. D. Nunes, C. Serpa and L. G. Arnaut, *J. Phys. Chem. B*, 2015, **119**, 7571–7578.

65. E. F. McCoy and I. G. Ross, *Aust. J. Chem.*, 1962, **15**, 573–590.

66. R. P. van Duyne and S. F. Fischer, *Chem. Phys.*, 1974, **5**, 183–197.

5 Electron Transfer Reactions in Polar Solvents

5.1 Introduction

It was shown before that intramolecular systems help to probe the charge separation and charge recombination kinetics in various middle polarity solvents. Here, we will address the question if the CS and CR rates in polar solvents follow the same free-energy dependence as in less polar solvents.

According to the eq. 1.16, it is clear that an increase in the solvent polarity is going to affect the Coulomic stabilization and solvation terms. Thus, the charge recombination becomes less exothermic than in the weakly polar solvents. It is well known that the dynamics of solvation plays an important role when the charge-transfer state is formed. It was pointed out that the interaction energy of polar solvents with the charged species is similar to chemical binding energies.[1] The polar solvents can affects the electronic nature of the CT, for example, by amplifying its charge-transfer character. Additionally, the electronic deformations in the solvated molecule may by followed by structural changes which are not observed in the gas phase or in middle polarity solvents. Increasing the solvent polarity also increases the solvent reorganization energy.

In this chapter, we will focus on the influence of polar solvents on the ET rates, using the same intramolecular systems and bimolecular dMA+iPN system as in chapter 4.

5.2 Results and Discussion

5.2.1 Steady-State Study

The absorption spectrum of **1** and the sum spectra of 3,4-dimethylanisole (dMA) and isopropylidenomalononitrile (iPN), measured in acetonitrile, are presented in Figure 5.1. The maximum of the lowest locally-excited electronic state of **1** was red shifted ~ 3.5 nm in comparison with the parent compounds, and shifted around 0.5 nm to the higher energy, comparatively to the middle polarity solvents. Figure 5.1 also presents the absorption spectrum of **2**, with a shoulder between 270 and 278 nm, which was assigned to the lowest locally-excited electronic state of **2** after comparison with the respective fluorescence excitation spectrum.

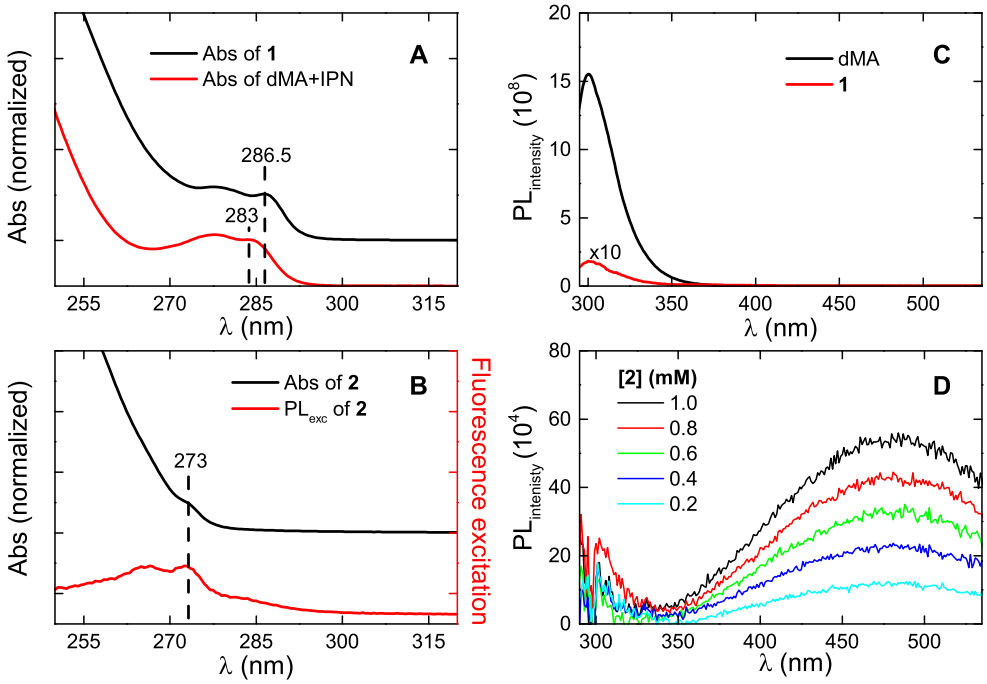

Figure 5.1 (A) Absorption spectrum of **1** in comparison with the sum spectra of dMA and iPN (0.1mM each). (B) Absorption and fluorescence excitation ($\lambda_{em} = 480$ nm) spectra of **2**. (C) Fluorescence spectra of **1** (λ_{exc}=287 nm) and dMA (λ_{exc}=283 nm). (D) Fluorescence spectra of various concentrations of **2** ($\lambda_{ex} = 273$ nm). All samples were measured in acetonitrile.

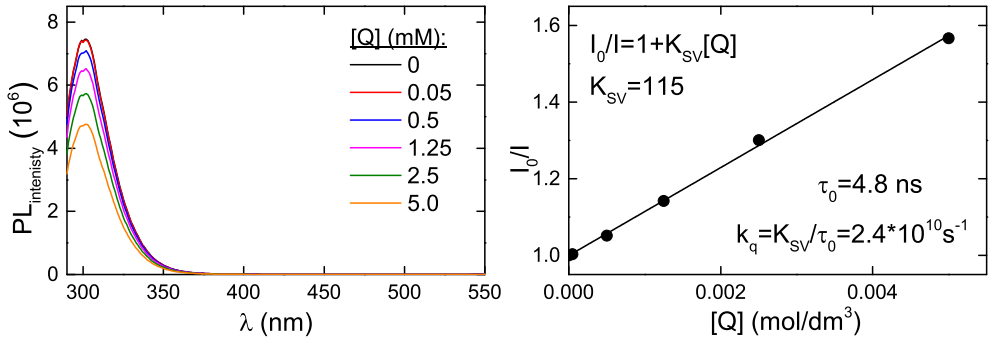

Figure 5.2 Fluorescence spectra of dMA in acetonitrile (left), in the presence of various concentrations of iPN, and corresponding Stern-Volmer plot (right). τ_0 was taken from SPC.

The steady-state fluorescence spectrum of dMA exhibits a band with a maximum at 301 nm in acetonitrile (λ_{ex}= 283 nm) and with a fluorescence quantum yield (ϕ_{PL}) of 0.21 (reference: phenol; ϕ_{PL} = 0.14[2]). The fluorescence of dMA is quenched upon addition of isopropylidenemalononitrile. The steady-state fluorescence spectra of dMA with and without quencher are compared in Figure 5.2. The formation of a new emissive species corresponding to the exciplex/CT state was not observed, as in weakly polar solvents. The quenching rate constant upon addition of iPN ([Q]= 0-5 mM) was calculated from the slope of the Stern-Volmer plot I_0/I versus quencher concentration, and is equal to $2.39 \times 10^{10}\,\mathrm{s^{-1}M^{-1}}$ in acetonitrile (Figure 5.2).

The steady-state fluorescence spectra of **1** and **2** in acetonitrile are presented in Figure 5.1. The fluorescence spectrum of **1** (λ_{ex}= 287 nm) shows a poorly visible band with a maximum at 303 nm, which corresponds to the fluorescence of locally-excited singlet state, ^{1}**1** (Φ_{PL}<0.001). As opposed to the data obtained in weakly polar solvents (chapter 4), the emissive species corresponding to the charge-transfer state was not observed in acetonitrile and 2-propanol. However, the low quantum yield of ^{1}**1** emission suggests that efficient ET occurred. Polar solvents increase the stabilization of the charge-transfer state. This results in a smaller mixing of the CT and locally-excited singlet state of the donor, and decreases the emission intensity of the charge-transfer state. Molecule **2** exhibits even weaker fluorescence of the

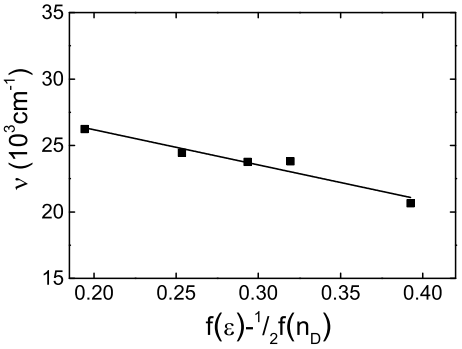

Figure 5.3 Lippert-Mataga plot of **2**, in n-butyl ether, chloroform, ethyl acetate, dichloromethane and acetonitrile.

locally-excited singlet state, $^1\mathbf{2}$, than **1** with the emission maximum around 290 nm. On the other hand, it was possible to detect a broad, structureless band at 485 nm, which belongs to the emission of charge-transfer state, $^1\mathbf{2}^{\pm}$. This species has a lower dipole moment and a slightly stronger exciplex character than $^1\mathbf{1}^{\pm}$. However, it is not an exciplex itself. The data obtained in acetonitrile fits well to Lippert-Mataga plot (Figure 5.3) together with the data obtained in middle polarity solvents. Thus, we can assume that the change in the dipole moment of **2** is insignificant for this series of solvents. Regarding molecule **1**, we cannot conclude that the dipole moment did not change with the solvent polarity, due to lack of the necessary information from the experimental result.

In both cases, increasing the concentration of the molecules does not produced significant changes in the spectrum (in **1**, no new bands appeared; in **2**, there was an increase in the intensity of the emission band, but the maxima of the emission spectrum did not change). This shows that the molecules did not adopt the face-to-face orientation which is characteristic for exciplexes. Most of the quenching occur due to non-emissive species (in the case of **1**) or weakly emissive species (in the case of **2**). The former species can only be analyzed using femtosecond pump-probe transient absorption spectroscopy, while the latter can also be analyzed by single photon counting experiments.

5.2.2 Transient Absorption

The characterization of the transient species populated by electron transfer and the consecutive processes in polar solvents was performed with femtosecond pump-probe transient absorption and flash photolysis. The former technique allows the investigation of non-emissive or poorly emissive charge-transfer state, and the latter one helps to characterize long-living species such as triplet state or free ions.

Transient absorption spectra of 3,4-dimethylanisole (1 mM) in acetonitrile were collected upon sample excitation at 273 nm, followed by probing it between 350 and 650 nm. The global fitting analysis of the collected data, using a sequential decay mechanism, allowed the assignment of three Evolution-Associated Spectra (Figure 5.4 C), which are similar to the ones found in isopropyl ether. The first component with the shortest lifetime was assigned to the initially-populated Franck-Condon state of the donor ($^1D^*$), that via vibrational relaxation leads to the lowest vibronic state of the singlet excited state (^1D). ^1D decays in 4.89 ns and gives rise to a long living species, assigned to the triplet state (^3D). 3,4-Dimethylanisole in acetonitrile follows first-order kinetics $^1D^* \rightarrow^1 D\,(\rightarrow) \rightarrow {}^3D$. In this case, the assigned EAS correspond to the true Species-Associated Spectra (SAS). Transient spectra of dMA collected at various time delays are shown in Figure 5.4 A and B. The population of the triplet state was confirmed by flash photolysis experiments, in which degased samples of dMA in acetonitrile were excited at 266 nm, and the triplet-triplet absorption spectra were collected (Figure 5.4 D). The generated transient band has a maximum at 300 nm. The lifetime of ^3D measured in deaerated acetonitrile solution is $2 \pm 0.2\,\mu$s, which is in good agreement with the triplet lifetime of anisole measured in the same experimental conditions.

The global analysis of the data in acetonitrile in the presence of 100 mM of the isopropylidenomalononitrile, shows that four lifetimes are necessary to fit the transient absorption. The Evolution-Associated Spectra presented in Figure 5.4 G do not correspond to the true Species-Associated Spectra, and, in addition, they differ significantly from the EAS obtained in isopropyl ether. The first EAS, represents

the populated Franck Condon state, $^1D^*$, which decays rapidly to the excited singlet state, ^1D . The second EAS seems to belong to the ^1D with some feature of charge transfer state. This may be explained by electron transfer reactions in bimolecular systems occurring at various donor-acceptor distances, i.e., some molecules can undergo electron transfer, while others still need to approach to closer distance.

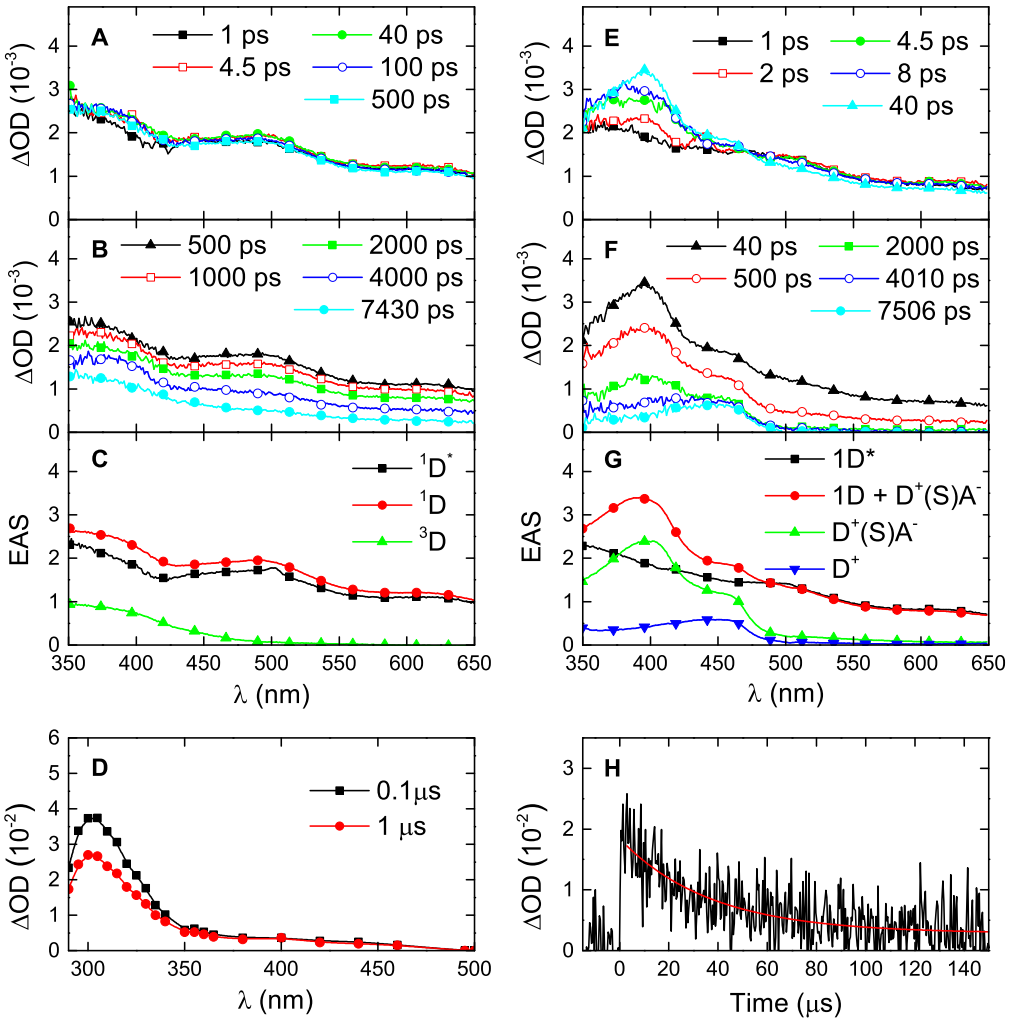

Figure 5.4 Transient absorption spectra of dMA in acetonitrile, in the absence (A, B) and presence of 100 mM of iPN (E, F), in chosen time delays upon excitation. Evolution-Associated Spectra are presented in (C) and (G). Triplet-triplet absorption spectra of dMA in ACN (λ_{ex}= 266 nm), taken 0.1 and 1 μs after flash (D). Decay of the free ion populated in the sample containing 1 mM of dMA and 2 mM of iPN, excited at 266 nm and collected at 470 nm (H).

The decay of the ^1D state was fitted to a monoexponential function and gave lifetime (τ) value of 380 ps. This value is consistent with the value calculated from the Stern-Volmer plot when [Q] = 100 mM. In a polar solvent, loose ion pairs are formed upon ET and decay within 1.76 ns (associated with the third EAS) to the plateau, which is not a baseline. The plateau corresponds to the generation of free ion pairs, with the maximum of the transient spectrum at 460 nm, typical for the radical cation of anisole absorption (fourth EAS),[3] that decay to the ground state on the longer time scale. The population of the free ions is possible due to a relatively slow charge recombination of loose ion pairs to the ground state, thus the dissociation into free ions may occur. Gould et al. showed that deactivation of the LIP formed between aromatic hydrocarbons and 2,6,9,10-antracyanoanthracene in acetonitrile, may occur by charge recombination to the ground state with a rate of $(0.78 - 6.3) \times 10^{10}\,\mathrm{s}^{-1}$, which is accompanied by the formation of free ions with separation rate k_{sep}=$8 \times 10^8\,\mathrm{s}^{-1}$.[4] Transient absorption spectra at various time delays are presented in Figure 5.4 E and F. The persistent band was further studied with flash photolysis. Probing the 3,4-dimethylanisole (1 mM) in the presence of 2 mM of iPN at 470 nm, upon excitation at 266 nm, led to the observation of long living species, which was assigned to the free cation (D^+) with the lifetime of 30 µs in the absence of oxygen. The decay of this species is presented in Figure 5.4 H.

The quenching effect of the singlet excited state of 3,4-dimethylanisole by isopropylidenomalononitrile is better visible be comparing the decays in the chosen wavelengths (Figure 5.5). We can clearly observe quenching of the donor and the existence of a long leaving species in the presence of the quencher at 455 nm. The decay at 455 nm leads to a plateau and not to the baseline. The 2D images of the collected data are presented in the same figure.

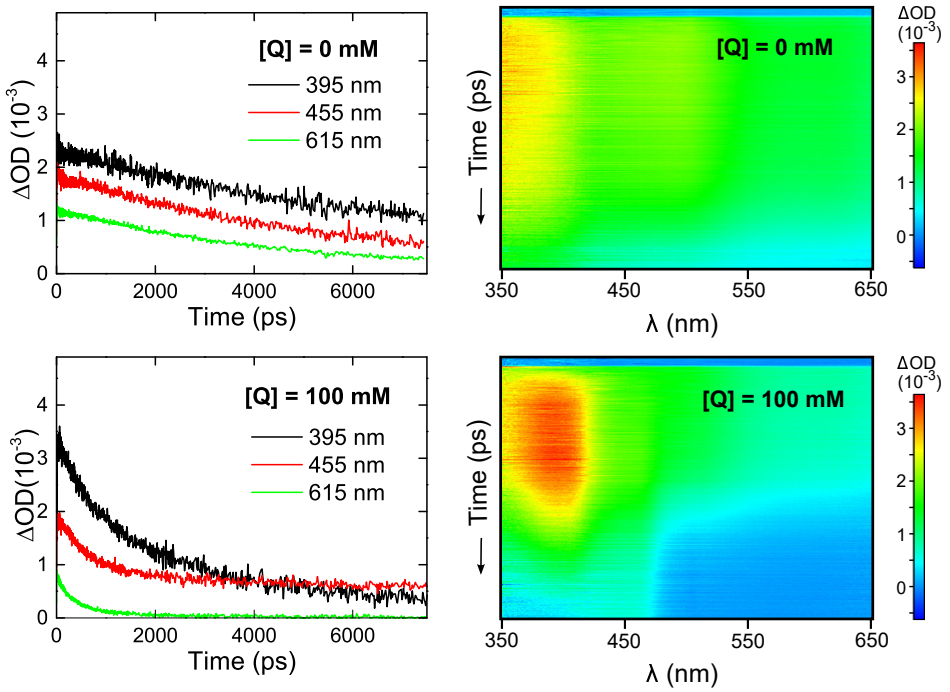

Figure 5.5 Time profiles of transient absorption of dMA in the absence and presence of 100 mM of iPN in acetonitrile, monitored at 395, 455 and 615 nm. 2D images of the collected data, after solvent subtraction and chirp correction, are also presented.

Additionally, it was also possible to follow the changes in the transient absorption in the near-infrared region. We assigned just one Evolution-Associated Spectrum which correspond to the ^1D, with the lifetime 4.51 ns, which is in perfect agreement with lifetime from the studied UV region, although the fitting is not perfect, due to the weak signal and background noise. The absence of the triplet state can be explained by the lack of the triplet-triplet absorption of the ^3D in the near-infrared region.

Addition of the 100 mM of iPN, shorten the lifetime of ^1D to 280 ps, which is comparable with the result obtained in the UV region. This leads to the formation of the loose ion pair (τ_{LIP}=1.61 ns), which gives rise to a new long-living species. This species with the maximum out of the experimental window, correspond most likely to the free anion. Transient absorption spectra collected at various time delays and calculated Evolution-Associated Spectra are shown in the Figure 5.6. Time profiles measured at 860 and 1340 nm are presented with the 2D images in Figure 5.7.

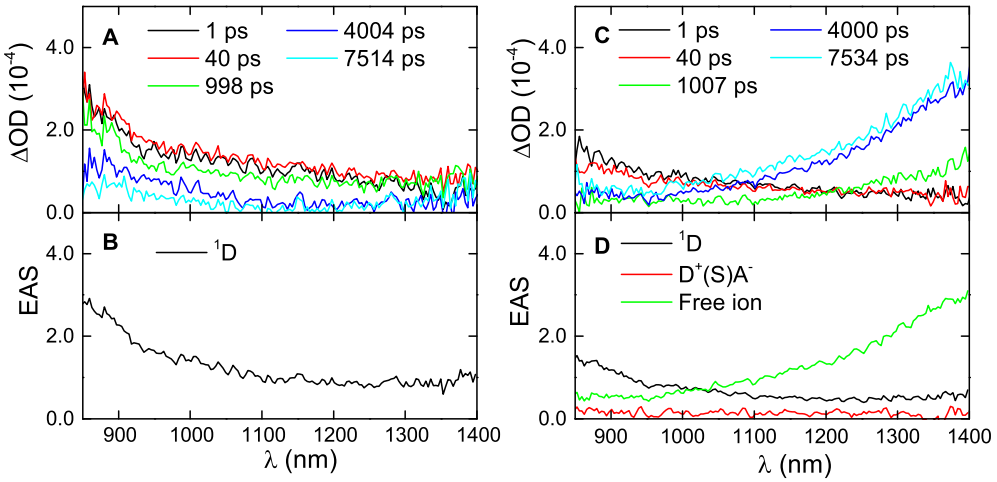

Figure 5.6 Transient absorption spectra of dMA in the absence (A) and presence of 100 mM of iPN (C) in acetonitrile, at various times delays, measured in the NIR. Evolution-Associated Spectra are presented on B and D for samples without and with quencher, respectively.

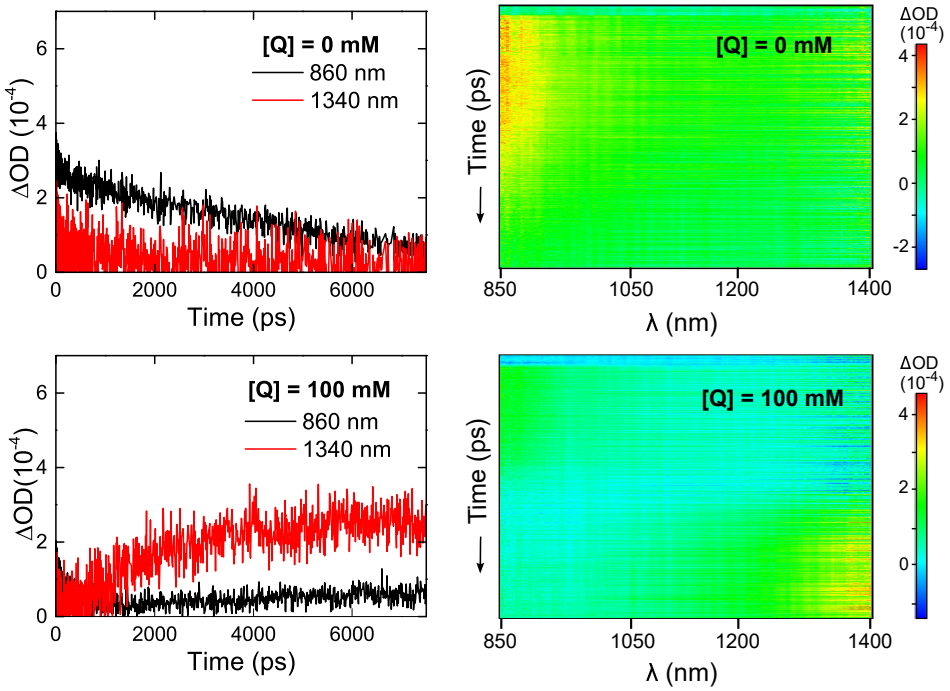

Figure 5.7 Time profiles of transient absorption of dMA in the absence and presence of 100 mM of iPN in acetonitrile, monitored at 860 and 1340 nm. 2D images of the collected data, after solvent subtraction and chirp correction, are also presented.

Femtosecond transient absorption was also used to study the intramolecular systems in polar solvents. Compound **1** in acetonitrile was excited at 287 nm and probed between 340 and 650 nm. Transient absorption spectra of **1**, collected at various time delays, are presented in Figure 5.8. Two lifetimes were necessary to describe the transient species observed in ACN (beside the lifetime of Franck-Condon state, $^1\mathbf{1}^*$), which were assigned to the locally-excited state, $^1\mathbf{1}$ and to the charge-transfer state $^1\mathbf{1}^{\pm}$, with an intense band around 465 nm. The $^1\mathbf{1}^{\pm}$ band has the same spectral profile as in middle polarity solvents, however it exhibits a weak shift to the higher energy. We could observe an isosbestic point, which confirms that charge-transfer state is populated by decay of $^1\mathbf{1}$. This is also seen in the analysis of the time profiles presented in Figure 5.9. The high value of the charge recombination rate of $^1\mathbf{1}^{\pm}$ in acetonitrile ($4.17\times10^9\,s^{-1}$) excludes the possibility of the intersystem crossing to the $^3\mathbf{1}^{\pm}$. Lifetime of $^1\mathbf{1}^{\pm}$ is too short for hfc-isc to occur.

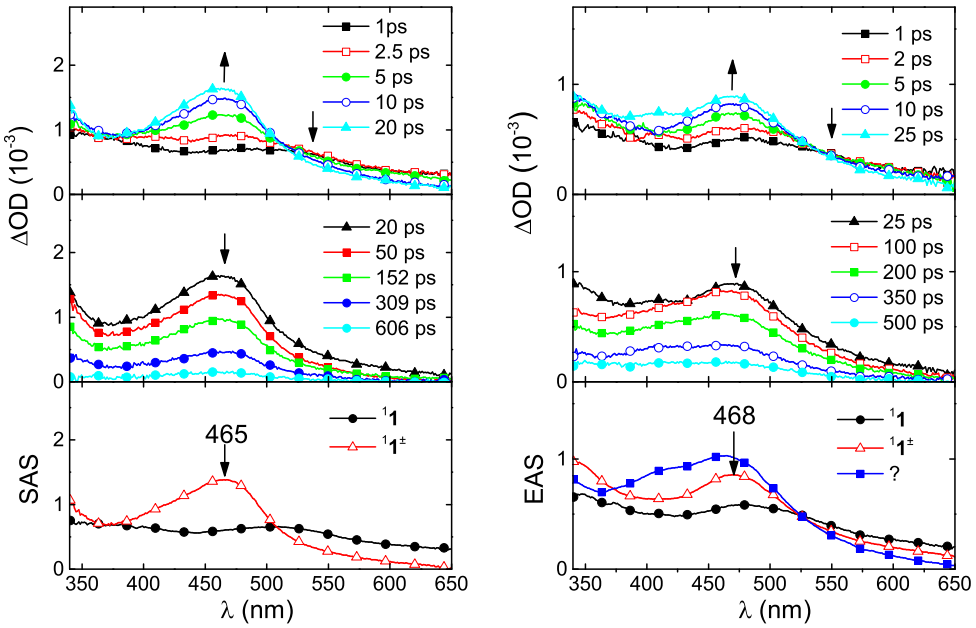

Figure 5.8 Transient absorption spectra of **1** in acetonitrile (left: top and center) at various time delays and corresponding Species-Associated Spectra (left: bottom). Transient absorption spectra of **1** in 2-propanol (right: top and center) at various time delays and corresponding Evolution-Associated Spectra (right: bottom).

A different situation was observed in the experiment performed in 2-propanol (POH). In this case, an additional lifetime was necessary to obtain a relatively good fit of the data. The Evolution-Associated spectrum has a band similar to the one of ^1CT, but more broad (Figure 5.8). However, it is impossible to assign the band to a concrete species. A possible explanation for the additional band could be the existence of a hydrogen bonded species but the higher viscosity of 2-propanol also opens other alternatives. Studies in other alcohols will be necessary to clarify these systems and asses possible change in the mechanism of decay of $^1\mathbf{1}$.

The time profiles collected at various wavelengths are presented in Figure 5.9, together with the 2D images of all collected data. Lifetimes obtained by femtosecond transient absorption, at various temperatures, are presented in Table 5.1.

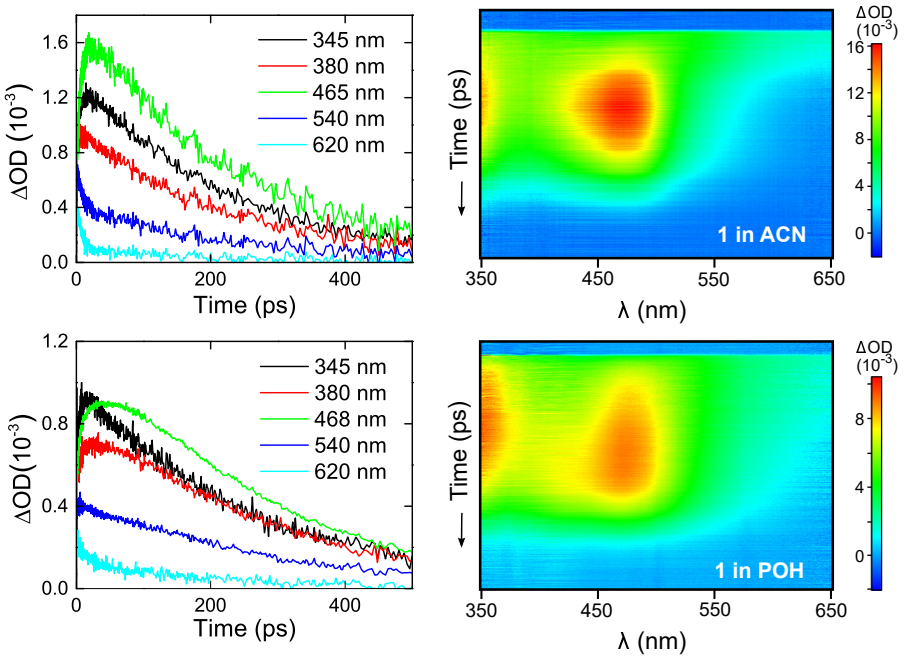

Figure 5.9 Time profiles of **1** in acetonitrile (top) and 2-propanol (bottom) measured at various wavelengths (λ_{ex}=287 nm). The 2D images of the collected data are also presented.

The CS rates are fast, equal to $1.43 \times 10^{11}\,s^{-1}$ and $1.48 \times 10^{11}\,s^{-1}$ in acetonitrile and 2-propanol, respectively. The value obtained in ACN confirms the good estimation of the CS rate by Pasman et al..[5] They estimated an ultrafast charge separation ($k_{CS} > 10^{11}\,s^{-1}$) from the level of fluorescence quenching of $^1\mathbf{1}$, however, ET rate

was to fast to be determined with any accuracy by their experimental setup.[6]

Table 5.1 Lifetimes of Species-Associated Spectra of **1** obtained by femtosecond transient absorption, at various temperatures.

System	T(K)	τ_{CS} (ps)	τ_1 (ps)	τ_2 (ps)
	323	7.11	-	244.68
	293	6.98	-	239.68
1/ACN	276	7.14	-	239.21
	253	7.58	-	238.00
	235	7.11	-	238.05
1/POH[a]	293	5.96	50.80	265.19

[a] fitting is not so good

The charge separation rates in middle polarity and polar solvents shows the following dependence: k_{CS}(DBE) < k_{CS}(CHF) < k_{CS}(DCM) > k_{CS}(ACN). If the charge separation follows the same free-energy dependence in all solvents, this would suggest that the CS occurs in the inverted region in polar solvents, due to the high exothermicity of the system.

Femtosecond transient absorption spectra of **2** in acetonitrile, collected upon excitation at 273 nm are presented in Figure 5.10. The target analysis gave just two Species-Associated Spectra (beside the Franck-Condon state). The first SAS, was assigned to the ^{1}**2**, which populates ^{1}CT bellow 25 ps in all studied temperatures (isosbestic point can be observed). Charge transfer state ^{1}**2**$^{\pm}$ in acetonitrile has a spectrum with a broad band with maximum around 425 nm, which is blue shifted in comparison with data in moderate polarity solvents. This shift is larger than in **1.** From the Lipper-Mataga plot we know that dipole moment did not change upon increasing the polarity of the solvent. The hypsochromic shift probably occurred due to higher solvation of the charge-transfer state. The decay of this state was monoexponential. Lifetimes of SAS of **2** are presented in Table 5.2.

In both molecules, the charge transfer state lies below the locally-excited triplet state, thus the latter one is not energetically accessible. The lack of the triplet state was confirmed by performing the flash photolysis experiment for **1** and **2** in deaerated ACN solution. Triplet-triplet absorption was not observed.

Table 5.2 Lifetimes of Species-Associated Spectra of **2** obtained by femtosecond transient absorption in acetonitrile, at various temperatures.

System	T(K)	τ_{CS} (ps)	τ_2 (ns)
2/ACN	323	21.59	9.76
	293	22.26	10.82
	253	24.45	7.77
	235	24.43	7.77

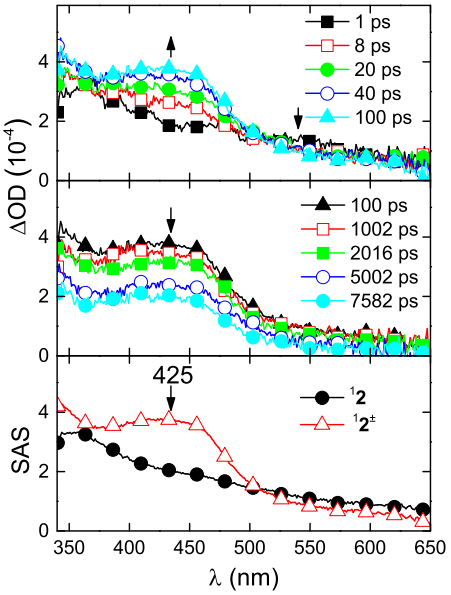

Figure 5.10 Transient absorption spectra of **2** in acetonitrile (top and center) at various times delays and corresponding Species-Associated Spectra (bottom).

5.2.3 Single Photon Counting

A monoexponential fitting was applied to the decay of dMA emission in ACN. The lifetime value (4.8 ns) obtained by single photon counting (Figure 5.11) is similar to the value obtained with the femtosecond transient absorption experiment (4.5 ns).

Monoexponential fittings were applied to the all samples containing quencher (Figure 5.11). The quenching rate constant of dMA in acetonitrile, in the presence of various concentration of iPN ([Q]=0-5 mM), was equal to $2.13 \times 10^{10}\,s^{-1}M^{-1}$. This value is in good agreement with results obtained from Stern-Volmer plot and with diffusion rate constant in acetonitrile. SPC and the plot of rate constant vs quencher concentration are presented in Figure 5.12.

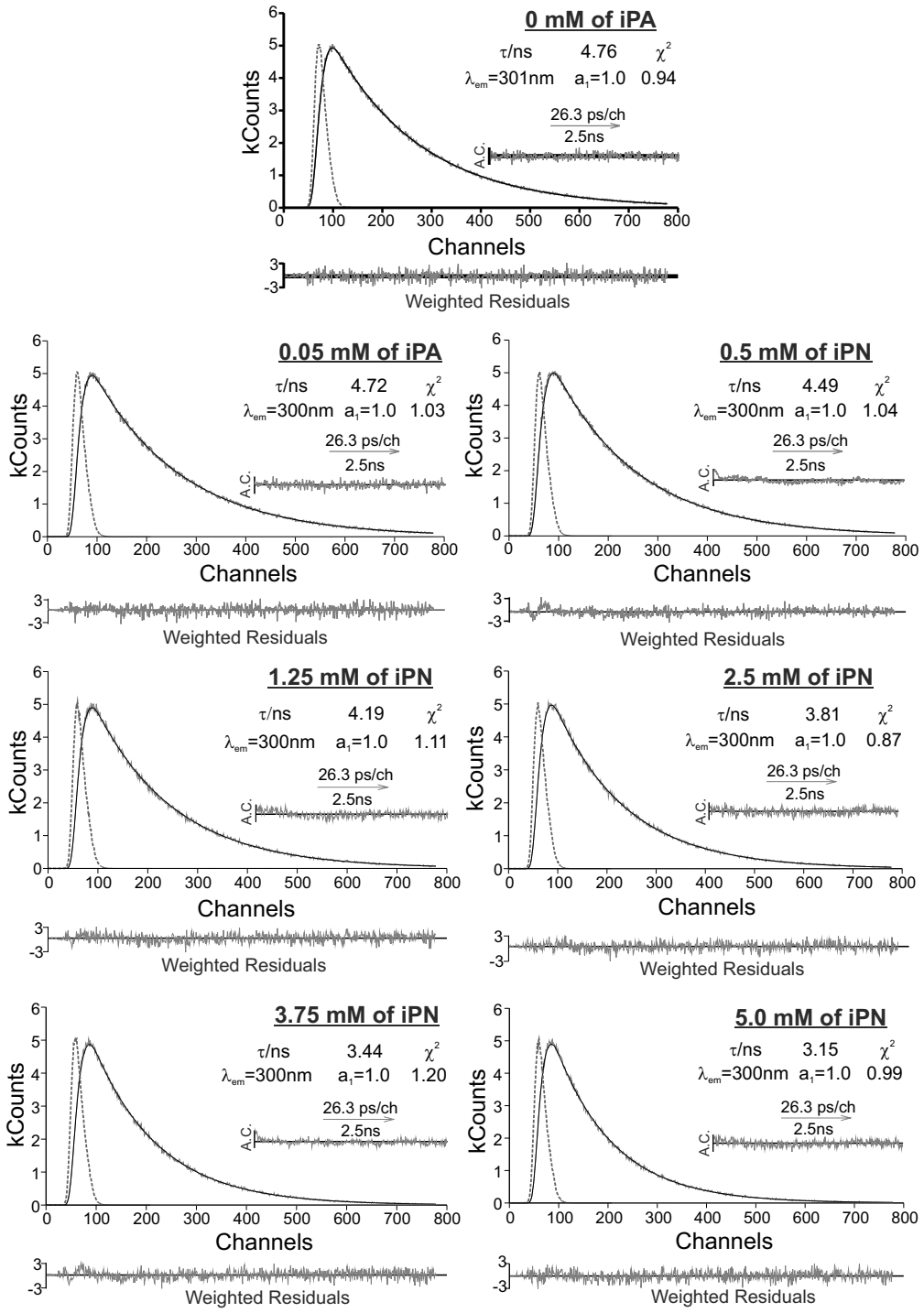

Figure 5.11 Single Photon Counting of dMA in the presence of various concentrations of iPN, in ACN, with applied monoexponential fitting after excitation at 282 nm, at 20°C. Weighted residuals, autocorrelated function (A.C.) and χ^2 values are also presented. The instrument response function is presented by the dashed line.

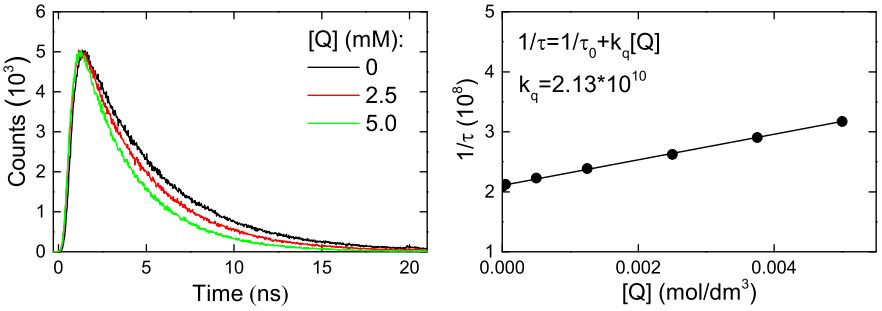

Figure 5.12 Left: SPC decays of dMA in the presence of various concentrations of quencher in acetonitrile. Right: Plot of rate constant vs quencher concentration in acetonitrile.

The fluorescence of the CT state ($^1\mathbf{1}^{\pm}$) was not observed in ACN and POH, therefore we could not measure its lifetime by SPC. However, it was possible to measure the fluorescence lifetime of $^1\mathbf{2}^{\pm}$ in ACN at 20°C (Figure 5.13). Biexponential fitting had to be apply to analyze the decay. The locally-excited triplet state, $^3\mathbf{2}$, lies higher in energy than $^1\mathbf{2}^{\pm}$ or $^3\mathbf{2}^{\pm}$. However, the previous chapter showed that the values of $^1k_{isc}$ and $^3k_{isc}$ for **2** are slightly larger, in the (1-2)$\times 10^9\,\mathrm{s}^{-1}$ range, than those expected from the hfc-isc mechanism and obtained for **1**, which are in the (1-5)$\times 10^8\,\mathrm{s}^{-1}$ range. Such high values were tentatively assigned to a higher mixture of locally-excited state character in the wavefunction describing $\mathbf{2}^{\pm}$ compared to $\mathbf{1}^{\pm}$, which is indeed the reason why emission from $^1\mathbf{2}^{\pm}$ is observed in acetonitrile. Such large intersystem crossing rates in $\mathbf{2}^{\pm}$ are competitive with its $\approx 10^8\,\mathrm{s}^{-1}$ CR rate obtained by transient absorption and may lead to biexponentiality. The transient absorption spectra and lifetimes of $^1\mathbf{2}^{\pm}$ and $^3\mathbf{2}^{\pm}$ are expected to be indistinguishable and the spectra is adequately fitted with only one CT species in ACN.

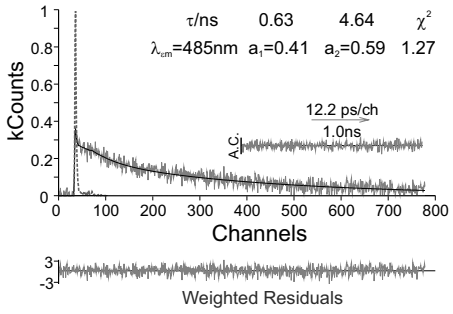

Figure 5.13 SPC decay of $^1\mathbf{2}^{\pm}$ in ACN with applied biexponential fitting (λ_{ex}=287 nm).

5.2.4 Temperature and free-energy dependence on ET rates

Changes in large dielectric constants (e.g., $\varepsilon = 37$ for acetonitrile at 293 K and $\varepsilon = 48$ at 235 K) lead to very modest changes in the free-energy of ET reactions. For example, the free-energy in acetonitrile changes from -29.44 kcal/mol at 323 K to 30.03 kcal/mol at 235 K for **1**, and from -17.70 kcal/mol at 323 K to -18.32 kcal/mol at 235 K for **2**. Such small changes in ΔG^0 have little impact in the temperature dependence of reactions in acetonitrile. Thus, the apparent activation energy of charge recombinations in both molecules in acetonitrile is only slightly negative, as shown in Figure 5.14. Table 5.3 presents the calculated free energies, charge separation and charge recombination rates.

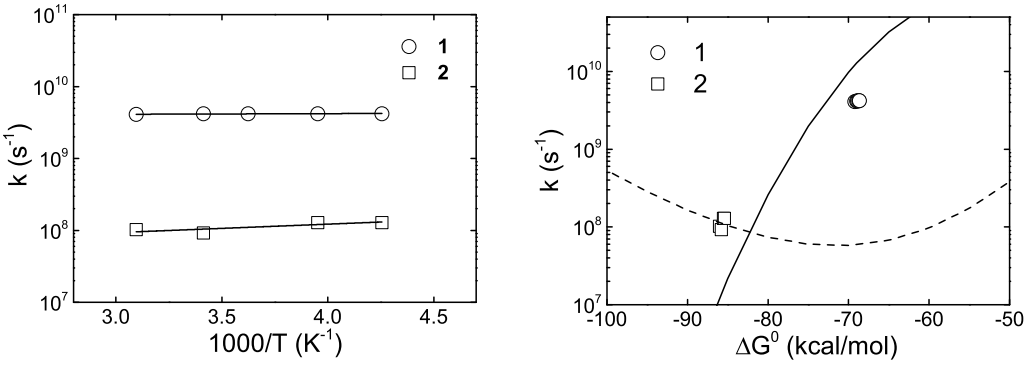

Figure 5.14 Left: Arrhenius plots of charge recombination of **1** and **2** in ACN. Right: Charge recombination of **1** and **2** as a function of the driving force in various temperatures in ACN. Intersecting-State Model calculations with applied $\Lambda = 40$ and $\Lambda = 70$ are represented with the full and dashed line, respectively.

Table 5.3 The free energy, CS and CR rates obtained by femtosecond transient absorption in acetonitrile.

System	T (K)	ΔG_{CS}(kcal/mol)	k_{CS} (s^{-1})	ΔG_{CR}(kcal/mol)	k_{CR} (s^{-1})
1/ACN	323	-29.44	1.41×10^{11}	-69.23	4.09×10^{9}
	293	-29.67	1.43×10^{11}	-69.00	4.17×10^{9}
	276	-29.79	1.40×10^{11}	-68.88	4.18×10^{9}
	253	-29.93	1.32×10^{11}	-68.74	4.20×10^{9}
	235	-30.03	1.41×10^{11}	-68.64	4.20×10^{9}
2/ACN	323	-17.70	4.63×10^{10}	-86.03	1.02×10^{8}
	293	-17.94	4.49×10^{10}	-85.79	9.24×10^{7}
	253	-18.21	4.09×10^{10}	-85.55	1.29×10^{8}
	235	-18.32	4.09×10^{10}	-85.41	1.29×10^{8}

The temperature independence of these reactions, which occur in the inverted region, demonstrates that nuclear tunneling remains the dominant mechanism of charge recombination in a polar solvent. The small changes in ΔG^0 with the temperature and the difficulty of expanding the range of ΔG^0 with different polar solvents without a change in mechanism, limit the ability to define the free-energy relationship of ET in polar solvents using the intramolecular systems available for this study. An extension of the ΔG^0 range would require additional molecules. Nevertheless, it is useful to compare the ET rate constants in acetonitrile with those obtained for weakly and moderately polar solvents. Figure 5.15 shows that, at room temperature, the charge recombination rate of $^1\mathbf{2}^{\pm}$ in ACN ($\Delta G^0 \approx -86$ kcal/mol, $^1k_{CR}=9.2 \times 10^7\,s^{-1}$) is very similar to that of $^1\mathbf{1}^{\pm}$ in NBE (–86 kcal/mol, $8.7 \times 10^7\,s^{-1}$), but that of $^1\mathbf{1}^{\pm}$ in ACN (–69 kcal/mol, $4 \times 10^9\,s^{-1}$) is distinctly different from the charge recombination of $^1\mathbf{1}^{\pm}$ in DCM (–74 kcal/mol, $7 \times 10^7\,s^{-1}$). In other words, ACN does not seem to fit in the same free-energy relationships as the less polar solvents.

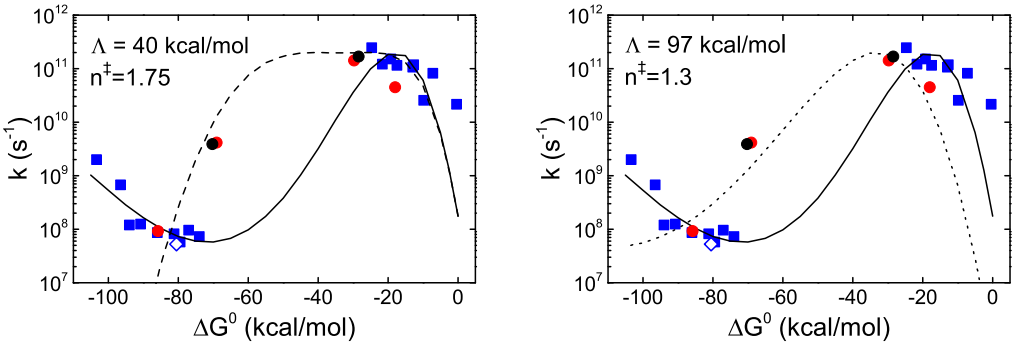

Figure 5.15 ET transfer rates of **1** and **2** in ACN (red circles) and in less polar solvents (blue squares). ET transfer rates of **1** in POH (black circles) and CR rate of **1** in diethyl ether[5] (◊). Left: The calculations differ only in the value of Λ (Λ= 40 kcal/mol fits polar solvents calculations (dashes line) and Λ= 70 kcal/mol fits the less polar solvents (full line)). Right: dotted fitting represent the increase in the solvent reorganization energy obtained by decreasing $n^{\ddagger}$ to 1.3 and increasing Λ to 97 kcal/mol.

A likely reason for the difference between ACN and less polar solvents is the change of the solvent reorganization energy, λ_s. In polar solvents a higher solvation of the radical ions is expected, thus also higher λ_s. Based on the evidence that the dielectric continuum approximation overestimates λ_s,[7] probably by a factor of

two,[8–10] it was estimated in chapter 4 that λ_s is approximately 6±3 kcal/mol for the weakly and moderately polar solvents discussed in that chapter. The maximum rate in ACN is observed at ΔG^0= –30 kcal/mol, which suggests $\lambda_s + \lambda_v \approx$ –30 kcal/mol, and together with $\lambda_v \approx$ 14 kcal/mol estimated in chapter 4 for molecules **1** and **2**, leads to $\lambda_s \approx$ –16 kcal/mol. Although λ_s may be expected to increase by 10 kcal/mol from NBE (ε= 3.1) to ACN (ε= 37), it is very difficult to reconcile this difference in λ_s with approximately the same charge recombination rate ($9.2 \times 10^7 s^{-1}$ vs. $8.7 \times 10^7 s^{-1}$) at a very similar driving force (–86.0 to –85.8 kcal/mol).

Figure 5.15 presents an alternative explanation for the similar rates of polar and weakly polar solvents at –86 kcal/mol but a two order of magnitude difference at -70 kcal/mol. Lowering the value of Λ from 70 to 40 kcal/mol changes the free-energy relationship and provides a slightly better fit to the data in ACN. As mentioned before, the value of Λ reflects the coupling to nonreactive modes. The limit of $\Lambda = \infty$ leads to the Marcus inverted parabola dependence of the rates on the driving force of ET reactions (i.e., λ is independent of ΔG^0). A decrease in the value of Λ means a higher increase in the sum of bond extensions with $|\Delta G^0|$, thereby higher increase of λ with $|\Delta G^0|$.[11] The fitting in Figure 5.15 suggests that more excess energy is released to solvent modes in ACN than in less polar solvents. ACN is more strongly coupled with the reaction coordinate and adds to the reorganization energy of the ET reactions. Figure 5.14 compares the temperature dependence predicted by the tunneling calculations with the experimental rates.

We used a simple continuum model of the solvent to estimate free-energy. However, Heitele et al. suggested that this may lead to some errors in the calculations of the driving force.[12] These authors suggested that the correction for the solvation energy should be applied to account for the effective radius of the solvent,[12] by employing the mean-sphere approximation.[13,14] The application of the correction seems reasonable, especially as it was already pointed out in chapter 1, the dielectric continuum model seems to work poorly for calculation of λ_s. Our preliminary calculations (not presented here) show that weakly polar solvents are affected by the

correction factor, thus the difference in the driving forces for polar and middle polarity solvents increases. Nevertheless, the application of this model to the analysis of our data needs to wait for the measurement of the redox potentials of donor and acceptor, that are estimated in our calculations.

5.3 Conclusions and Future Direction

The electron transfer rates in polar solvents seem to follow a different free-energy dependence than in less polar solvents. One plausible explanation is the increase in the reorganization energy due to an increase of solvation and a stronger coupling of medium to the solute's reaction coordinate. The other possibility is that the free-energy dependence is the same as in weakly polar solvent, however, it is displaced to the higher driving force due to changes in the solvent reorganization energy. Although the fittings in Figure 5.14 and Figure 5.15 are very encouraging, they should be interpreted with extreme care: data on more intramolecular systems closely related with molecules **1** and **2** must be collected in ACN to consolidate the free-energy dependence hinted by the data available, and a definitive theoretical interpretation must await for the availability of such data.

In the literature, other explanations for the change in rate with solvent polarity can be found. For example, a decrease in the transition state $n^{\ddagger}$ was observed with an increase in solvent polarity, due to a small interaction of the electrons of the reactive bonds with those of the solvents.[15] Mataga et al. suggested an increase in the Franck-Condon factor due to an increase in the frequency of the solvent reorientational phonon around the charged molecule.[16] These explanations were not proposed for the intramolecular systems, but they can not be excluded from our interpretation before additional experiments are performed, expanding the range of intramolecular systems studied in the same polar solvents. Additionally, in order to obtain information about possible changes in the geometry of the solvated charge-transfer state (which may affect the ET rates), the molecular geometry of the solute in the presence of the polarized solvent should be optimized.

Even though we do not have enough data to precisely interpret the results obtained in polar solvents, we can conclude that proper choice of solvent polarity has a huge impact on the charge separation and charge recombination, which differs from the commonly used dependencies. For example, by decreasing the dielectric constant from $\varepsilon = 37$ in acetonitrile to $\varepsilon = 9$ in dichloromethane, the charge recombination rate decreased ∼60 times in **1**, and increased ∼5 times in **2**. This makes dichloromethane a better medium to store usable chemical energy in **1** and acetonitrile in **2**. This results give an example on how knowledge about the solvent dependence on charge separation and charge recombination rates may contribute to the design of more efficient ET-based materials.

References

1. J. Najbar, R. C. Dorfman and M. D. Fayer, *J. Chem. Phys.*, 1991, **94**, 1081–1092.

2. M. Montalti, L. Prodi, A. Credi and M. T. Gandolfi, *Handbook of Photochemistry*, CRC Press, 3rd edn, 2006.

3. S. Takamuku, S. Komitsu and S. Toki, *Radiatiation Phys. Chem.*, 1989, **34**, 553–559.

4. I. R. Gould and S. Farid, *J. Phys. Chem.*, 1992, **96**, 7635–7640.

5. P. Pasman, G. F. Mes, N. W. Koper and J. W. Verhoeven, *J. Am. Chem. Soc.*, 1985, **107**, 5839–5843.

6. P. Pasman, F. Rob and J. W. Verhoeven, *J. Am. Chem. Soc.*, 1982, **104**, 5127–5133.

7. S. J. Formosinho, L. G. Arnaut and R. Fausto, *Prog. React. Kinet.*, 1998, **23**, 1–90.

8. M. D. Newton, M. V. Basilevsky and I. V. Rostov, *Chem. Phys.*, 1998, **232**, 201–210.

9. H.-S. Ren, M.-J. Ming, J.-Y. Ma and X.-Y. Li, *J. Phys. Chem. A*, 2013, **117**, 8017–8025.

10. X.-Y. Li, *Int. J. Quantum Chem.*, 2015, **115**, 700–721.

11. L. G. Arnaut, S. J. Formosinho and H. D. Burrows, *Chemical Kinetics*, Elsevier, Amsterdam, 2007.

12. H. Heitele, P. Finckh, S. Weeren, F. Pöllinger and M. E. Michel-Beyerle, *J. Phys. Chem.*, 1989, **93**, 5173–5179.

13. P. G. Wolynes, *J. Chem. Phys.*, 1987, **86**, 5133–5136.

14. I. Rips, J. Klafter and J. Jortner, *J. Chem. Phys.*, 1988, **88**, 3246–3252.

15. S. J. Formosinho and L. G. Arnaut, *J. Photochem. Photobiol. A Chem.*, 1994, **82**, 11–29.

16. N. Mataga, Y. Kanda and T. Okada, *J. Phys. Chem.*, 1986, **90**, 3880–3882.

6 General Conclusions and Final Remarks

This work focused on bimolecular and intramolecular systems that could give some insight about the mechanism of electron transfer reactions. Aromatic hydrocarbons and nitrile groups were chosen as electron-donors and electron-acceptors, respectively, to allow for the investigation of very exothermic reactions. To the best of our knowledge this is the first time that ET reactions are controlled over a range of 100 kcal/mol in exothermicities.

We found an interesting relationship between rates and free-energy, distinct from the well-known Marcus normal, optimal and inverted region. The increase in exotermicities above $\Delta G^0 <$ -70 kcal/mol, increased ET rates, both in bimolecular and intramolecular systems, giving rise to a new "double inverted region". Additionally, faster rates were observed for weakly polar solvents with higher activation energies than activationless rates observed in more polar solvents. The observation of rates that are faster when $E_a > 0$ than when $E_a \approx 0$ is contrary to the dogma of chemical reactivity. This unexpected behavior can be explained by the decrease of the solvent dielectric constant with the increase in temperature, which therefore increases the exothermicities of charge recombination rates. In the "double inverted region" more exothermic charge recombination become faster as exotermicity increases as the result of the increase in temperature ($E_a > 0$). The charge recombination rates become slower in the inverted region when the increase in temperature increase the

exothermicity.

Widely accepted formulations of the rates of ET reactions fail to explain the end of Marcus inverted region and the change from negative to positive activation energies with decreasing solvent polarity. A possible explanation for the breakdown of this firmly held belief is a change in reaction coordinate as the exothermicity of ET reaction increases, elicited by the increased involvement of high-frequency vibrational modes. Here, we used the Intersecting-State Model (ISM), which accounts for nuclear tunneling and changes in the displacement, d, between donating and accepting vibrational modes, to explain the data observed experimentally. There has been a very good agreement between theoretical and experimental results.

We showed that charge recombination rates of weakly and moderated polar solvents fit the same free-energy relationship. This shows that the solvent reorganization energy, λ_s is largely overestimated by Marcus two-sphere dielectric continuum model. This is also evidenced by the lack of strong displacement of the onset of the Marcus inverted region in bimolecular photoinduced charge separation (PCS). Charge recombinations in acetonitrile seem to follow a different free-energy relationship. Only activationless rates were observed in this solvent, although charge recombinations were investigated to ΔG^0= -80 kcal/mol. Apparently acetonitrile is more strongly coupled with the reaction coordinate and contributes more significantly to the increase of the reorganization energy with the driving force of the reaction.

Detailed characterization of the species involved in charge separation and charge recombination, was obtained by use of the various experimental techniques that allow to study of ultrafast and relatively slow processes. It was shown that pump-probe spectroscopy is a great tool to study non-emissive species, which cannot be characterized by other techniques. The combination of femtosecond transient spectroscopy with picosecond time-correlated single photon counting in the investigation of electron transfer reactions in the systems synthesized to probe very exothermic reactions, enable the unquestionable observation of the “double inverted region”

predicted by Intersecting-State Model in 1991.[1] However, the nature of the free-energy relationship in acetonitrile needs to be further investigated with molecules that further expand the range of driving forces of the ET reactions in this solvent.

References

1. L. G. Arnaut and S. J. Formosinho, *J. Mol. Struct. THEOCHEM*, 1991, **233**, 209–230.

A Appendix

The synthesis of estrone derivatives **1** and **2** performed by Prof. Arménio Serra is outlined in Figure 4.2. The detailed descriptions of procedures are presented below.

Synthesis of the estrone derivative **1b** (3-methoxy-1,3,5 (10)-estratrien-17-one). In a pressure tube 1.0 g (3.7 mmol) of estrone (3-hidroxy-1,3,5 (10)-estratrien-17-one) (**1a**), 1.2 g (3.6 mmol) of potassium carbonate and 2.0 mL of methyl iodide (16 mmol) were added to 50 mL of acetone. The mixture was placed in an oil bath at 60^{o}C for 24 h. The formation of the methyl ether was monitored by NMR. Incomplete methylation led to the addition of another amount of methyl iodide and the reaction was continued. The precipitate that was formed was filtered and the liquid evaporated at reduced pressure. The solid residue was recrystallized in dichloromethane/methanol originating 0.81 g (η=78 %) of the estrone derivative **1b** (m.p.=168-169.5^{o}C).

Synthesis of the estrone derivative **1** (3-methoxy-1,3,5 (10)-estratrien-17-yliden) malononitrile). The introduction of the dicyano group was carried out using described procedures.[1,2] In a round flask 400 mg of **1b** (1.4 mmol), 590 mg of ammonium acetate, 1.52 mL of acetic acid and 309 mg (4.68 mmol) of malononitrile were added to 30 mL of toluene. The solution was refluxed overnight in a Dean-Stark apparatus, under nitrogen. The solution was treated with a saturated solution of $NaHCO_3$ (50 mL), washed with water, dried over Na_2SO_4 and the solvent evaporated under reduced pressure. The residue was subject to column chromatography (silica, DCM and then EAC). The product was recrystallized in ethanol originating 273 mg (η=56 %) of **1** (m.p.=188-189^{o}C; 190^{o}C).[3]

The estrone derivative **2b** (3-[1,2-benzisothiazole-1,1-dioxide]-1,3,5 (10)-estratrien-17-one) was prepared following a described procedure.[4] In a round bottom flask 1.2 g of **1a** (4.4 mmol), 0.7 mL of triethylamine and 1.0 g (4.9 mmol) of pseudosaccharyl chloride were added to 100 mL of toluene and refluxed for 2 hours under N_2. The hot solution was filtered and the liquid left to cool to room temperature. The precipitate **2b** was filtered and dried. The material was chromatographed (silica-gel DCM/ethyl ether 3:1) to yield 0.70 g (η=36 %) of **2b** (m.p.=261-263^{o}C decomposition).

The estrone derivative **2c** (1,3,5 (10)-estratrien-17-one) was prepared following a described procedure.[4] In a round bottom flask 0.45 g (0.10 mmol) of **2b** and 1.0 g of C/Pd (10 %) were added to 100 mL of benzene and heated to reflux. A solution of 2.6 g (30 mmol) of sodium hypophosphite in 50 mL of water was added stepwise and the mixture was stirred under reflux during 4 hours. After cooling to room temperature the catalyst was filtered. The solution was extracted with ethyl ether, washed with water and dried with anhydrous sodium sulphate. Solvent evaporation originates a solid material that was chromatographed (silica-gel, DCM/ethyl ether 10:1). The first fraction was collected and corresponded to 0.20 g (0.078 mmol) of **2c** (η=78 %, m.p.=134-135^{o}C).[4]

The estrone derivative **2** (1,3,5 (10)-estratrien-17-yliden)malononitrile) was prepared following a described procedure.[1,2] In a round flask 0.25 g of **2c** (0,098 mmol) 0.37 g (4.8 mmol) of ammonium acetate, 1.0 mL of acetic acid and 0.19 g (2.9 mmol) of malononitrile were added to 30 mL of toluene. The solution was refluxed overnight in a Dean-Stark apparatus, under nitrogen. The solution is treated with a saturated solution of $NaHCO_3$ (50 mL), washed with water, dried over Na_2SO_4 and the solvent evaporated under reduced pressure. The residue is chromatographed (silica-gel DCM and then EAC). The product is recrystallized in ethanol originating 0.19 g (η=65 %) of 2 (m.p.=200-202^{o}C).

Molecules were characterized using several techniques such as: infrared spectroscopy (IR), nuclear magnetic resonance (NMR), time-of-flight mass spectrome-

try (TOF MS), elemental analysis and X-ray crystallography. Characterization of molecule **1** and **2** is presented below.

References

1. H. Oevering, M. N. Paddon-Row, M. Heppener, A. M. O. Oliver, E. Cotsaris, J. W. Verhoeven and N. S. Hush, *J. Am. Chem. Soc.*, 1987, **109**, 3258–3269.

2. J. M. Lawson, D. C. Craig, A. M. Oliver and M. N. Paddon-Row, *Tetrahedron*, 1995, **51**, 3841.

3. A. W. T. Annen, K.; Hofmeister, H.; Laurent, H.; Seeger, *Chem. Ber*, 1978, **111**, 3094.

4. A. F. Brigas and R. A. Johnstone, *Tetrahedron Lett.*, 1990, **31**, 5789.

A.1 Characterization of molecule 1

1. **CHNS elemental analysis:** i) calculated for $C_{22}H_{24}N_2O$: C, 79.48; H, 7.28; N, 8.43, ii) found: C, 79.08; H, 7.15; N, 8.31.

2. **TOF MS (EI+) m/z:** i) calculated for $C_{22}H_{24}N_2O$ [M+] 332.44, ii) found 332.19.

3. **IR (KBr):** 3433, 2948, 2926, 2874, 2837, 2233, 1606, 1573, 1495, 1454, 1282, 1252, 1036, 887 cm^{-1};

4. ^{1}**H NMR** (400 MHz, $CDCl_3$): δ 1.07 (s, 3H), 1.46 –1.62 (m, 5H), 1.71-1.78 (m, 1H), 1.93 –2.05 (m, 2H), 2.26 – 2.31 (m, 1H), 2.48 (m, 1H), 2.46-2.50 (m, 1H), 2.68-2.71 (m, 1H), 2.75 – 3.02 (m, 4H), 3.78 (s, 3H), 6.65 (s, 1H), 6.74 (dd, 1H, J = 2.8 Hz, J = 8.8 Hz), 7.19 (d, 1H, J = 8.8 Hz). H-NMR spectrum of **1** is presented on Figure A.1.

5. ^{13}**C NMR** (100 MHz, $CDCl_3$): δ 16.6, 23.3, 26.3, 27.4, 29.5, 33.9, 34.7, 38.2, 43.2, 49.4, 54.1, 55.2, 79.7, 111.2, 111.7, 112.3, 113.9, 126.3, 131.3, 137.5, 157.8, 196.1. C-NMR spectrum of **1** is presented on Figure A.2.

6. **X-Ray crystallography** analysis is presented in Figure A.3. It shows that **1** is extended molecule with ring C of steroid with chair-like conformation. This is in good agreement with optimized structure calculated using electronic structure calculation, performed with GAMESS.

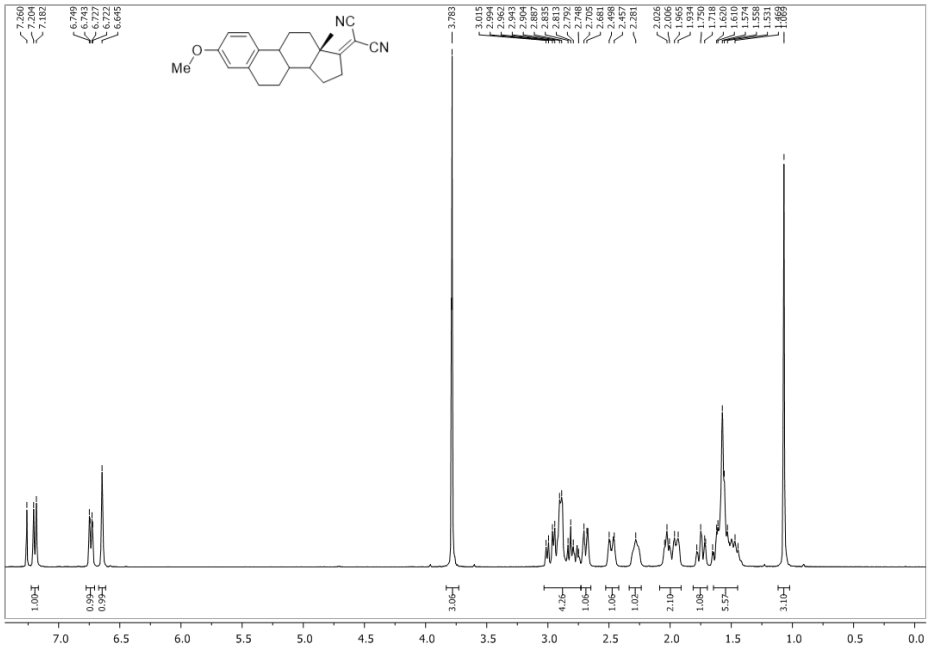

Figure A.1 ^{1}H NMR (400 MHz, $CDCl_3$) spectrum of compound **1**.

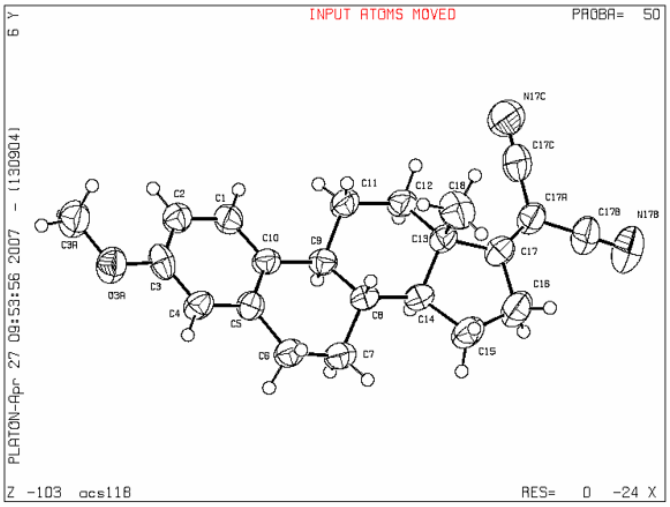

Figure A.3 X-Ray of **1.**

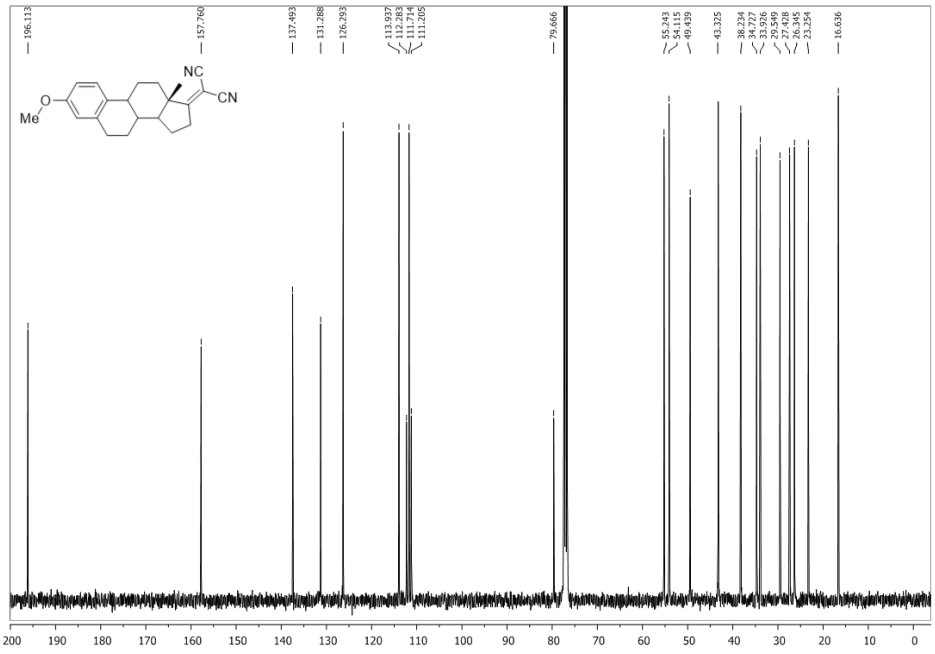

Figure A.2 ^{13}C NMR (100 MHz, $CDCl_3$) spectrum of compound **1**.

A.2 Characterization of molecule 2

1. **CHNS elemental analysis:** i) calculated for $C_{21}H_{22}N_2$: C, 83.40; H, 7.33; N, 9.26, ii) found: C, 83.02; H, 7.38; N, 8.79.

2. **TOF MS (EI+) m/z:** i) calculated for $C_{21}H_{22}N_2$ [M+] 302.18, ii) found 302.18.

3. **IR (KBr):** 3433, 2952, 2933, 2863, 1599, 1491, 1454, 1379, 746 cm^{-1}.

4. **^{1}H NMR** (400 MHz, $CDCl_3$): δ 1.08 (s, 3H), 1.43 – 1.54 (m, 2H), 1.59-1.70 (m, 3H), 1.76 (td, 1H, J = 4,0 Hz , J = 12.8 Hz), 1.94 – 2.07 (m, 2H), 2.33 – 2.38 (m, 1H), 2.49-2.55 (m, 1H), 2.69-2.73 (m, 1H), 2.75 – 2.84 (m, 1H), 2.91 – 3.02 (m, 3H), 7.07 – 7.11 (m, 1H), 7.13 – 7.19 (m, 2H), 7.28 – 7.30 (m, 1H). H-NMR spectrum of **2** is presented on Figure A.4.

5. **^{13}C NMR** (100 MHz, $CDCl_3$): δ 16.6, 23.3, 26.1, 27.4, 29.2, 34.0, 34.7, 38.0, 43.7, 49.4, 54.3, 79.7, 111.2, 112.3, 125.2, 125.9, 126.1, 129.1, 136.2, 138.9, 196.0. H-NMR spectrum of **2** is presented on Figure A.5.

6. **X-Ray crystallography** analysis was not performed, due to difficulty in

growth of good quality crystal.

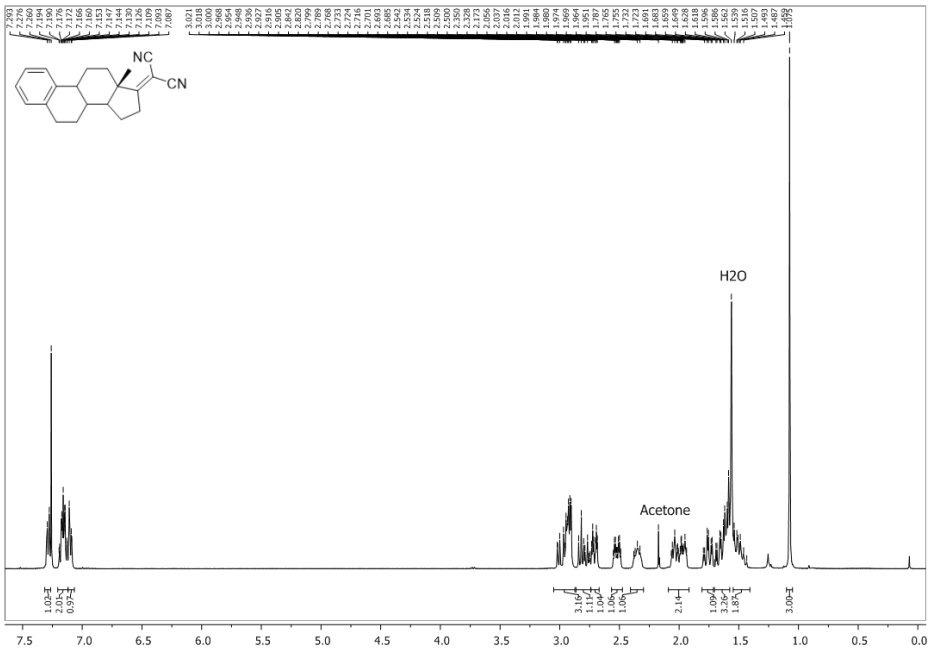

Figure A.4 ^{1}H NMR (400 MHz, $CDCl_3$) spectrum of compound **2**.

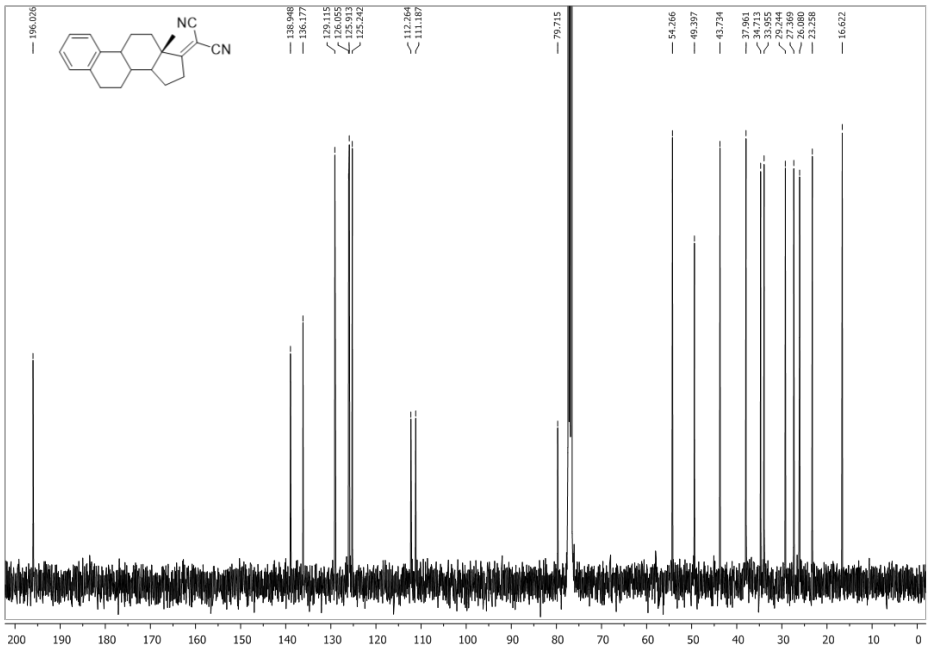

Figure A.5 ^{13}C NMR (100 MHz, $CDCl_3$) spectrum of compound **2**.

B Appendix

Fluorescence decays measured using TCSPC for naphthalene/fumaronitrile system, in various solvents and temperatures are presented in Figure B.1 and Figure B.2. These figures also contain information about weighted residuals, autocorrelated function (A.C.) and χ^2 values. Obtained data are presented in Table 3.1.

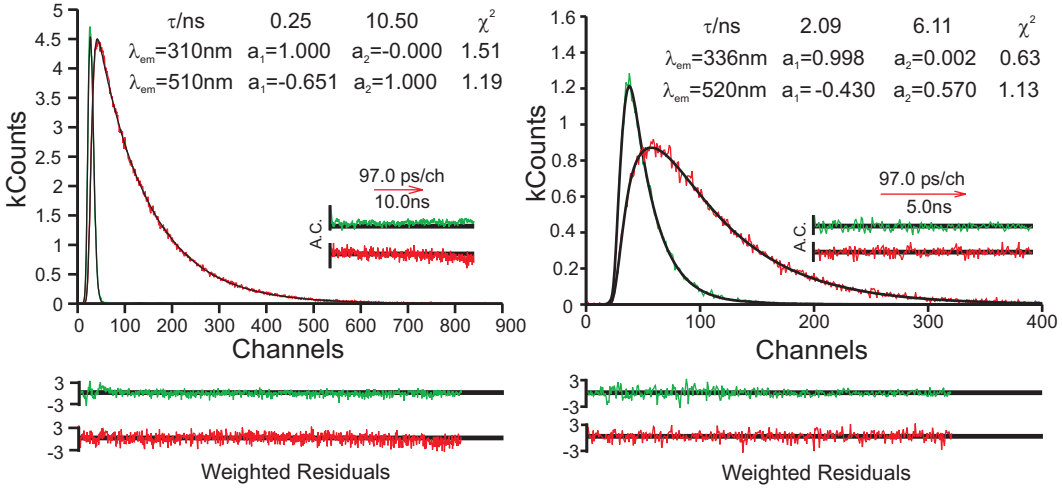

Figure B.1 Left: Fluorescence decay obtained with TCSPC and corresponding fit in dichloromethane (left), and 1,2-dichloroethane (right) for the charge-transfer complex of the naphthalene/ fumaronitrile system at $20°C$. Excitation at 282 nm and emission collected at 310 nm and 510 nm in DCM, and at 336 nm and 520 nm in DCE.

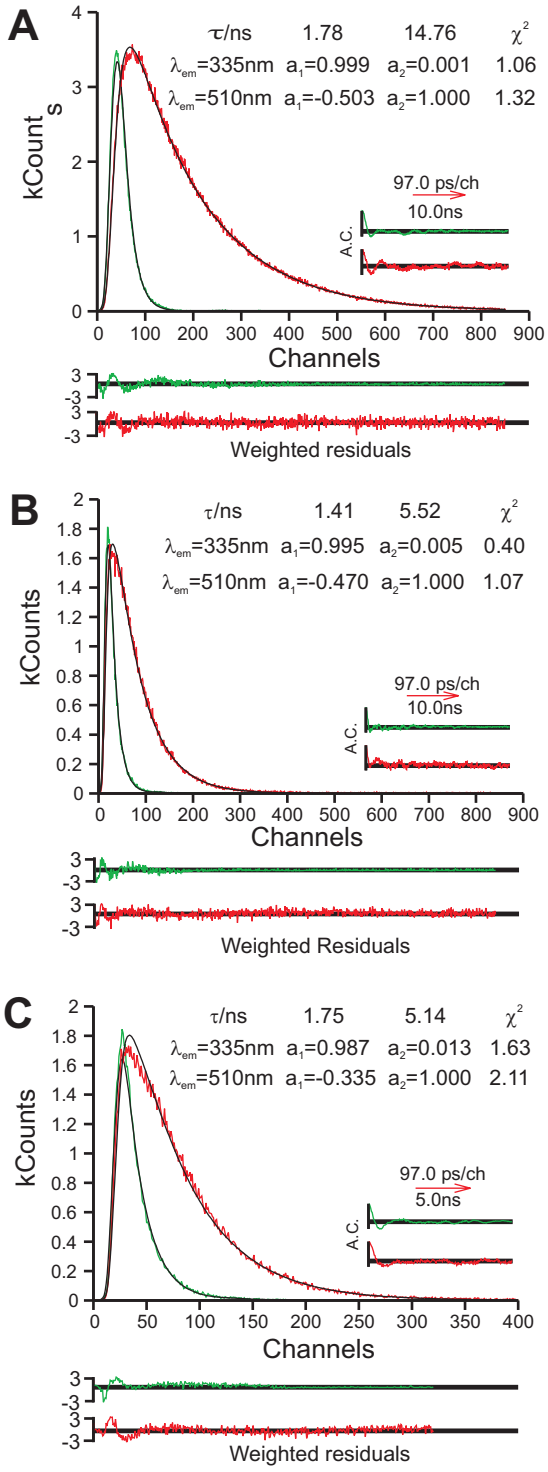

Figure B.2 Fluorescence decay obtained with TCSPC and corresponding fit in methyl acetate, for the charge-transfer complex of the naphthalene/ fumaronitrile system at 20°*C* (A), -15°*C* (B) and -30°*C* (C). Excitation at 282 nm and emission collected at 335 nm and 510 nm.

C Appendix

Table C.1 Parameters used to calculate dielectric constants employed in this study, from the dependence $\varepsilon = aT^2 + bT + c$, together with the temperature range for which equation can be used.

Solvent	ε (293K)	a	b	c	Temp. Range (K)
Di-n-butyl ether	3.1	5.462×10^{-5}	-4.058×10^{-2}	10.30	188-313.8
Isopropyl ether *	4.19	7.480×10^{-4}	-4.828×10^{-1}	81.44	298.2-323.2
Chloroform	4.81	5.680×10^{-5}	-5.183×10^{-2}	15.12	218.2-323.2
Ethyl acetate	6.08	5.369×10^{-5}	-5.099×10^{-2}	16.41	195.2-333.3
Dichloromethane	9.00	2.426×10^{-4}	-1.781×10^{-1}	40.36	184.1-306
Acetonitrile	37.03	3.908×10^{-4}	-4.028×10^{-1}	12.15	229.2-333.2

* Value extrapolated

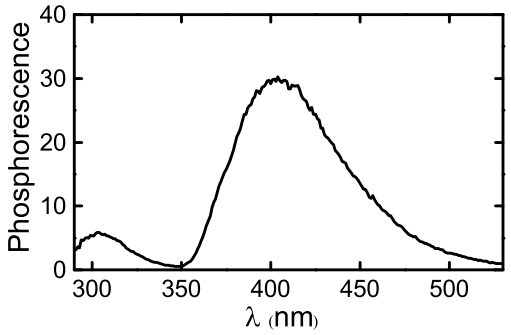

Figure C.1 Phosphorescence of dMA in mixture DCM:MeOH (1:1, v:v)

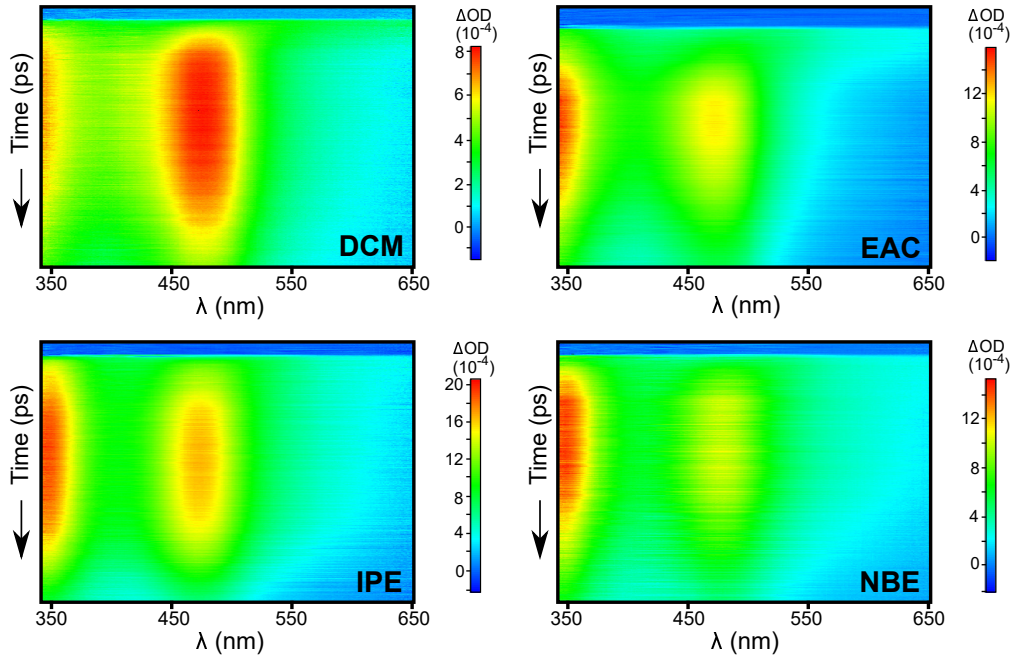

Figure C.2 2D images obtained by femtosecond transient absorption experiments in various solvents. 2D image in CHF is presented in Figure C.3

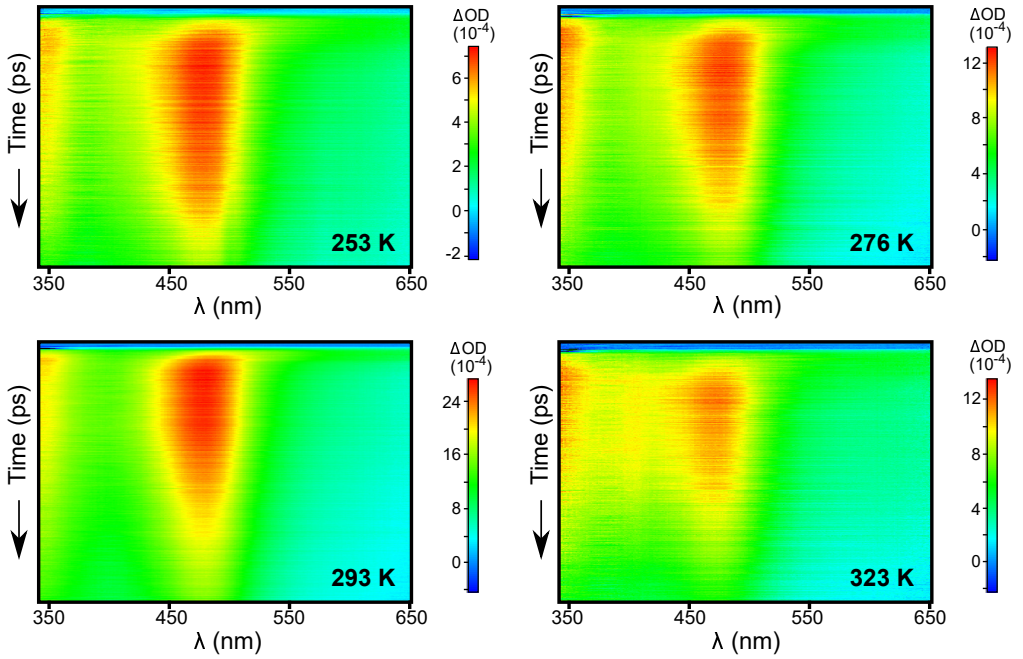

Figure C.3 2D images of data collected for **1** in chloroform at various temperatures, using fs pump-probe spectroscopy.

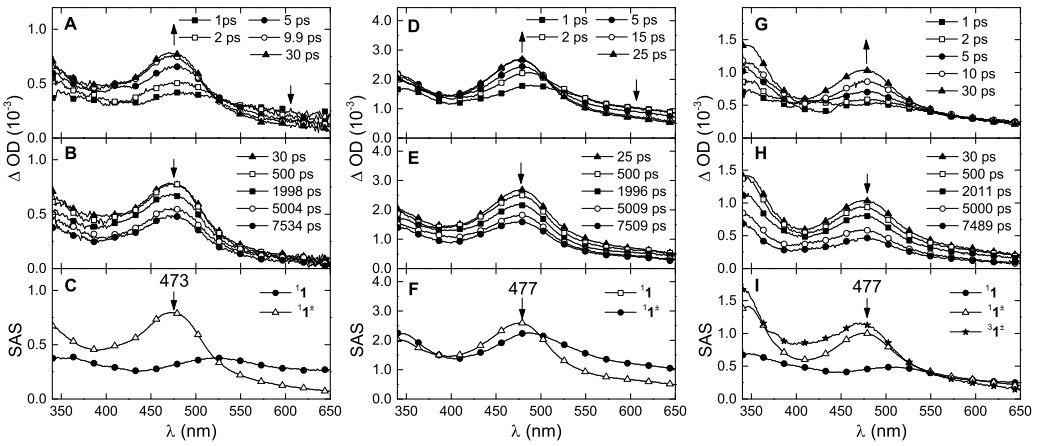

Figure C.4 Transient absorption spectra of **1** in dichloromethane (A,B), chloroform (D,E) and di-n-butyl ether (G, H) at various time delays and corresponding calculated Species-Associated Spectra in these solvents (C, F, I).

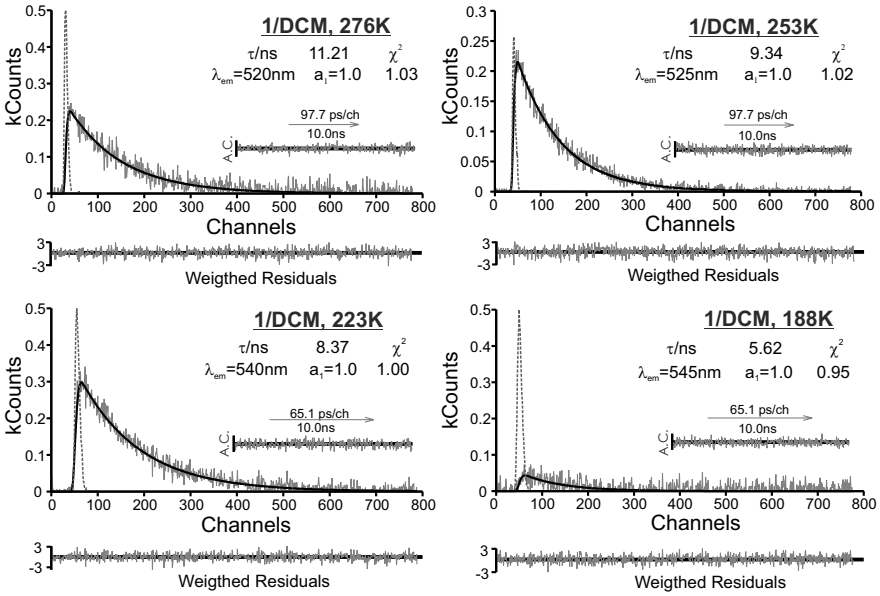

Figure C.5 Single Photon Counting of **1**, measured in dichloromethane at various temperatures, with applied monoexponential fitting after excitation at 282 nm. Weighted residuals, autocorrelated function (A.C.) and χ^2 values are also presented. The instrument response function is presented by the dashed line.

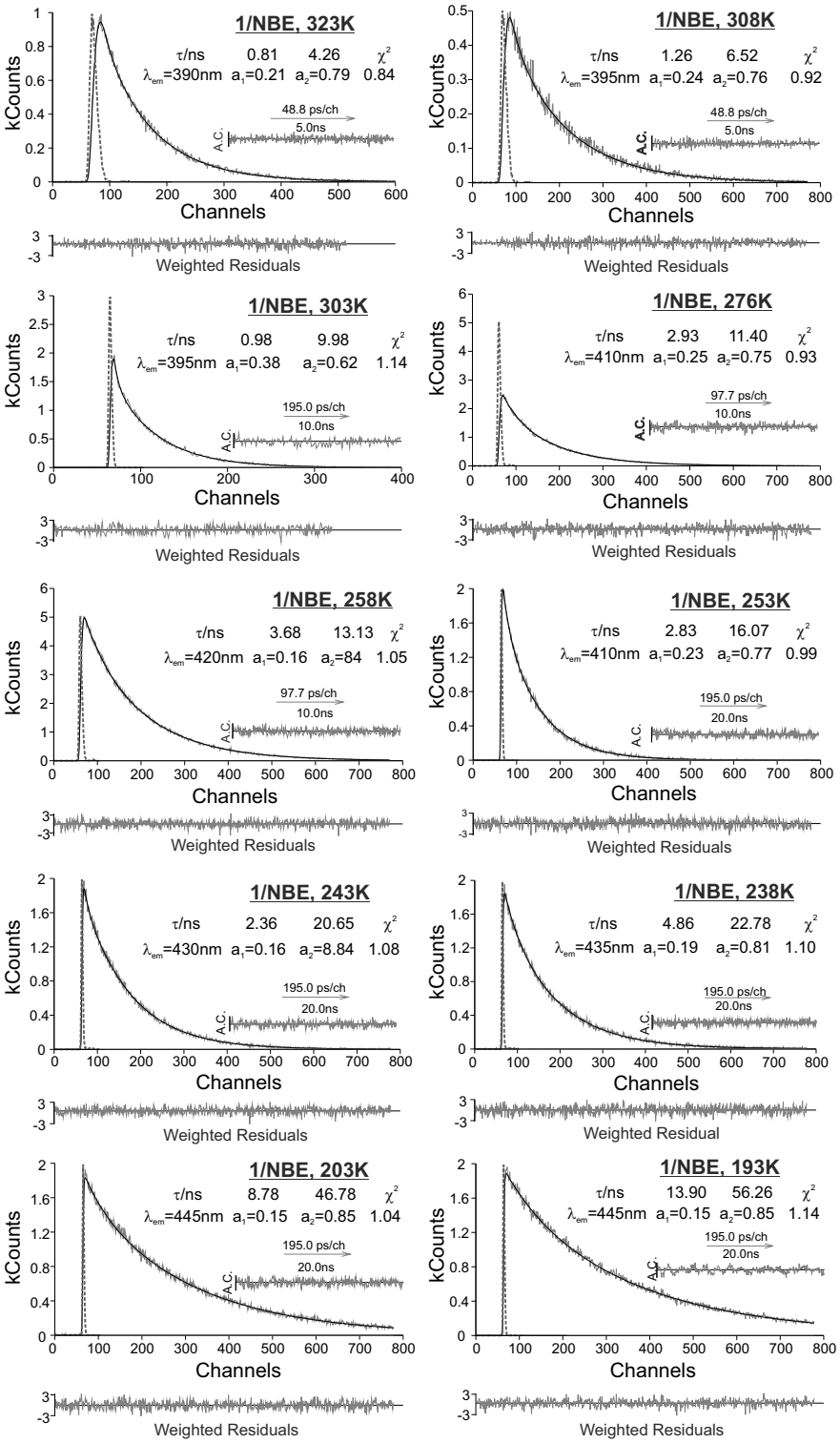

Figure C.6 Single Photon Counting of **1**, measured in di-n-butyl ether at various temperatures, with applied biexponential fitting after excitation at 282 nm. Weighted residuals, autocorrelated function (A.C.) and χ^2 values are also presented. The instrument response function is presented by the dashed line.

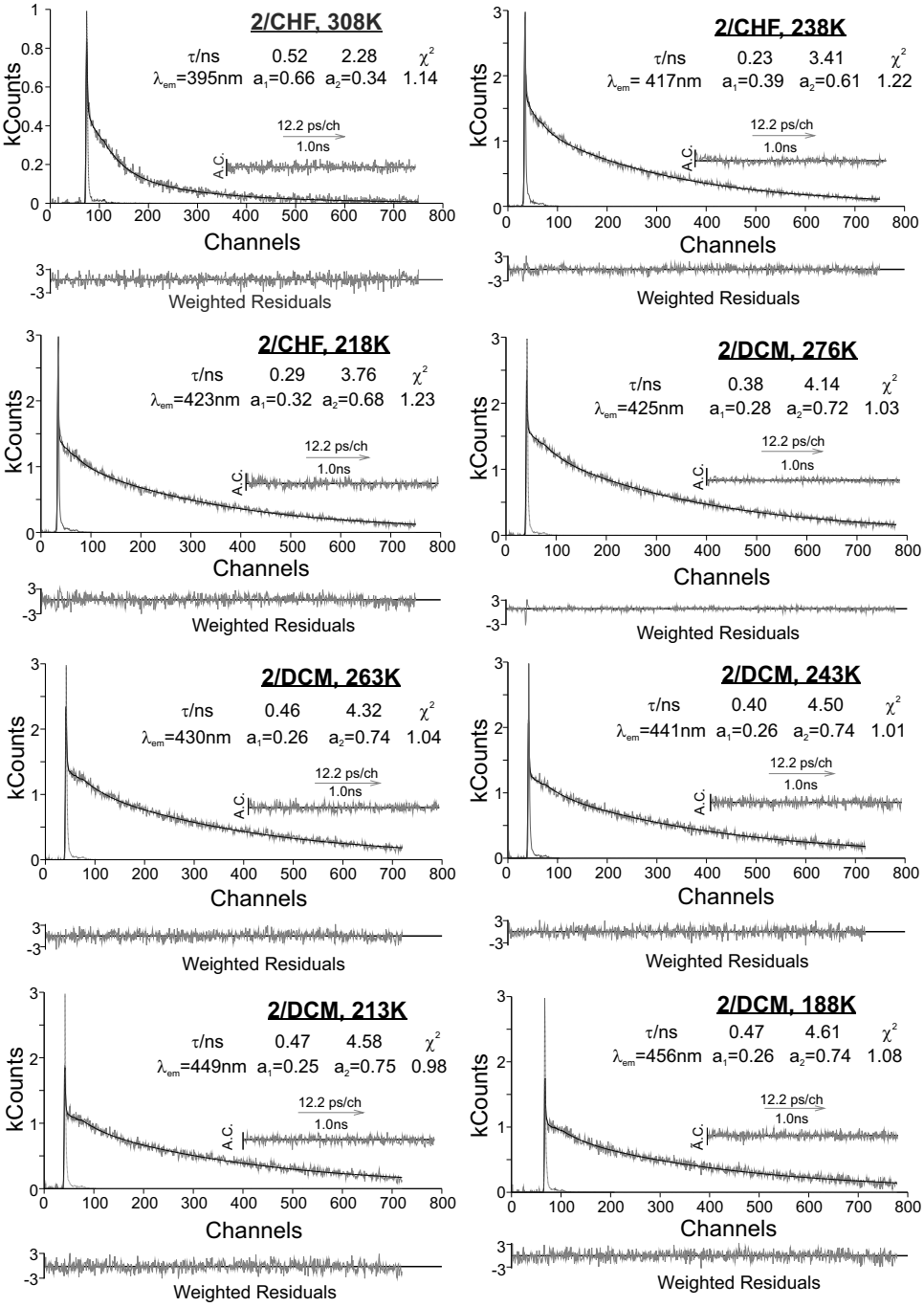

Figure C.7 Single Photon Counting of **2** in CHF and DCM at various temperatures, with applied biexponential fitting after excitation at 273 nm. Weighted residuals, autocorrelated function (A.C.) and χ^2 values are also presented. The instrument response function is presented by the dashed line.

List of Figures

List of Tables